TORSION PENDULUM STUDIES OF ^{4}He IN NANOPORES

By

SATORU MIYAMOTO

A DISSERTATION PRESENTED TO THE GRADUATE SCHOOL
OF THE UNIVERSITY OF FLORIDA IN PARTIAL FULFILLMENT
OF THE REQUIREMENTS FOR THE DEGREE OF
DOCTOR OF PHILOSOPHY

UNIVERSITY OF FLORIDA

1995

UNIVERSITY OF FLORIDA LIBRARIES

ACKNOWLEDGEMENTS

The author would like to thank his adviser, Yasumasa Takano for his patience and open-mindedness which have made the time he has spent working for him very enjoyable and interesting.

Thanks also go to Professors G. Ihas, J. Graybeal, C. Hooper, and M. Muga for serving on the author's supervisory committee. In addition, the author wishes to express his gratitude to Professors G. Ihas, S. Nagler and N. Sullivan for providing pieces of equipment which were crucial to this work and to Professor M. Meisel for the ruthenium oxide thermometers.

Thanks go to Bob Fowler and co-workers in the machine shop for providing a number of finely machined pieces for this work. Thanks also go to G. Labbe and B. Lothrop for technical support and supply of liquid helium. The author also wishes to express gratitude to the staff of the electronics shop for their support.

Special thanks go to the graduate students of the low temperature group for their help.

The author would like to thank Ray Strubinger and Miho Shraishi for assistance in preparing the dissertation.

TABLE OF CONTENTS

ACKNOWLEDGEMENTS ii

LIST OF FIGURES vi

LIST OF TABLES vii

ABSTRACT viii

1 INTRODUCTION 1

1.1 Superfluid ^{4}He 1
1.2 Kosterlitz-Thouless Theory for Two Dimensional Superfluidity 6
1.3 Superfluidity of Thin ^{4}He Films in Porous Vycor Glass 17
1.4 ^{4}He Adsorbed in Zeolite 17
1.5 ^{4}He Adsorbed in Porous Silica with a 25 Å Pore Diameter 21

2 EXPERIMENTAL TECHNIQUES AND CRYOSTAT 22

2.1 Torsion Pendulum 22
2.2 Thermometry 33
2.3 Four-Wire Resistance Bridge 35
2.4 Data Acquisition 41
2.5 Cryostat 45
2.6 Sample Gas-Handling System 53

3 CHABAZITE DEHYDRATION TECHNIQUE 58

3.1 Chabazite 59
3.2 Vacuum Dehydration of Chabazite and Nitrogen Adsorption Isotherm. . . . 62
3.3 High Pressure Dehydration of Chabazite 70

4 TORSION PENDULUM EXPERIMENT ON ^{4}HE ADSORBED IN CHABAZITE 82

4.1 Sample Cell 82
4.2 Results and Analysis 84
4.3 Conclusions 84

5 TORSIONAL PENDULUM EXPERIMENT ON ^{4}He ADSORBED IN 25 Å DIAMETER PORES OF SILICA 90

5.1 Sample Cells 90
5.2 Results and Discussions 92
5.3 Conclusions 114

A HELIUM VAPOR PRESSURE THERMOMETER 117

B TORSION PENDULUM EXPERIMENT USING CHABAZITE CRYSTAL C16 123

B.1 Results for the Torsion Pendulum Containing Chabazite 123
B.2 Results for the Torsion Pendulum with an Empty Cell (A Control Experiment) 133
B.3 Analysis and Conclusions 136
B.4 Conclusions 144

REFERENCES 146

LIST OF FIGURES

1.1 Andronikashvili's torsional pendulum. 2
1.2 Superfluid density 4
1.3 Dispersion curve of superfluid 5
1.4 Two-dimensional superfluid density 8
1.5 Vortex placed in a uniform external flow 10
1.6 Solutions of the Kosterlitz-Thouless recursion equation 16
1.7 Superfluidity density of ^{4}He films in porous Vycor glass 18

2.1 Torsion pendulum 23
2.2 Schematic diagram of the feedback circuit 25
2.3 Construction of the electrodes 27
2.4 Circuit diagram of the phase shifter 29
2.5 Circuit diagram of the zero crossing detector 30
2.6 Calibration of the ruthenium oxide thermometer Bk5p104 34
2.7 Calibration of the ruthenium oxide thermometer Bk6p93 36
2.8 Circuit diagram of the Anderson bridge 37
2.9 Equivalent circuit for the four-wire bridge 39
2.10 Phase shift caused by the ferrite core 42
2.11 Ratio of the error signal to the resistance difference 44
2.12 Dilution refrigerator 47
2.13 Thermal anchoring box for the coaxial cables 54
2.14 Gas-handling system 55

3.1 Cage structure of chabazite 60
3.2 Framework structure of chabazite 61
3.3 Adsorption isotherm of nitrogen at 77 K on chabazite 63
3.4 Heating curves of vacuum dehydration 65
3.5 Home-made furnace and the power controller 68
3.6 Ramp circuit 69
3.7 High pressure furnace using a MS-17 reactor 71
3.8 High pressure furnace made from a 1/2 inch stainless steel tube 75
3.9 Heating curves for chabazite dehydration runs C3 and C4 79

4.1 Torsion pendulum containing a chabazite crystal 83
4.2 Resonance curve of the torsional pendulum 85
4.3 Temperature dependence of the resonant frequency 86
4.4 Temperature dependence of the amplitude 87
4.5 ^{4}He-loading sensitivity 88

5.1 Adsorption isotherm 91
5.2 Torsional pendulum for the porous silica experiment 93
5.3 Frequency curves for porous silica 95
5.4 Amplitude for porous silica 96
5.5 1-χ for various amounts of adsorbed ^{4}He 97
5.6 Frequency shift for coverages from 6.75 mmol to 7.80 mmol 99
5.7 Frequency shift for 8.01 mmol to 8.20 mmol 100
5.8 Critical temperature 102
5.9 Fitting parameter for $\alpha T^2 + \beta T$ dependence of the frequency data at low temperatures 104
5.10 Phonon velocity 106
5.11 Superfluid density calculated by the theory of Kotsubo and Williams. . . . 110
5.12 Superfluid density for various film thicknesses 111
5.13 Fitting to the superfluid density at 7.60 mmol and 7.80 mmol 113
5.14 Core radius obtained by Cho and Kotsubo 115

A.1 Helium vapor pressure thermometer 119
A.2 Capacitance of the vapor pressure thermometer as a function of pressure at 77 K 120
A.3 Circuit diagram of the capacitance bridge for the vapor-pressure thermometer 122

B.1 Frequency of the torsion pendulum containing chabazite crystal C16. 124
B.2 Frequency as a function of temperature for various amounts of ^{4}He. 125
B.3 Amplitude of the torsional pendulum containing chabazite crystal 126
B.4 History dependence of the frequency anomaly 127
B.5 Size of the frequency anomaly for various amounts of ^{4}He 129
B.6 Frequency for the amounts of ^{4}He larger than 2.32 mmol. 130
B.7 Adsorption isotherm of ^{4}He at 4.2 K on the chabazite crystal 132
B.8 Frequency of the torsional pendulum with an empty cell 135
B.9 Frequency of the floppy mode of the torsional pendulum with an empty cell 137
B.10 Amount of liquid ^{4}He escaping from the cell 138
B.11 $\int_0^T \sigma dT$ as a function of temperature for superfluid ^{4}He 140
B.12 Onset temperature of the frequency anomaly 141
B.13 Size of the frequency anomaly for the floppy mode and the torsional mode . 143

LIST OF TABLES

2.1 Resonance frequency and Q factor 32
2.2 Specification of ferrite cores 41
2.3 Resistance value of thermometers 51
2.4 Volume of each part of the refrigerator system 52
2.5 Calibration coefficients for the Paroscientific pressure transducer 56

3.1 Summary of vacuum dehydration 66
3.2 Summary of run H 67
3.3 Summary of Supercritical Dehydration 72
3.4 Summary of high pressure dehydration in the 1/2 inch furnace 74
3.5 Summary of high-pressure dehydration in the 9/16 inch furnace 78

5.1 Results of nonlinear least square fitting 94
5.2 Coherence length obtained from superfluid density near T_c 101
5.3 Fitting parameters with the Kotsubo-Williams theory 112

Abstract of Dissertation Presented to the Graduate School
of the University of Florida in Partial Fulfillment of the
Requirements for the Degree of Doctor of Philosophy

TORSION PENDULUM STUDIES OF ^{4}He IN NANOPORES

By

Satoru Miyamoto

December 1995

Chairman: Professor Yasumasa Takano
Major Department: Physics

In this dissertation, experimental results are presented on the torsion pendulum studies of ^{4}He adsorbed in chabazite, whose pore is 13 Å in diameter, and in silica with 25 Å diameter pores. The objective of this work was to search for superfluidity in extremely confined ^{4}He.

A novel technique for dehydrating chabazite crystals has been developed for this work. As we found out, chabazite crystals of millimeter sizes cannot be dehydrated simply by heating them in vacuum as commonly done for zeolite powders, since the heating results in pulverization of the crystals. To dehydrate the crystals without damage, a high pressure dehydration technique has been developed. In this method, chabazite crystals are heated in a high pressure helium atomosphere at pressures over 10,000 psi in a furnace attached to a sorption pump filled with activated charcoal. The pump removes water selectively under

high pressure. Using a crystal prepared with this method, the experiment down to 100 mK found no superfluidity in ^{4}He adsorbed in chabazite crystal with the torsion pendulum technique.

In porous silica, superfluid transition was observed with the transition temperature ranging from 0.12 K to 0.82 K depending on the ^{4}He coverage. Near the full pore coverage, the temperature dependence of the superfluid density was found to arise entirely from the phonon excitation, with no evidence for other mechanisms such as vortex-pair unbinding. The superfluid density for lower ^{4}He coverages are compared with the Kosterlitz-Thouless theory adopted by Kotsubo and Williams for a small sphere. The fitting parameters obtained from the comparison are examined to address the applicability of the Kosterlitz-Thouless theory to ^{4}He films in extreme confinement.

CHAPTER 1
INTRODUCTION

1.1 Superfluid ^{4}He

^{4}He is believed to remain liquid even at $T = 0$ due to the small mass and the weakness of the attractive force between the atoms. Liquid ^{4}He becomes a superfluid when it is cooled to $T_\lambda = 2.17$ K. Although the superfluid has been known for decades, the microscopic mechanism responsible for the transition has not yet been fully understood.

Andronikashvili's experiment. In 1946, Andronikashvili [1] confirmed the validity of the two-fluid model [2, 3, 4] in his experiment, which measured the temperature dependence of the superfluid density of ^{4}He using a torsional pendulum. This device consisted of a stack of equally spaced aluminum disks, which were attached to a phosphor bronze wire and immersed in liquid ^{4}He as illustrated in Fig. 1.1. The gap between the disks were chosen to be smaller than the viscous penetration depth $\sqrt{2\eta_n/\omega\rho_n}$ of the normal component of superfluid ^{4}He, so that the normal component between the disks follows nearly completely the motion of the disks. Here η_n and ρ_n are the viscosity and the density of the normal component. The resonance frequency ω of the torsional oscillation of the pendulum is a function of the rigidity of the wire and the total moment of inertia of the pendulum, including the liquid which moves with the disks. Above T_λ, where ^{4}He is a normal liquid, the entire liquid between the disks moves with the pendulum. Below T_λ, the resonance frequency increases as the superfluid component, which has no viscosity, decouples from

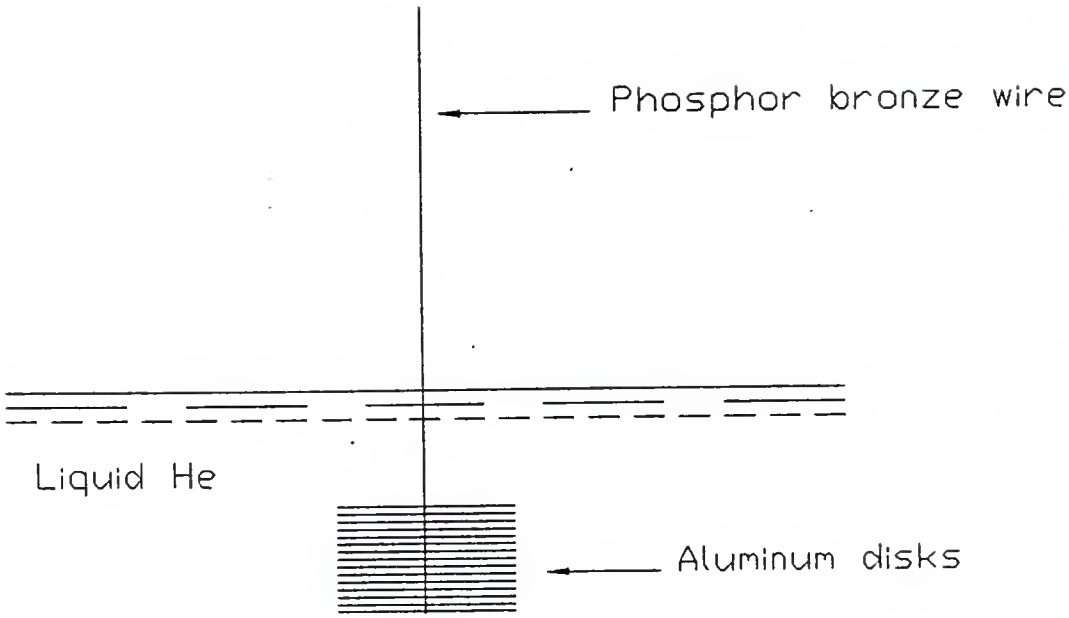

Figure 1.1. Andronikashvili's torsional pendulum [1].

the motion of the pendulum. The frequency change is proportional to the superfluid density ρ_s as will be discussed in Section 2.1. The temperature dependence of ρ_s measured by this method is shown in Fig. 1.2, in which ρ_s has been normalized by the total density ρ of liquid ^{4}He.

Landau's theory. In 1941, Landau [2, 3] predicted that the dispersion curve of elementary excitations in superfluid ^{4}He should be linear at low energies and deviate at higher energies from the linear relation, becoming a parabola with a local minimum at a finite energy Δ and momentum p_0. The excitations in the linear region are called phonons and those in the parabolic region are called rotons. Figure 1.3 shows the dispersion curve measured by Henshaw and Woods [6] in 1961 using neutron scattering. Their experiment, as well as those of others, agrees with Landau's prediction.

When the velocity of the superfluid relative to a wall exceeds the critical velocity, which is determined as the slope of the line drawn from the origin to the tangent of the parabola near its minimum, the flow can lose its kinetic energy through roton creation. The Landau critical velocity for roton creation is 58 m/sec. Below the critical velocity, the flow does not dissipate any energy. An ideal gas which consists of free particles has a dispersion $\epsilon = p^2/2m$. Since the critical velocity is zero in this case, macroscopic flow of the ideal gas loses kinetic energy at any velocity. Therefore, the ideal gas cannot be a superfluid. In Landau's picture, the dispersion curve with a non-zero slope at $\vec{p} = 0$ is crucial for the occurrence of superfluidity. Bose-Einstein condensation has no direct role in superfluidity, according to Landau.

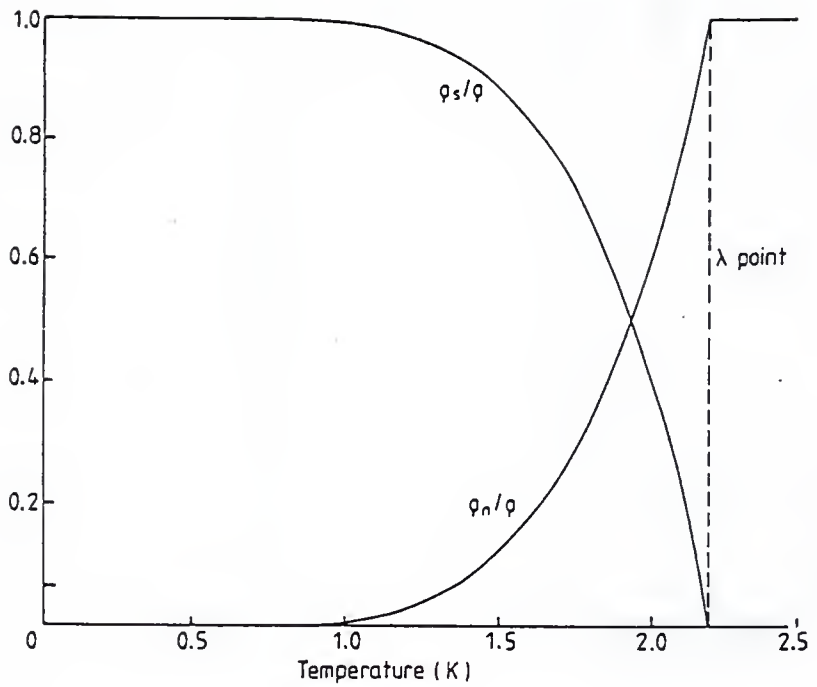

Figure 1.2. Superfluid density and the normal-fluid density of superfluid ^{4}He as a function of temperature, after Tilley and Tilley [5].

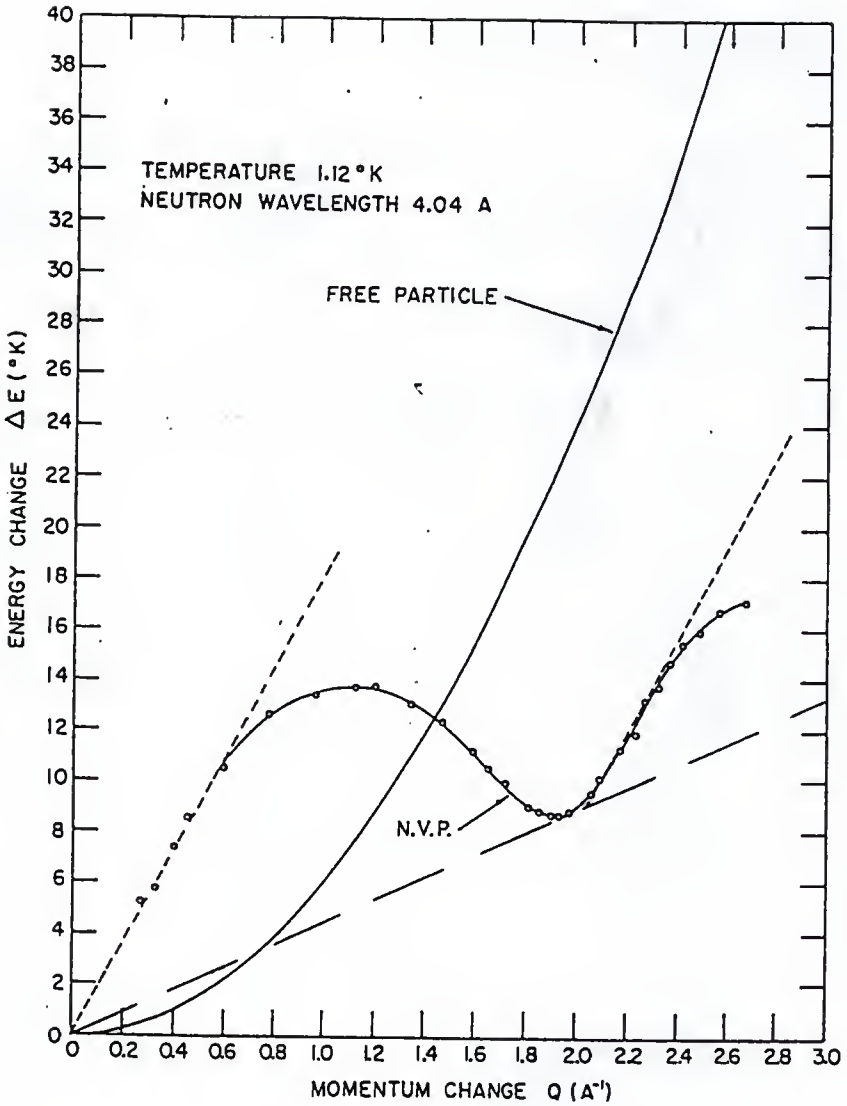

Figure 1.3. Dispersion curve of elementary excitations in superfluid ^{4}He, after Henshaw and Woods [6].

In Landau's theory, the normal fluid density below T_λ is

$$\rho_n = \frac{1}{V}\sum_p p_z^2 \frac{dn}{d\epsilon}\,, \tag{1.1}$$

where p is the momentum of each elementary excitation, either a phonon or a roton, and $n = n(\epsilon, T)$ is the number density at energy ϵ. The number density of phonons follows Bose-Einstein statistics. Boltzmann statistics is appropriate for the rotons because the Boltzmann factor $\exp(-\Delta/k_BT)$ is more than 50 at temperatures below T_λ for the roton energy $\Delta = 8.65$ K.

$$n_{\rm ph} = 9.60\pi\left(\frac{k_BT}{hc}\right)^3\,; \tag{1.2}$$

$$n_{\rm ro} = \frac{2p_0^2(\mu k_BT)^{1/2}\exp(-\Delta/k_BT)}{(2\pi)^{3/2}\hbar^3}\,, \tag{1.3}$$

where c is the phonon velocity. From Eqs. 1.2,1.3 and Eq. 1.1, one can obtain the temperature dependence of the normal fluid density $\rho_{\rm n}$. At low temperatures $\rho_{\rm n}$ increases as $\sim T^4$ due to the phonon excitation. At higher temperatures, the roton excitation contributes to the $\rho_{\rm n}$ as $\sim T^{-1/2}\exp(-\Delta/k_BT)$. These expressions indicate that the phonon excitation dominates at temperatures lower than 0.6 K. Above 1 K, the roton excitation becomes dominant. In the critical region near T_λ, where the fluctuations are essential, the picture of elementary excitations is no longer valid.

1.2 Kosterlitz-Thouless Theory for Two Dimensional Superfluidity

Bishop [7] and Agnolet [8] have studied the superfluid transition of thin ^{4}He films adsorbed on Mylar sheets by using torsional pendulum techniques. Figure 1.4 shows the temperature dependence of the superfluid density of ^{4}He films ranging in thickness from

a submonolayer to a few atomic layers [8]. Here the period shift ΔP of the pendulum is proportional to the superfluid density, ρ_s.

The superfluid transition observed by these authors has been successfully explained by the theory developed by Kosterlitz and Thouless [10]. There are many good reviews of the Kosterlitz-Thouless theory, including one by Agnolet and Reppy [9, 11, 12].

Vortex in an external superflow. The order parameter of superfluid ^{4}He is written as

$$\psi(\vec{r}) = \sqrt{\frac{\rho_s(\vec{r})}{m}} \exp(i\phi(\vec{r})) \,, \tag{1.4}$$

where ρ_s is the superfluid density, ϕ is a real function of position $\vec{r}$, and m is the atomic mass of ^{4}He. Since the current density is $\vec{j_s}(\vec{r}) = \hbar/m(\phi^*\nabla\phi - \phi\nabla\phi^*)$ and $\vec{j_s}(\vec{r}) = \rho_s\vec{v_s}$, the superfluid flow field is $\vec{v_s}(\vec{r}) = (\hbar/m)\nabla\phi$, which states that the superfluid flow is the gradient of the phase of the order parameter.

When there is a vortex in superfluid ^{4}He without an external flow, the flow field around the vortex is quantized according to

$$\vec{v_s} = n\frac{\hbar}{mr^2}\vec{z} \times \vec{r} \tag{1.5}$$

$$= n\frac{\hbar}{mr}\vec{\theta}, \tag{1.6}$$

where n is an integer, and $\vec{\theta}$ is a unit vector for the θ direction of the polar coordinates in which $\hat{z}$ is the direction along the core of the vortex. The energy of the vortex is a sum of the kinetic energy of the superflow around the vortex core and the core energy E_c. It can

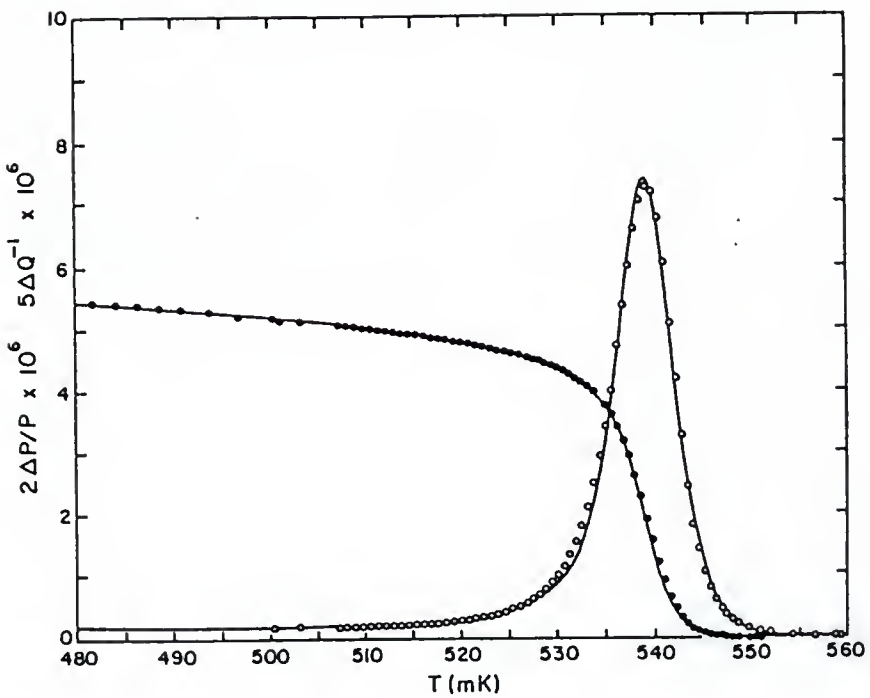

Figure 1.4. Period shift and Q^{-1} as functions of temperature for a ^{4}He film on a Mylar sheet after Agnolet [9]. The coverage is 34.03 μmol/m^2.

be written as

$$
\begin{aligned}
E_{\text{vortex}} &= \frac{1}{2}\int \rho_s v_s^2 d\vec{r} + E_c \\
&= n^2 \pi K_0 \log(R/a) + E_c \,, \qquad (1.7)
\end{aligned}
$$

where the energies are per length of the vortex, $K_0 = \rho_s(\hbar/m)^2$, a is the vortex core radius, and R is the size of area on which the film is present.

When a singly-quantized vortex ($n = 1$) is placed in a uniform superflow as shown in Fig. 1.5, the flow below the core is faster than the flow above it. Since the phase $\phi(\vec{r})$ of the order parameter changes by 2π on going around the core of the vortex, the phase increases by 2π along a path taken below the core and decreases by 2π for a path taken above the core. When a vortex moves downward, the velocity of the uniform superflow decreases by $\hbar/Lm$, where L is the width of the external flow. This means that a free vortex receives a force downward from the uniform flow and, as it moves, dissipates the kinetic energy of the flow. The force on the vortex is essentially the same as the Magnus force on a rotating cylinder placed in an air flow.

In bulk and thick films of ^{4}He, where vortices have macroscopic lengths, the energy given by Eq. 1.7 is much larger than the thermal energy $k_B T$. In atomically thin films of ^{4}He, however, vortices are the essential elementary excitations that determine the normal-fluid density ρ_n near the transition temperature.

<u>Vortex-vortex interaction.</u> In order to understand how the thermally excited vortices in two-dimensional ^{4}He determine the superfluid density near the transition temperature T_c, one needs to start with the interaction between two vortices. From here on, ρ_s will be

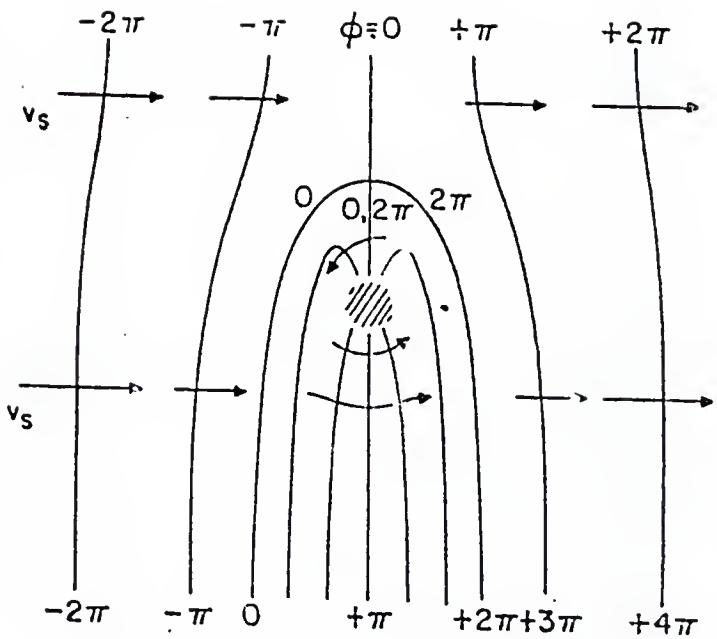

Figure 1.5. Flow around a vortex in a uniform external flow with superimposed phase contours after Langer and Reppy [12].

the areal superfluid density instead of a three-demensional one. When there are two singly-quantized vortices with superflow in the opposite direction from each other in the absence of an external flow, the flow fields add constructively in the region between the cores and cancel each other in regions far from the cores. As a consequence, the total kinetic energy can be reduced by bringing the two vortices closer. This means that there is an attractive force between the two vortices of opposite signs. The energy of a vortex pair is [13]

$$E_{\text{pair}}(r) = 2\pi\rho_s \left(\frac{\hbar}{m}\right)^2 \log(r/a) + 2E_c \,, \tag{1.8}$$

where r is the separation of the cores.

When the vortex pair is placed in a uniform external superflow, the pair feels a force tending to increase the separation. This force is a function of the separation r of the pair. A sufficiently large external flow can break apart a vortex pair. The energy of the vortex pair is written as

$$E(r) = E_{\text{pair}} - p_{\text{pair}} v_s \,, \tag{1.9}$$

where v_s is the external flow velocity and p_{pair} is the moment of the pair [12, 13], which is

$$p_{\text{pair}} = \rho_s \sqrt{\frac{h}{m}} \,. \tag{1.10}$$

The energy $E(r)$ has a maximum at

$$r_c = \frac{1}{2\pi v_s} \sqrt{\frac{h}{m}} \,. \tag{1.11}$$

Vortex pairs with separations less than r_c remain bound, whereas pairs with separations larger than r_c are pulled apart by the external flow.

Screening effect of vortex pairs. At low temperatures, there are few vortices thermally excited in the ^{4}He film. The vortices form pairs because of the attractive forces between two vortices with opposite superflow fluids around them. Therefore, the macroscopic superflow does not decay as long as the flow velocity is not large enough to break vortex pairs. At high temperatures where the number of vortices is large, the interaction between two vortices forming a pair becomes influenced by the superflow field of other pairs. A vortex pair placed between two vortices which are forming a larger pair increases the separation in response to the flow field of the larger pair. This costs energy for the larger pair, resulting in the reduction of the attractive force between the two vortices. This screening effect increases as the density of the vortex pairs increases with temperature.

The situation described above is analogous to a dielectric in an electric field. In fact, the problem of many vortex pairs in a uniform superflow can be exactly mapped to that of positive and negative charges in an electric field. In this description, the screening effect can be approximated by introducing a dielectric constant $\epsilon(r)$, which represents the effect of many nested pairs of vortices located between the two vortices forming a pair we are considering. The dielectric constant $\epsilon(r)$ can be written using the polarization $\alpha(r)$ of a vortex pair with separation r as

$$\begin{aligned} \epsilon(r) &= 1 + 4\pi\chi(r) \\ &= 1 + 4\pi \int_{r_0}^{r} d\vec{r'}\alpha(r')n(r') \,, \end{aligned} \tag{1.12}$$

where $n(r')$ is the two-dementional density of vortex pairs with separation r' and r_0 is . The polarization is given by

$$\alpha(r) = \frac{n\hbar}{m} \left. \frac{\partial < r\cos\theta >}{\partial v_s} \right|_{v_s=0} . \tag{1.13}$$

The average is taken over the annulus $r < r' < r + dr$. The result is

$$\alpha(r) = \frac{\pi r^2 K_0}{2k_B T} , \tag{1.14}$$

where $K_0 = \rho_s(\hbar/m)^2$. The density of vortex pairs can also be obtained by summing the Boltzmann factor $\exp(-E_{\text{eff}}/k_B T)$ over the annuls $r < r' < r + dr$ divided by r_0^4;

$$n(r) = \frac{2\pi r}{r_0^4} \exp\left(-\frac{E_{\text{eff}}}{k_B T}\right) , \tag{1.15}$$

where E_{eff} is the energy of a vortex pair in a dielectric medium

$$E_{\text{eff}}(r) = 2\pi K_0 \int_{r_0}^{r} \frac{dr'}{\epsilon(r')r'} . \tag{1.16}$$

As can be seen in these equations, these quantities have to be determined in a self-consistent fashion.

In order to make the calculation simple, it is useful to define a new length scale $l \equiv \log(r/r_0)$ and dimensionless functions

$$y(l) \equiv y_0(\frac{r}{r_0})^2 \exp\left(-\frac{E_{\text{eff}}}{2k_B T}\right) \tag{1.17}$$

and

$$K^{-1}(l) \equiv \epsilon(r) k_B T K_0^{-1} \,. \tag{1.18}$$

Here $y_0 \equiv \exp(-E_c/k_B T)$. Using these definitions, one can rewrite Eq. 1.12 as

$$K^{-1}(l) = k_B T K_0^{-1} + 4\pi^3 \int_0^l dl' y^2(l') \,. \tag{1.19}$$

Inserting Eq. 1.16 into Eq. 1.17 , one obtains

$$y(l) = y_0 \exp\left(2l - \pi \int_0^l K(l') dl'\right) \,. \tag{1.20}$$

Differentiating Eqs. 1.19 and 1.20 with respect to l leads to

$$\frac{dK^{-1}}{dl} = 4\pi^3 y^2(l) \tag{1.21}$$

$$\frac{dy(l)}{dl} = y(l)(2 - \pi K(l)). \tag{1.22}$$

According to Eqs. 1.19 and 1.20, the initial conditions for Eqs. 1.22 are $K^{-1}(0) = k_B T K_0^{-1}$ and $y(0) = y_0$. Combining Eqs. 1.22 one obtains

$$\frac{dK^{-1}}{dy} = \frac{4\pi^3 y}{2 - \pi K(l)}. \tag{1.23}$$

Integrating this equation leads to

$$2\pi^2 y^2 - \frac{2K^{-1}}{\pi} + \log\left(\frac{K^{-1}}{\pi}\right) = C(T) \,, \tag{1.24}$$

where the constant of integration $C(T)$ is determined by the initial conditions at $l = 0$ to be

$$C(T) = 2\pi^2 y_0^2 - \frac{2}{\pi} k_B T K_0^{-1} + \log\left(\frac{k_B T K_0^{-1}}{\pi}\right) . \tag{1.25}$$

Eliminating $y^2(l)$ from Eqs. 1.24 into yields

$$\frac{dK^{-1}}{dl} = 4K^{-1} - 2\pi \log \frac{K^{-1}}{\pi} + 2\pi C(T) . \tag{1.26}$$

A group of solutions for this differential equation are plotted in Fig. 1.6. The figure can be divided into three regions according to the temperature. In region C above T_c, each line representing a solution at a given temperature initially falls as l increases but starts to rise for larger l, without hitting the horizontal axis. Since l represents the separation of the vortex pair and a larger $y(l)$ means a higher density of vortex pairs, the solutions above T_c can be interpreted as unbound states of vortex pairs. As K^{-1} diverges, the dielectric constant ϵ diverges, also indicating free vortex states. On the other hand, in region A for $T < T_c$, the lines intercept the horizontal axis on which $y = 0$. All pairs are considered to be in bound states. It is important to note that solution B for $T = T_c$ also intercepts the horizontal axis at finite l. This means that there is a finite ρ_s at $T = T_c$ unlike in bulk superfluid ^{4}He or in films of superfluid ^{4}He that are not atomically thin. Since y diverges to infinity above T_c, ρ_s becomes zero. This indicates that there is a discontinuity in ρ_s at T_c. Nelson and Kosterlitz [14] have shown that ρ_s/T in the limit of $T \to T_c$ from below is a universal constant which does not depend on the thickness of the film:

$$\lim_{T \to T_c} \rho_s/T = \rho_s(T_c)/T_c = \frac{2m^2 k_B}{\pi \hbar^2} . \tag{1.27}$$

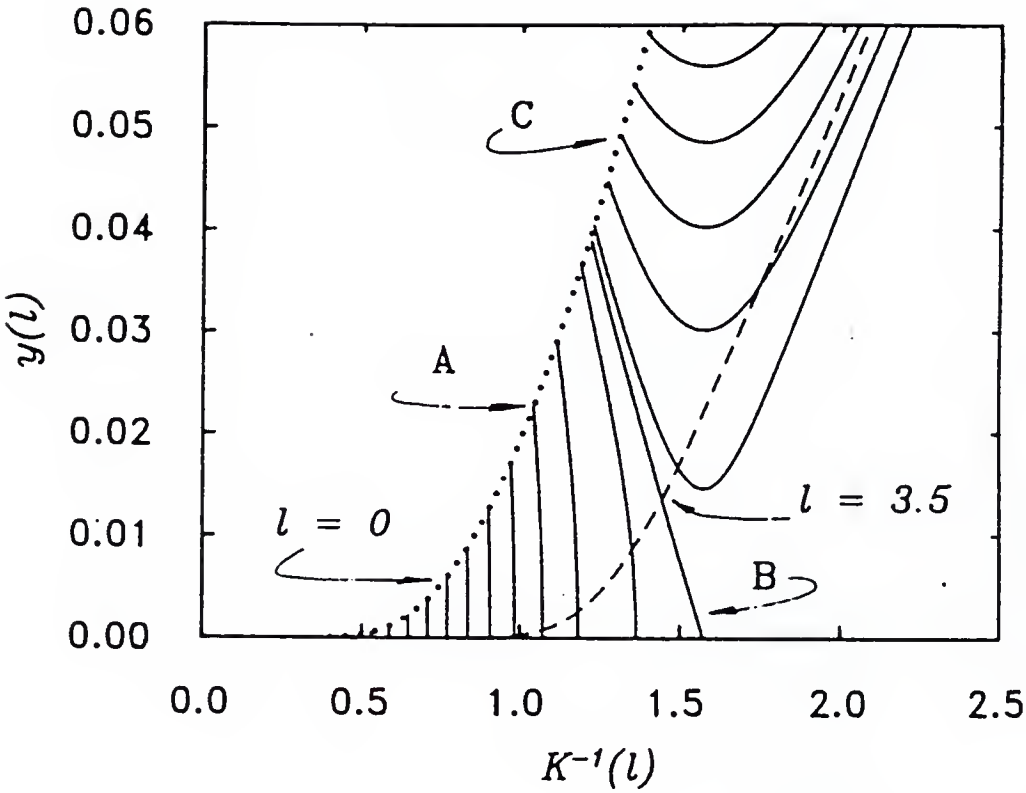

Figure 1.6. Solutions of the Kosterlitz-Thouless recursion equation after Agnolet [9]. The trajectories are classified into three groups according to the temperature. Line A represents solutions whose temperature is below T_c. These solutions intercept the horizontal axis with finite l. Line B is the solution for $T = T_c$ and crosses the horizontal axis with finite l. Lines C represent solutions for temperatures above T_c. These solutions never cross the horizontal axis. The dotted line shows values of y and K^{-1} at $l = 0$. The dashed line shows values of y and K^{-1} for $l = 3.5$.

1.3 Superfluidity of Thin ^{4}He Films in Porous Vycor Glass

There have been a series of studies on the superfluidity of thin ^{4}He films adsorbed in porous Vycor glass [7, 12, 15, 16], whose pores are 70 ± 10 Å in diameter and randomly connected to each other. Figure 1.7 shows the superfluid density ρ_s measured by the torsion pendulum technique []. The period shift δP of the pendulum is proportional to ρ_s.

The temperature dependence of the superfluid density obeys a power law $\Delta P(T) = \Delta_0(1 - T/T_c)^\zeta$ with a critical exponent $\zeta = 0.635 \pm 0.050$, which is close to the bulk liquid ^{4}He value. As the density of the film gets smaller, T_c decreases down to 3 mK. Reppy and co-workers have argued that the result suggests a cross-over from a regime of three dimensional superfluidity to a dilute ideal Bose gas-like behavior [15].

There is a different, but not necessarily orthogonal, interpretation of the results. Kotsubo and Williams [17] and other authors [18, 19] have argued that superfluidity of a thin ^{4}He film in the porous Vycor glass can be explained by vortex-pair unbinding. In this picture, the three-dimensionally interconnected pores modify the inter-vortex interaction from the logarithmic potential for the two-dimensional film case [18] to a linear potential at a distance larger than the pore diameter. For a distance shorter than the pore diameter, the interaction remains logarithmic. Due to the three-dimensional connectivity of the pores, however, the transition belongs to a three-dimensional universality class, which explains the critical exponent close to the value for the bulk superfluid transition in ^{4}He .

1.4 ^{4}He Adsorbed in Zeolite

Zeolite is a group of aluminosilicate minerals containing water. There are over 130 species of zeolite known to date, either natural or synthetic. The most unique feature of zeolite is that the mineral contains microscopic pores incorporated into the crystal structure.

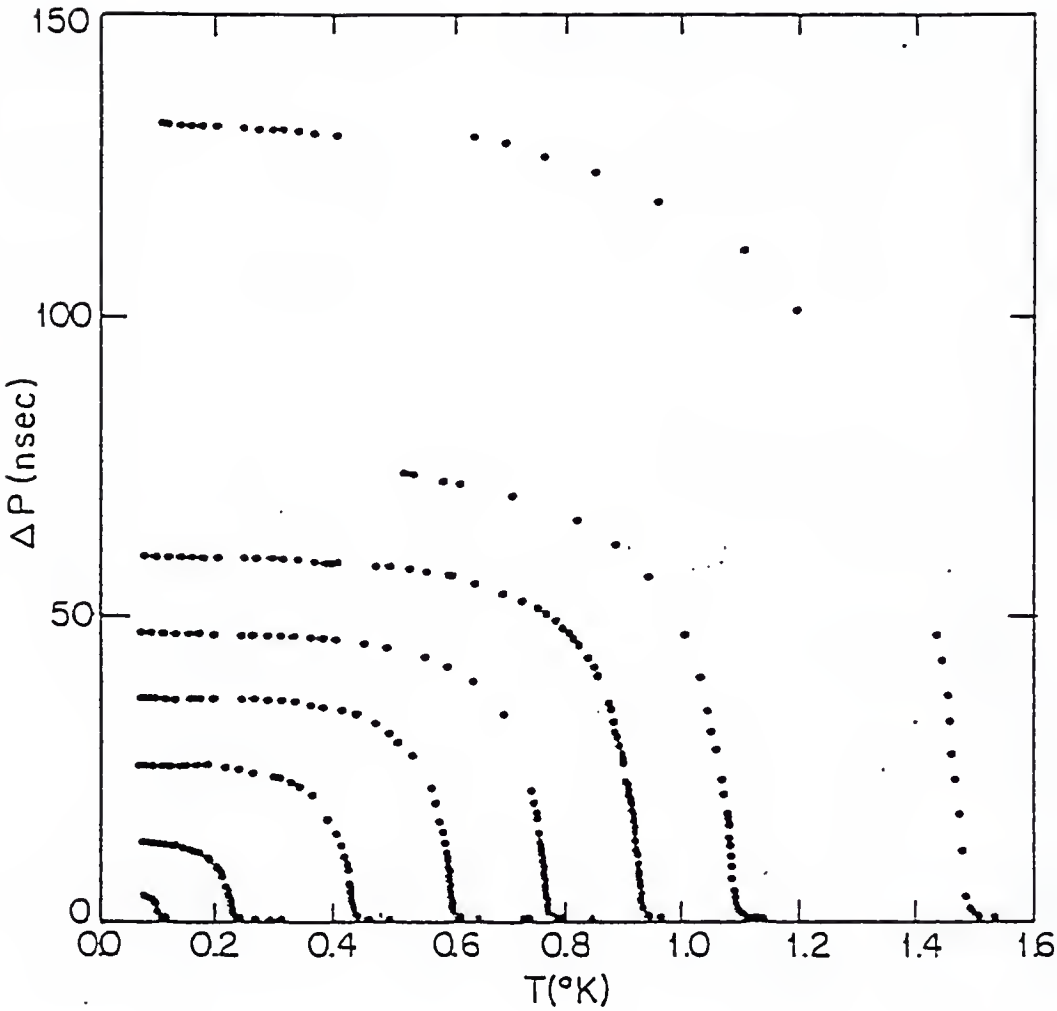

Figure 1.7. Superfluid density of ^{4}He films in porous Vycor glass after Bishop [7].

The diameter of these pores is typically less than 15 Å, which is only five times larger than the size of the ^{4}He atom and is too small to accommodate vortices whose core diameters are 25 ± 12 Å.

Recently, Shirahama *et al.* [20] have studied the superfluidity of thin ^{4}He films in porous glass with pore sizes ranging from 50 Å to 1 μm in diameter. From the relationship between T_c and the pore diameter, they found that the vortex core size to be $a_0 = 25 \pm 12$ Å, which is an order of magnitude larger than the vortex core of 2.6 Å for bulk liquid ^{4}He. If any superfluid transition were to be seen in a ^{4}He film in zeolite, one can expect the transition to be of a novel type not associated with the unbinding of vortex pairs.

Another important characteristic of zeolite is that the surface potential of the pores are periodic, since they are part of the crystal structure. This is in strong contrast to porous glass which is a heterogeneous substrate with a random surface potential. In the experiments of thin ^{4}He films in porous glass, a localized layer corresponding to ~ 1.7 atomic layer over the surface has always been observed. Only the ^{4}He atoms above this localized layer have been observed to become superfluid. Some workers have argued that because of strong but short-range attractive force from the substrate, the layer that sits directly on the substrate is compressed into a solid [7, 16]. However, this does not necessarily mean that a subatomic layer should be localized, since the ^{4}He atoms in this situation should be able to move along the surface unless the surface potential contains deep wells. Another argument is that ^{4}He atoms are localized due to the random surface potential in analogy to the localization of electrons in a random potential [21, 22]. If this is the case, a submonolayer of ^{4}He may exhibit superfluidity in zeolite, whose pores present a periodic surface potential.

Some zeolite species have three-dimensionally connected pores, which provide ^{4}He atoms with a circular path of a diameter less than 15 Å. In such a geometry, a vortex may exist whose core is a part of the substrate rather than normal fluid to save the core energy. It is interesting to speculate how a lattice of such vortices, which assume the periodicity of the zeolite framework, may lead to novel effects on the superfluidity.

These are our motivations in studying ^{4}He in zeolite. Chapter 3 of this dissertation gives a detailed description of chabazite, a particular type of zeolite we have chosen as our substrate. Following the discussion of dehydration technique for chabazite, Chapter 4 and Appendix B discuss the experimental results.

Previous study on helium in zeolite. Wada and Kato [23] have studied heat capacities and isosteric heat of sorption of ^{4}He and ^{3}He in Y zeolite (LTA). They have reported that the atoms are localized near the cations in the pores, when the amount of helium is small. As the amount of helium increases, ^{4}He atoms form a solid-like layer in the pores. Eventually ^{4}He starts to behave like either a gas or a liquid depending on the density of ^{4}He atoms over the first atomic layer. When ^{4}He nearly fills up the pores, the heat capacity becomes small again and this has been interpreted as an indication of a solid-like state. Wada and Kato have observed a hump in the heat capacity of adsorbed ^{3}He at a temperature below 1 K and they have interpreted it to be due to the Fermi degeneracy of ^{3}He atoms. Despite these pieces of evidence for ^{4}He being a fluid for some film coverages, there has been no sign of superfluidity in their results. However, looking for an anomaly in the heat capacity is a notoriously difficult way to discover superfluidity in thin films of ^{4}He in porous geometries. Prior to this dissertation, no search for superfluid transition in ^{4}He absorbed in zeolite has

been made with a torsional-pendulum technique, except for one negative study [] which used powders of Y zeolite.

1.5 ^{4}He Adsorbed in Porous Silica with a 25 Å Pore Diameter

Porous glass has been a very popular substrate in which to study the superfluidity of ^{4}He films in confinement. As has been discussed in section 1.3, vortex-pair dissociation may be responsible for the superfluid onset as in the case of the flat ^{4}He film. Studies by Shirahama *et al.* [20], mentioned in that section, have been our motivation to investigate superfluidity in ^{4}He films confined in pores whose size is close to the vortex core diameter. Naively, if vortices are responsible for a superfluid transition and their pore diameter is as large as claimed, then the transition temperature can be much enhanced in such pores, since the two vortices forming a pair can hardly accommodate any other vortices between them to screen the intra-pair interaction.

We have chosen porous silica with a nominal pore diameter of 25 Å as a substrate. Unlike zeolite pores, the pores have a random surface potential and are randomly connected with each other. These features are similar to those of porous Vycor glass.

CHAPTER 2
EXPERIMENTAL TECHNIQUES AND CRYOSTAT

2.1 Torsion Pendulum

Use of a torsion pendulum in studies of superfluids dates back to Andronikashvili [1], as discussed in Section 1.1. A modern version of this device has been developed by Reppy and co-workers [16, 24], who made it a powerful tool to study superfluid ^{4}He in confined geometries and superfluid ^{3}He. The torsion pendulums built for the experiments of this dissertation are based on their design.

Principles. Each torsion pendulum consists of a sample cell, which contains a zeolite crystal or a porous silica, and a torsion rod through which ^{4}He is introduced to the cell as shown in Fig. 2.1. When ^{4}He in the cell becomes superfluid, the torsional oscillation of the cell decouples from the superfluid component which has no viscosity. This decoupling increases the resonance frequency of the oscillation.

The resonance frequency f_0 is given by

$$f_0 = \frac{1}{2\pi}\sqrt{\frac{K}{I}}, \tag{2.1}$$

where K is the spring constant of the torsion rod, and I is the moment of inertia of the cell including that of the ^{4}He. A small decrease δI in the moment of inertia due to the

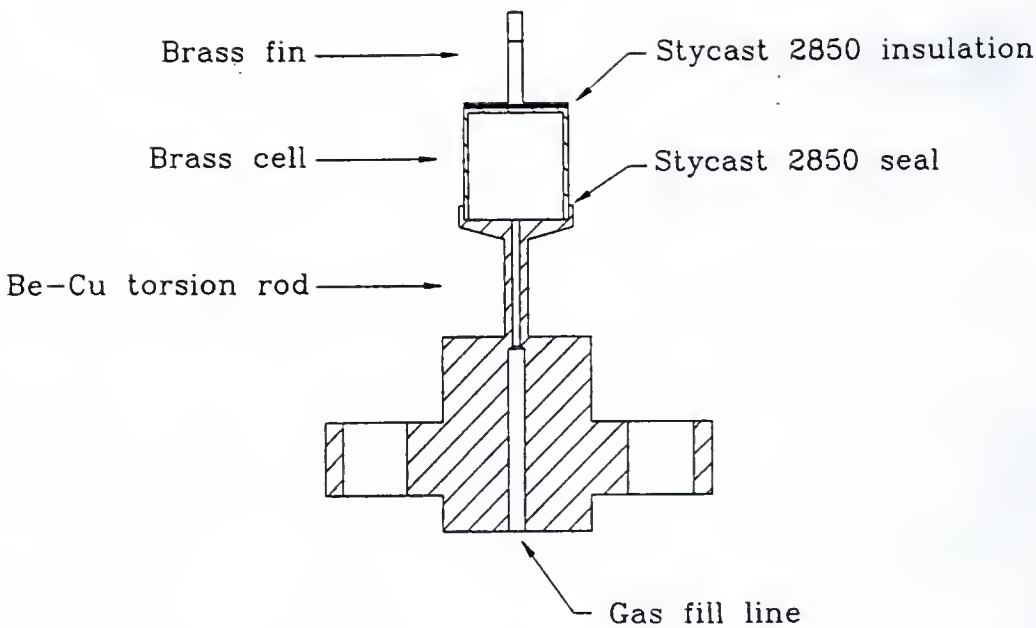

Figure 2.1. Torsion pendulum.

decoupling of the superfluid component produces a frequency increase

$$\delta f = \frac{1}{2\pi}\sqrt{\frac{K}{I}} - \frac{1}{2\pi}\sqrt{\frac{K}{I+\delta I}} \simeq \frac{1}{2} f_0 \frac{\delta I}{I}, \tag{2.2}$$

which is directly proportional to the superfluid density.

Detection of the pendulum oscillation. Figure 2.2 is a schematic presentation of the feedback circuit that drives the torsion pendulum and detects the resonance frequency and the amplitude of the oscillation. The pendulum is driven by the electrostatic force between the drive electrode and the fin attached to the bottom of the sample cell. Another stationary electrode facing the fin from the opposite side is employed to detect the oscillation. The fin is dc biased from 100 to 200 volts for two purposes: (i) to cause the pendulum to oscillate at the drive frequency instead of the first harmonic, and (ii) to make the oscillation produce a current signal. The detected signal is fed back to the drive electrode to maintain the oscillation. Using a low loss material such as a Be-Cu alloy for the torsion rod, one can achieve a Q factor close to 10^6. The very high Q factor is essential to good frequency stability and the detection of small dissipation in ^{4}He .

The bias line is connected to the fin by a thin copper wire (40 AWG). A regular 60/40 soft solder was used to attach the wire to the fin. The soldering was done with care to avoid cold soldering, which not only increases the risk of an open circuit upon cooling but also lowers the Q factor. Care was also taken to avoid prolonged heating which results in a failure of the Stycast 2850FT epoxy that bonds the fin to the sample cell. The wire was cut to a length so that it hung somewhat loosely. Problems such as parasitic resonance modes associated with an oscillation of the biasing wire have not been observed in this arrangement. The 0.1 μF Mylar capacitor between the bias and the cryostat ground

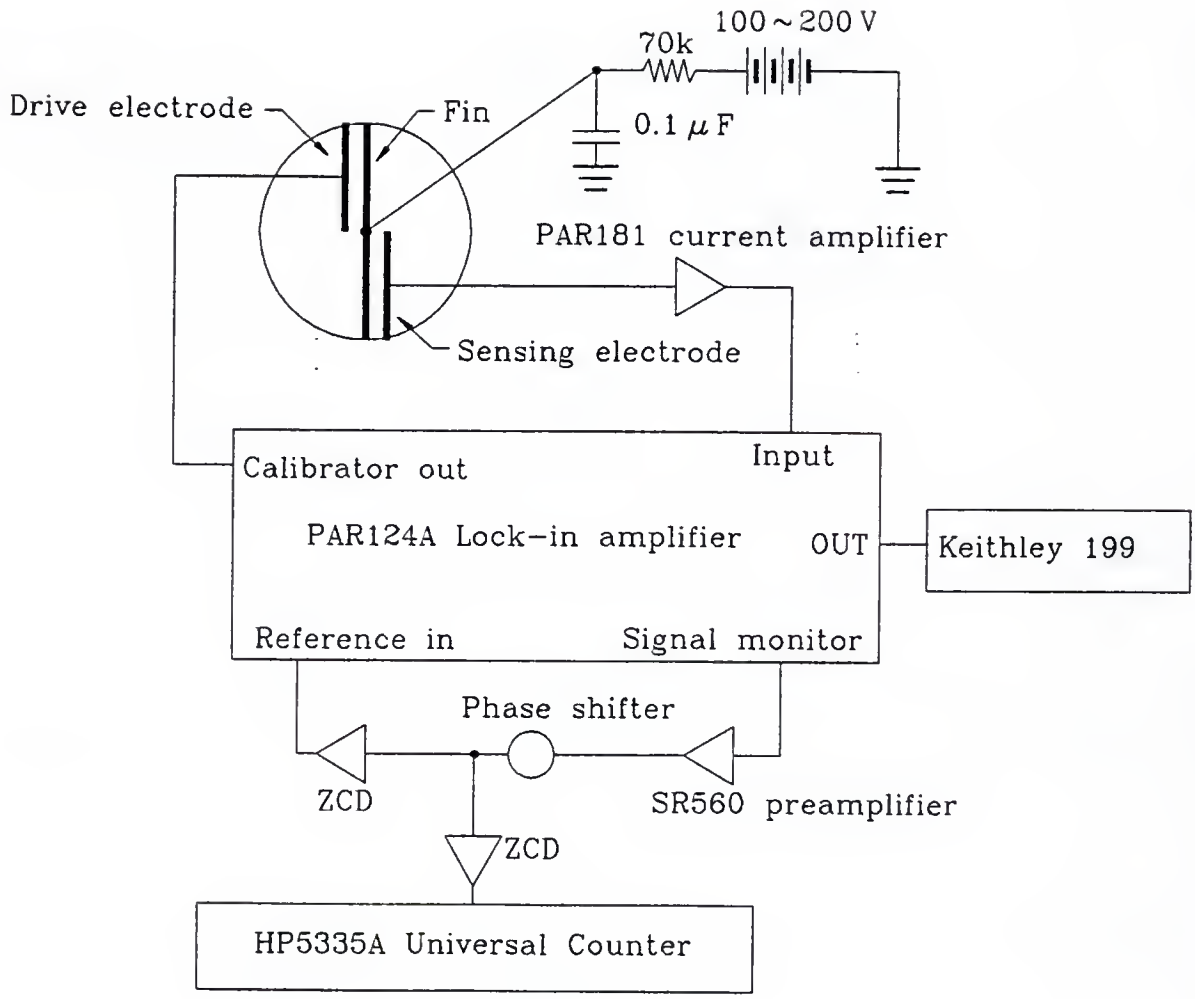

Figure 2.2. Schematic diagram of the torsional pendulum and the feed back circuit.

provides a path for the signal current. The capacitor is located on the base of the vibration isolator which houses the torsion pendulum. A 70 kΩ carbon resistor was placed outside the cryostat in series with the high-voltage source (Bertan 205A-01R [25]) to protect against short circuit to ground and to block the signal current.

Figure 2.3 shows the construction of the electrodes, one for driving the pendulum and the other for sensing the torsional oscillation. Each electrode is a 1/16 inch diameter brass button 0.3 inch in length, glued into a brass case with Stycast 2850FT epoxy. The gap between the electrode and the fin was adjusted manually with a finger or a pushing screw. In order to make the gap as small as possible to obtain a sufficient capacitance, the following method suggested by Nobuo Wada was used. A sinusoidal signal is first fed to the biasing line from which the capacitor and the resistor have been removed. The electrode is then moved in and out while monitoring the signal picked up by the electrode on an oscilloscope. In this way, a typical gap width of 50 $\sim$ 100 μm has been achieved, corresponding to a capacitance of $\sim$2 pF.

Feedback circuit. The home-made coaxial cable for the sensing electrode has a separate thermal anchor and shield from other cables in the cryostat in order to eliminate electronic noise from the thermometer leads and the cable for the driving electrode. It has a separate BNC connector port on the top of the cryostat for the same reason. The room-temperature coaxial cable that connects the PAR 181 current-sensitive preamplifier [26] to the port is made as short as possible to minimize the microphonic noise and the cable capacitance which cuts down the signal. The gain of the preamplifier is set at 10^9 V/A, for which the input impedance is 10 kΩ at frequencies less than 100 kHz. Since the capacitance of the entire sensing line is $C_{\rm line} \sim 220$ pF as measured at the top of the cryostat, with a

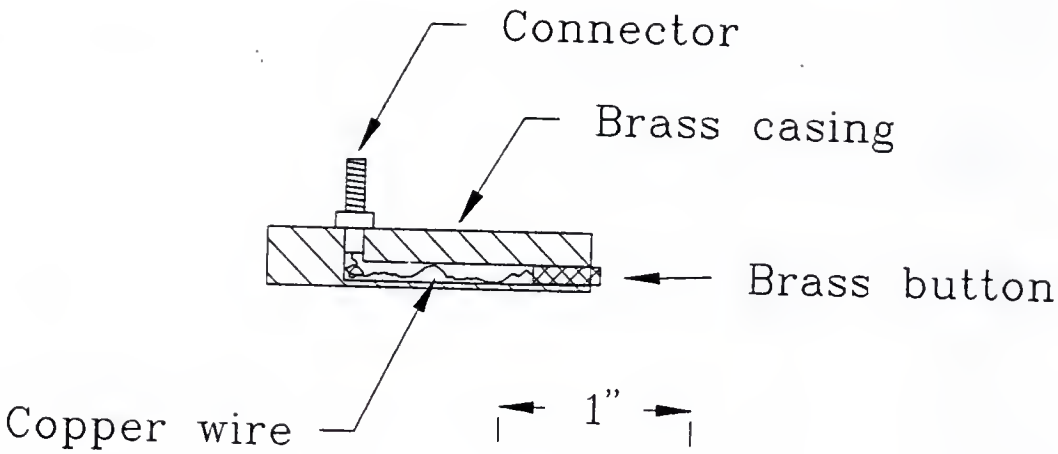

Figure 2.3. Schematics for the sensing and driving electrodes.

corresponding impedance of 145 kΩ for a typical signal frequency of 5 kHz, only about 6% of the signal current is lost through the line capacitance.

The output of the preamplifier goes to a PAR 124A lock-in amplifier [26]. The output of the signal-monitor port of the lock-in amplifier is fed to a home-made phase shifter through a Stanford Research SR560 low-noise preamplifier, which is needed to provide the zero crossing detector (ZCD) with a sufficient level of signal to overcome the noise.

The circuit diagram of the phase shifter is shown in Fig. 2.4. This circuit has been adapted from Horowitz and Hill [27] and consists of two stages. The first stage is a phase splitter which creates a buffered signal and its inverse from the input signal. The CA3026 differential amplifier [1] used for this stage consists of two matched transistors fabricated on a single monolithic substrate to reduce the temperature drift. The second stage combines the two signals through a capacitor and a ten-turn potentiometer. The amount of phase shift can be varied from nearly zero ($R \ll 1/\omega C$) to nearly 180° ($R \gg 1/\omega C$) by adjusting the potentiometer. The amplitude of the output is constant throughout the entire range of the phase. Since the output signal is biased to 11.8 V, a blocking capacitor and a resistor are needed at the output. This RC circuit gives an additional phase shift which should be compensated by the phase shifter.

The signal from the phase shifter is fed to the ZCD, which is shown in Fig. 2.5. The output of the ZCD is connected to the reference input of the lock-in amplifier, in which a phase-locked oscillator creates a sinusoidal signal at the frequency of the reference signal. This sinusoidal signal, after an internal ZCD, is available at the calibrator output, which is directly fed the driving electrode. The output level was set at 0.2 to 50 mV_{rms}, depending on the dissipation in ^{4}He.

[1] Manufactured by RCA.

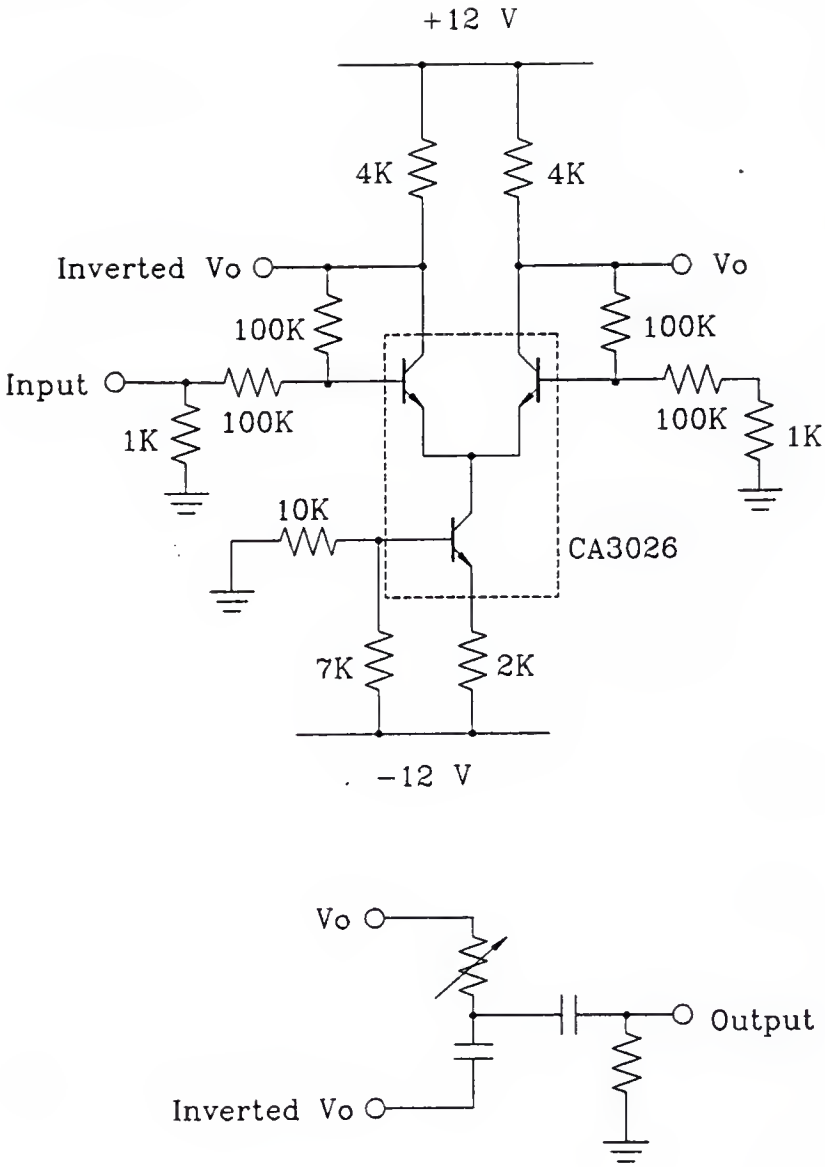

Figure 2.4. Circuit diagram of the phase shifter.

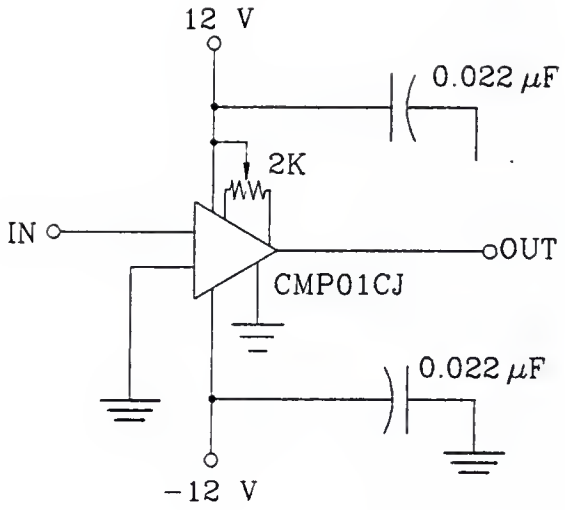

Figure 2.5. Circuit diagram of the zero crossing detector.

Construction of the torsional pendulum. The Be-Cu torsion rod (see Fig. 2.1) was heat treated in vacuum at 320°C for 3 hours for hardening. The sample cell was made of brass. Using light materials like magnesium alloy [9] gives a large relative change in the moment of inertia when ^{4}He becomes superfluid, leading to a larger frequency increase according to Eq. 2.2. However, we could not purchase such an alloy from the manufacturers in a quantity we could afford.

For chabazite experiments discussed in Chapter 4 and Appendix B, a separate torsion pendulum with a separate cell was made for each crystal, since the crystals differed in size. The crystal was glued in the cell with black Stycast 2850FT, which was applied either on a spot or on a line which stretched parallel to the axis of the cell. The reason for not applying Stycast over the entire circumference of the inner wall of the cell was to prevent the thermal contraction of Stycast from damaging the zeolite. Gluing of the crystal was done in a glove bag filled with dry nitrogen gas to prevent adsorption of moisture by the crystal. The torsion pendulum for the porous silica experiment, which is discussed in Chapter 5, was built with a similar procedure except that the silica was coated with Stycast 1266 before being glued in the cell. A detailed description of the construction is given in Chapter 5.

The cell was attached to the torsion rod with Stycast 2850FT in the glove bag. The same epoxy was used to attach the fin to the bottom of the cell. To achieve electrical insulation for the fin it was sufficient to place the fin on a thin layer of the epoxy rubbed on the cell surface without using a spacer. This was done *in situ* on the cryostat. Two dummy electrodes machined to the shape of the actual electrodes were placed against the fin to keep it in the correct alignment with respect to the electrodes while the epoxy cured at room temperature.

Temperature (K)	Q factor	Resonance frequency (Hz)
300	20,000	4794.841
77	68,000	4970.480
4.2	285,000	4992.779

Table 2.1. Changes in the resonance frequency and the Q factor of the torsional pendulum observed during a cooldown from room temperature to 4.2 K. The sample cell, 0.2" in diameter and 0.2" in height, was made of brass and contained chabazite crystal C16 discussed in Appendix B.

Frequency and amplitude of the pendulum oscillation. The frequency of the torsion oscillation can be estimated by using Eq. 2.1. The spring constant of the torsion rod is $K = \pi G(a^4 - b^4)/32L$, where G is the shear modulus of the rod (5.3×10^{11} dyne/cm^2 for Be-Cu), a is the outer diameter of the rod, b is the diameter of the hole, and L is the length of the rod. The estimate of the resonance frequency does not give very accurate values due to machining errors and the uncertainty in the contribution of the epoxy to the moment of inertia. Table 2.1 shows an example of how the frequency and the Q factor change as the pendulum is cooled from room temperature to 4.2 K. The changes are primarily due to the stiffening of the torsion rod as the temperature is lowered. Discussions on other resonance modes and variations of torsional-pendulum design can be found in the textbook written by the Cornell low temperature group [24].

The amplitude of the oscillation can be obtained from the signal amplitude as follows. The signal current I is the time derivative dQ/dt of the electric charge on the sensing electrode. This charge is $Q = CV$, where C is the capacitance between the electrode and the fin and V is the bias voltage applied to the fin. Therefore, the signal current is

$$I = V\dot{C} = -VC\frac{\dot{d}}{d}, \tag{2.3}$$

where the approximation $C \propto 1/d$ has been used since the gap d between the electrode and the fin is much smaller than the size of the electrode. Letting $d = d_0 - \delta e^{j\omega t}$ ($d_0 \gg \delta$) and $I = jI_0 e^{j\omega t}$ leads to the signal amplitude

$$I_0 = V\omega C \frac{\delta}{d_0} \tag{2.4}$$

to first order in δ/d_0; i.e.,

$$\delta = d_0 \frac{I_0}{V\omega C} \tag{2.5}$$

is the amplitude of oscillation. Typical values for the parameters are $I_0 = 10^{-11}$ ampere, $d_0 = 100\ \mu$m, $C = 2$ pF, the bias voltage $V = 200$ volt, and a resonance frequency of 5 kHz for the pendulum, which yields a δ of 0.8 Å near the center of the electrode. The velocity near the edge of the cell is twice the velocity of the fin near the center of the electrode, i.e. $v_{\text{edge}} = 2\omega\delta \sin\omega t$. The maximum velocity $v_{\text{edge}} = 2\omega\delta$ is about 5 μm/sec, which is well below the critical velocity of 6 mm/sec for bulk superfluid ^{4}He of measured by Craig and Pellam [28].

2.2 Thermometry

The temperature of the experiment was measured with a ruthenium oxide resistance thermometer, Bk5p104, which was provided by Mark Meisel [29]. The resistor chip is 0.05×0.05 inch^2 in size and is glued on a 1/16 inch thick copper plate with GE 7031 varnish. Copper leads are attached to the chip with silver epoxy. The chip and part of the leads are covered with Stycast 2850FT for mechanical strength. Figure 2.6 shows the calibration of a resistor from the same batch. Thermometer Bk5p104 had not been calibrated.

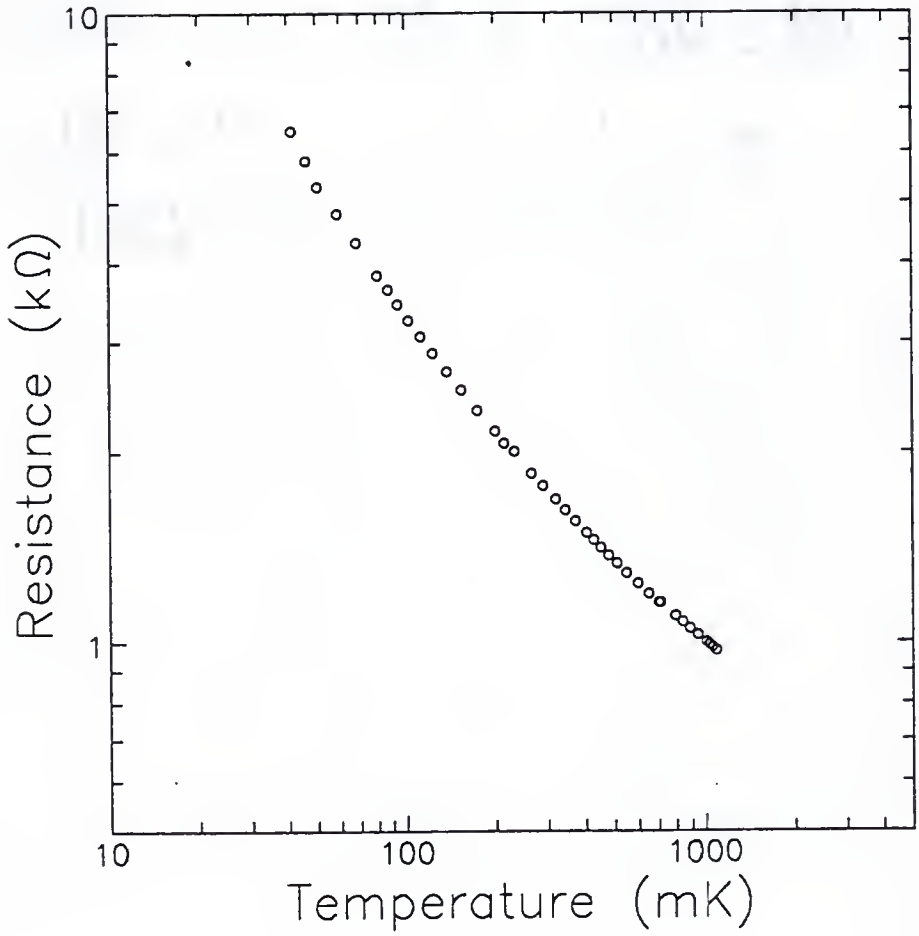

Figure 2.6. Calibration provided by M. Meisel for the ruthenium oxide thermometer Bk5p104, which is representative of the batch from which our thermometer has come.

I have built the Anderson bridge described in Section 2.3 to measure the resistance of the thermometer using a four-lead method. However, two of the four leads lost contact in the first experiment which used a torsional pendulum containing a chabazite crystal as described in Appendix B, forcing us to use a two-lead configuration. In order to keep consistency in the thermometry between this cooldown and the succeeding ones, we chose to use the two-lead configuration until the thermometer was calibrated later in this configuration. Another ruthenium oxide thermometer, Bk6p93, which was loaned to us by Mark Meisel, was installed on the cryostat before the next cooldown to calibrate the first thermometer. The resistance of this thermometer was measured by the dc method in a four-lead configuration. A Keithley 224 current generator was used to provide the 5 nA excitation current for this thermometer, and a Keithley 182 digital voltmeter was used to read the voltage across the thermometer. The current polarity was reversed for every reading to eliminate the effect of the thermal emf, which was about 1 μV. Figure 2.7 shows the calibration for Bk6p93.

2.3 Four-Wire Resistance Bridge

The circuit diagram of the home-made Anderson bridge [24, 31] is shown in Fig. 2.8. Toroidal transformers T_1 and T_2 are placed in separate magnetic shields made of iron. The excitation taken from the reference output of the Stanford Research SR530 lock-in amplifier is fed to transformer T_1, which has two secondaries. One of the secondaries is connected to the op amp OPA-111BM (Burr-Brown) which gives a constant current $I = V/R_s$ to the resistance thermometer R. Here V is the voltage across the secondary, and R_s is the value of the reference resistor. Non-inductive resistors [30] are used for references in order to avoid off-phase components. The other secondary of the transformer is connected to the ratio

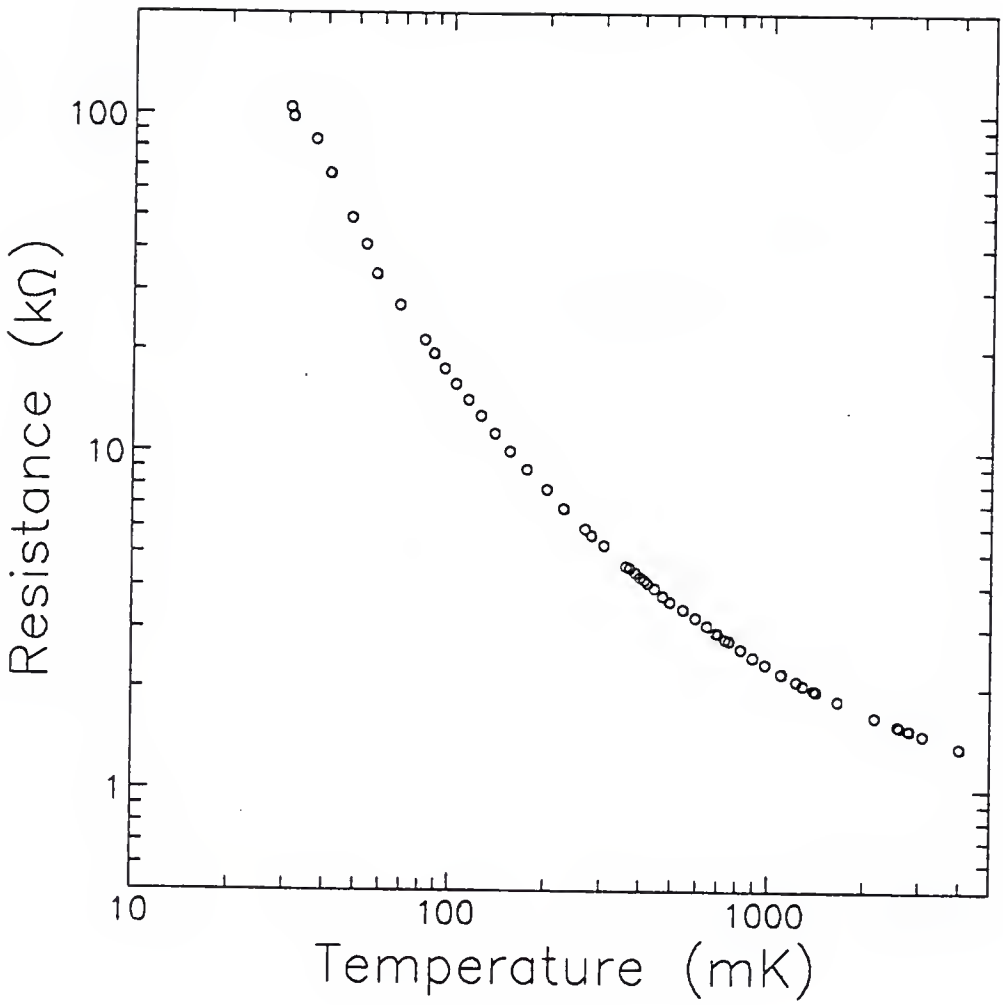

Figure 2.7. Calibration for the ruthenium oxide thermometer Bk6p93. The data were provided by Mark Meisel.

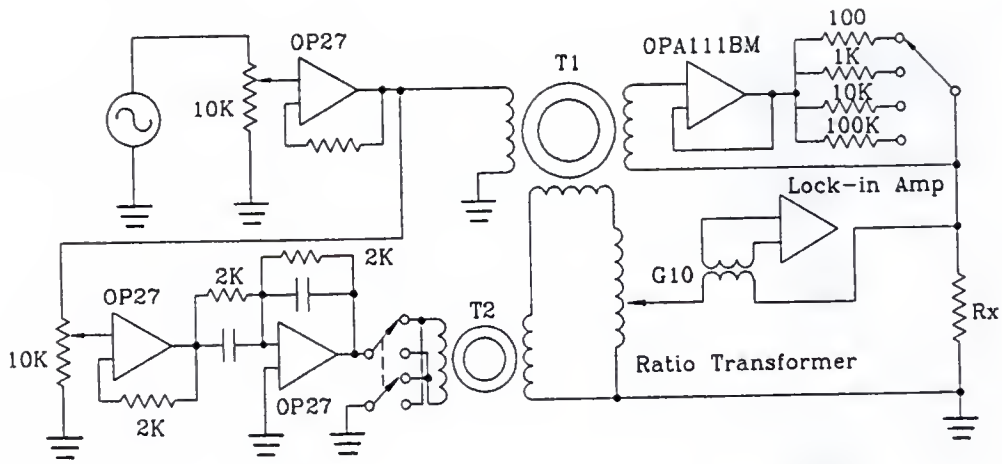

Figure 2.8. Circuit diagram of the Anderson bridge. The reference resistors are Caddock TN137 except for the 100 Ω which is a MK132 [30]. Both types are non-inductive resistors with 1% tolerance.

transformer, whose output is αV when the ratio setting is α, since the quadrature voltage added by transformer T_2 is small in comparison with V. When the bridge is balanced, the output of the ratio transformer and the voltage across the thermometer are the same. Therefore, the condition for the balance is

$$\alpha = \frac{R}{R_s}. \tag{2.6}$$

The bridge has been used mostly off balance to run the experiments under computer control. One can obtain the thermometer resistance from the error signal knowing the setting of the ratio transformer. In order to understand how far the bridge can be used off balance, let us consider the equivalent circuit shown in Fig. 2.9. The secondary of the transformer T_2 for the quadrature has been ignored in this circuit because the resistance change in the thermometer affects only the in-phase component of the bridge. Again the current supplied by the constant current source is I. The current through the primary of the signal transformer for the lock-in amplifier is I', and the current through the ratio transformer is I''. The voltage across the ratio transformer is

$$V = j\omega L(I'' + \alpha I'), \tag{2.7}$$

where L is the total inductance of the ratio transformer. The voltage across the primary inductance L_S of the signal transformer is

$$j\omega L_S I' = R(I - I') - j\omega\alpha L(I' + I''). \tag{2.8}$$

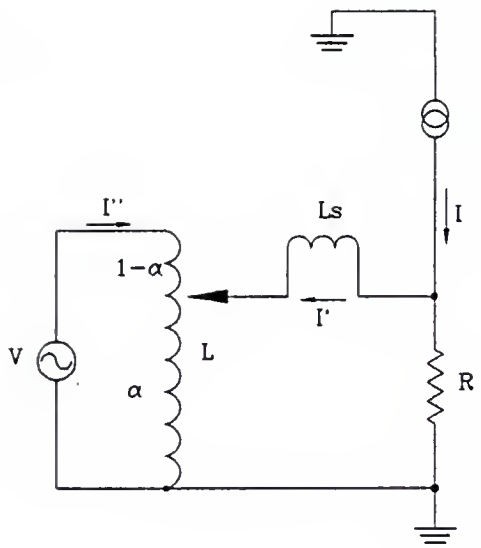

Figure 2.9. Equivalent circuit for the four-wire bridge.

Eliminating I'' from Eqs. 2.7 and 2.8 leads to

$$I' = \frac{RI - (1-\alpha)V}{R + j\omega[L_S + \alpha(1-\alpha)L]}. \tag{2.9}$$

If R_0 is the thermometer resistance for which the bridge has been balanced, then $\alpha V = R_0 I$. When the resistance increases to $R = R_0 + r$ by a small amount r, the error current I' is

$$I' = \frac{rI}{R_0 + r + j\omega[L_S + \alpha(1-\alpha)L]}. \tag{2.10}$$

By expanding the real and imaginary parts of this equation separately in terms of r, one obtains

$$I' = \frac{r}{A}\left\{R_0\left[1 + \left(\frac{1}{R_0} - \frac{2R_0}{A}\right)r\right] - j\omega\left[L_s + \alpha(1-\alpha)L\right]\left(1 - \frac{2R_0}{A}r\right) + \cdots\right\}, \tag{2.11}$$

where

$$A \equiv R_0^2 + \omega^2(L_S + \alpha(1-\alpha)L)^2 . \tag{2.12}$$

Since R_0/A is smaller than $1/R_0$, both the real and imaginary components of the error signal are proportional to r in so far as the resistance change r is a small fraction of the resistance R_0 for which the bridge has been balanced.

The second toroidal transformer T_2, which supplies the quadrature signal to the ratio transformer balances the off-phase component due to the cable capacitance. In order to produce the 90° phase shift, a simple differentiation circuit is used. However, the differentiator becomes unstable at high frequencies, because the total gain increases with frequency as $RC\omega$ and the op amps have internal phase shifts. It oscillated at 21.5 MHz, which was

Core	FT-23-J
O.D. (inch)	0.23
I.D. (inch)	0.12
Height (inch)	0.06
Permeability	850

Table 2.2. Specification of ferrite cores. The data are from *Iron-Powder and Ferrite Coil Forms* published by Amidon [32].

killed by inserting an extra resistor and capacitor. The phase-shifter looks like an integrator at high frequencies because of these additions.

We have found that the ferrite core of T_2 adds an unwanted phase shift to the quadrature. Figure 2.10 shows the phase shift as a function of frequency. The phase shift is probably caused by loss in the core which depends on the material and geometry of the core. The core used for the transformer T_2 is Amidon FT-23-J [32]. The specifications for material J are given in Table 2.2. The windings are 70 turns for the primary and 11 turns for the secondary. The inductance of the primary and secondary are 4.8 mH and 0.12 mH, respectively.

2.4 Data Acquisition

Two computer programs were written in Quick BASIC [33] to take data. Program TORCONT.BAS takes data at high temperatures where the frequency does not change very much. This program takes data on the fly, without using active temperature control. The rate of temperature change is controlled manually by partially closing a valve on the still pumping line of the dilution refrigerator and increasing the heater levels on the experimental stage and mixing chamber. The gate time of the frequency counter (see Fig. 2.2) is set at 2 minutes by the program. The error signal from the Stanford Research

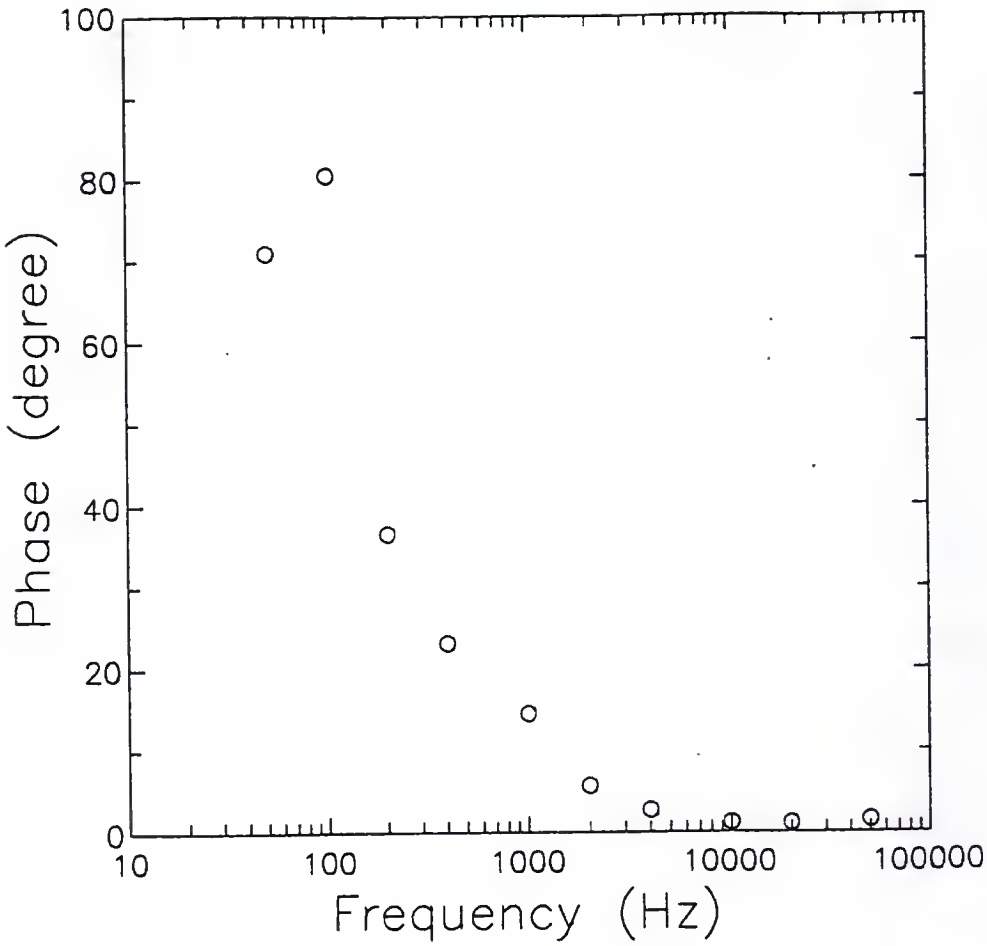

Figure 2.10. Phase shift caused by the ferrite cores as a function of frequency.

SR530 lock-in amplifier of the Anderson bridge is converted to a resistance by the program. The conversion of resistance to temperature is done after the experiment.

The second program TORAUTO.BAS takes data with temperature regulation using an ATC temperature controller manufactured by S.H.E. Since the Anderson bridge does not automatically balance itself, the internal offset of the lock-in amplifier is used to offset the error signal by an amount appropriate for the target resistance value. In order to get the correct offset value, the error signal for various ratio transformer settings has been measured at several temperatures by holding the mixing-chamber temperature constant. Figure 2.11 shows the ratio of the resistance difference to the voltage output of the lock-in amplifier as a function of the thermometer resistance. The ratio is a linear function of the resistance except in the lowest resistance region.

After it sets the offset for a new temperature, the program waits for the temperature to stabilize by monitoring the error signal. When the error signal indicates the resistance to be within 0.01% of the target value for four consecutive readings which are a few seconds apart, the program opens the gate of the frequency counter for 2 minutes. The temperature remains stable within 3 mK around 1 K during the data taking. While the gate is open, the amplitude of the torsion pendulum signal and the error signal of the Anderson bridge are read continuously by a Keithley 199 System DMM scanner. Both quantities are averaged by the computer and written to data files.

When thermometer Bk6p93 was installed before the second cooldown to calibrate Bk5p104, the two programs were modified to read the resistance of this thermometer before and after each frequency count.

TORAUTO.BAS was later modified and renamed as TORSION3.BAS for the torsional pendulum experiment using porous silica discussed in Chapter 5. The modified program

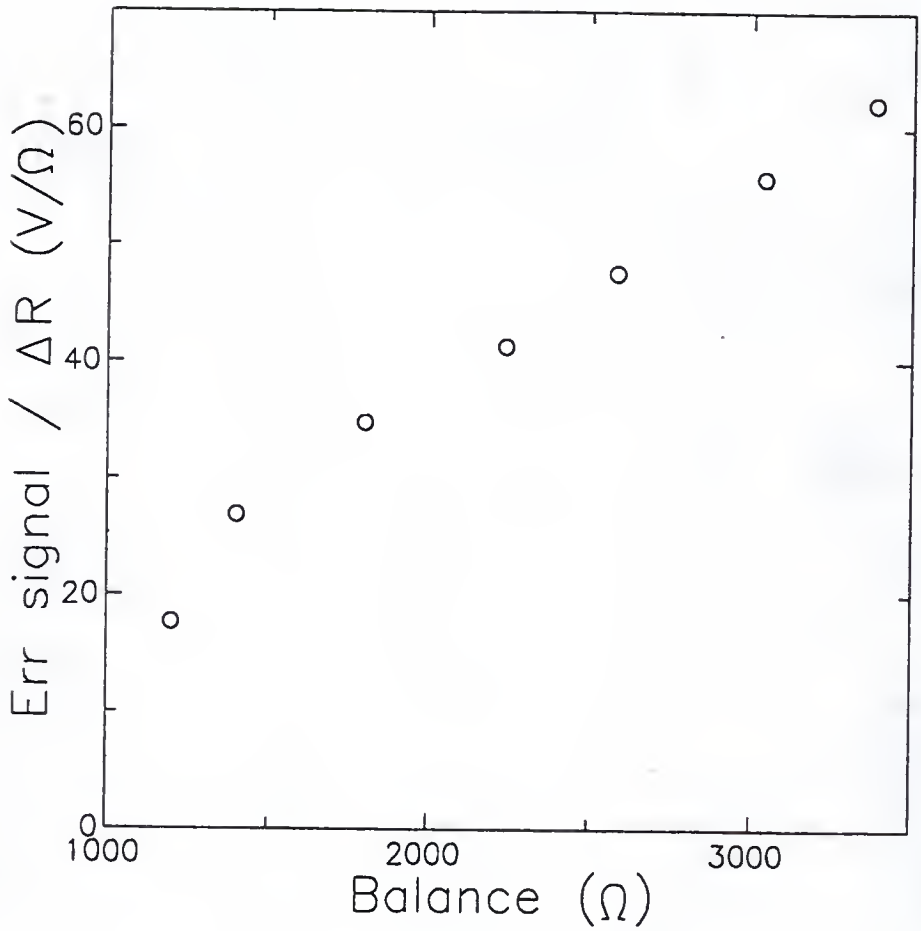

Figure 2.11. Ratio of the error signal to the resistance difference as a function of the thermometer resistance. The sensitivity of the lock-in amplifier was 20 mV. The oscillator was set at 10 Hz and 0.1 V.

records the readings of the torsion pendulum amplitude and the Anderson-bridge error signal in separate files for later analysis in addition to the averaged amplitude and the thermometer resistance. It also takes three frequency readings at each temperature to check the frequency stability. This program controls the heater on the mixing chamber as well as the heater on the experimental stage to eliminate a possible temperature gradient between the two stages. Since the ruthenium oxide thermometer Bk6p93 is located closer to the mixing chamber than Bk5p104, the temperature gradient may result in lower temperature readings for Bk6p93.

The program was later modified again to use Bk6p93 for temperature regulation when one of the leads for Bk5p104 became grounded during the experiment. The modified program calculates the appropriate heater output by simulating a PID temperature controller and sets the heater level through a D-to-A converter. The temperature of the experimental stage was regulated to within 3 mK by this method.

2.5 Cryostat

The cryostat, except for the dilution unit and part of the gas handling system, was purchased from BTi when they quit the dilution refrigerator business.

Vibration isolation. The vibration isolation of the cryostat is provided by two components. One is the concrete wall in which the plumbing from the gas handling system to the cryostat is embedded. The top of the wall is filled with dry sand to completely cover the plumbing. This wall helps to reduce the vibrations which originate from the mechanical pumps located in the crawl space under the laboratory. The other component of the vibration isolation is the floating table. The aluminum table is attached to three PVC sewage tubes, 16 inches in diameter and 5 feet 8 inchs in height, filled with concrete. Each

of these columns sits on an air spring which is placed in the aluminum base of the column. However, we have found that the bottoms of the columns started to slide sideways when the air spring was inflated to ~100 psi. Because of this problem the air springs have never been used in the actual experiments.

It is quite likely that the top of the columns are not flat. Since the aluminum table is bolted onto each column with a rubber sheet between them, the bottoms of the columns can slide. If this is the case, a possible solution is to grind flat the top surface of each column and to insert a thick metal plate under each rubber sheet so that the top surfaces of the plates are level and parallel to the table. It is also possible to guard the bottom of the columns with small air springs.

The vibrations generated by the mechanical pumps are also intercepted by sand boxes before they reach the gas handling system. These are wooden boxes 30 cm × 30 cm × 30 cm in size, each with a hole on the bottom for the plumbing. The gap between the hole and the plumbing is sealed with silicon caulking to avoid direct contact. As is well known, the sand should be kept dry to be effective.

Dilution unit. There are many good reviews on dilution refrigerators [24]. Figure 2.12 shows a schematic diagram of the dilution unit used in the experiments of this dissertation.

The still is made of copper and has a volume of 62.5 cm^3. The return line capillary is coiled inside the still to cool the liquefied ^3He to the still temperature. The first still that I constructed started to leak one week after the first cooldown of the refrigerator. The leak was found at the soft solder joint between the base plate of the still and the body. Soft solder had been used so that the joint could be undone later in case of a problem. However, it seemed that the solder was not strong enough to withstand the stress of differential thermal

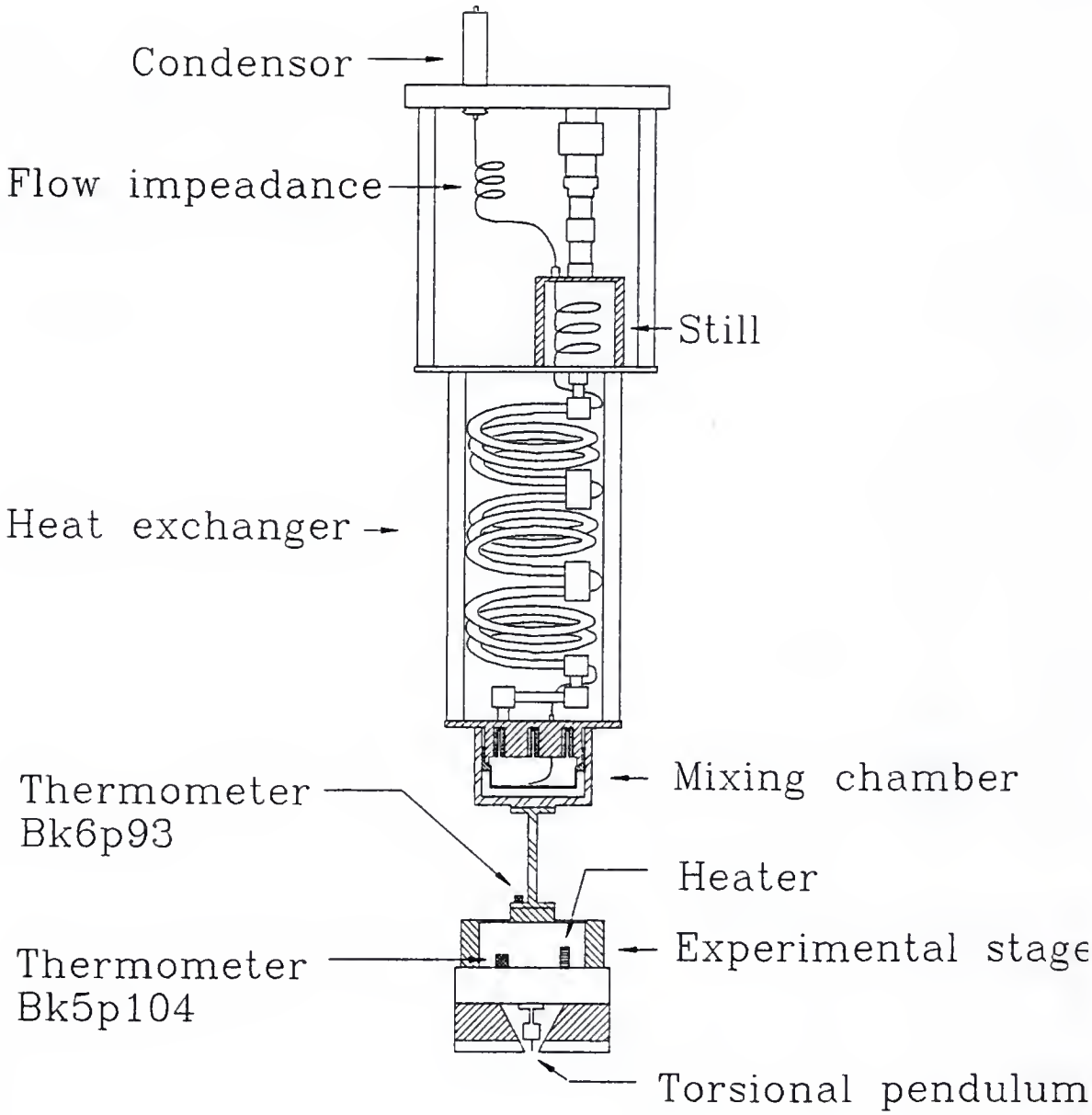

Figure 2.12. Schematic of the homemade dilution refrigerator.

contraction. Resoldering did not solve the problem. A new still with the same design was assembled with silver solder but also leaked at the same joint. Grinding away the leaky part and filling it with soft solder did not eliminate the leak. After spending many days trying to fix the leak, it was finally decided that the problem with the still design was the bulkiness of the body, which had 0.3 inch thick walls and weighed about 620 g. Following this diagnosis, yet another still with a smaller mass was built. In the new design, the wall thickness was reduced to 0.2 inch and all the edges were milled down as much as possible, reducing the mass to 480 g, whereas the inner volume was reduced by only 5%. In order to make stronger solder joints, the edges of the indentation on the base plate have been raised by 1/16 inch, 1/32 inch wide. The new still has worked well without a leak.

The heat exchanger is a continuous type of the tube-in-tube design using stainless steel tubes of two different diameters. It consists of three segments connected in series by two copper blocks and silver soldered together. The copper blocks are to provide convenient thermal anchoring for leads and cables. Each segment is manufactured in the following sequence. First a 0.03 inch diameter capillary is formed into a coil by wrapping it around a 1/16 inch tube. After inserting the coiled capillary into a 3/16 inch tube, the latter is filled with water and plugged on both ends with Apiezon Q [34]. Finally, the entire assembly, which is about 45 inches long, is dipped into liquid nitrogen to freeze the water and is bent into a 2.3 inch diameter coil with a pitch of about 0.3 inch by wrapping it around a 2 inch copper tube.[2] The frozen water in the tube prevents the cross section from collapsing during the bending. During the assembly of these segments into a single unit, it was difficult

[2]This freezing technique was also tried on the capillary to prevent flattening during the coiling, but it was abandoned after one try. The problem was that the ice started to melt immediately during the handling of the capillary.

to keep the stainless-steel tubes away from the direct flame of the torch during the silver soldering. Because of several leaks, I had to discard one of the coils and make a new one.

The flow impedance between the still and the ^{3}He condenser was made by inserting a 0.0089 inch diameter Cu-Ni wire into a 4.7 inch piece of Cu-Ni capillary with a 0.01 inch inner diameter and by stretching the capillary from both ends with pliers until the desired impedance value of 1.1×10^{12} cm^{-3} was obtained. The impedance was measured by immersing one end of the capillary in methanol and connecting the other end to a nitrogen gas cylinder. By collecting the nitrogen bubbles in a graduated glass tube, the flow rate was determined. The impedance Z was obtained from the flow rate $\dot{V}_2$ (cm^3/sec) by using the relation

$$Z = \frac{1}{2\eta\dot{V}_2 P_1}(P_1^2 - P_2^2)\,, \tag{2.13}$$

where P_1 is the applied pressure of nitrogen and P_2 is the atmospheric pressure. The kinematic viscosity η of nitrogen gas at room temperature is 18.9 μPa·sec.

The upper part of the mixing chamber is made of OFHC copper for good thermal conduction. The part has sixteen 0.95 cm diameter holes packed with 700 Å silver powder [35], which was provided by Dwight Adams. The powder has been heated in vacuum at 300°C for 30 minutes to increase the grain size. The surface of the holes had been electroplated with silver prior to the packing to improve the adhesion of the powder to the copper. A hole of 0.64 cm diameter was drilled in the center of each powder-packed hole. The bottom of the mixing chamber is made of brass.

The Vespel SP22 [36] insulators are used on the supports between the mixing chamber and the still[3]. Each insulator's outer diameter is 1 cm, the inner diameter is 0.43 cm, and

[3]Vespel SP22 is a ployimid resin containing 40% by weight of graphite.

the height is 1.27 cm. Two insulators are used on each support on the mixing chamber side. Heat leak through the Vespel insulators can be estimated by considering a one dimensional heat conduction problem. The heat flow $\dot{Q}$ through a material with a uniform cross section A follows the equation

$$\dot{Q} = -A\kappa(T)\frac{dT}{dx}, \tag{2.14}$$

where κ is the thermal conductivity and dT/dx is the temperature gradient. The thermal conductivity of Vespel SP22 is $\kappa = kT^2$, with $k = 17\ \mu$W/cm/K [37]. Since $\dot{Q}$ is constant over the length of the rod, integrating Eq. 2.14 leads to

$$\dot{Q} = \frac{Ak}{3L}(T_H^3 - T_L^3), \tag{2.15}$$

where L is the length of the rod. The high temperature end T_H is at about 0.6 K, a typical temperature of the still, and the low temperature end T_L is 80 mK. From Eq. 2.15, the heat leak through one Vespel insulator is estimated to be $\dot{Q}$=0.62 μW. Since there are six of them, the total heat leak into the mixing chamber through the Vespel is 3.7 μW.

Thermometers. The operation of the dilution refrigerator was monitored with six carbon resistance thermometers and one ruthenium oxide thermometer Bk7p27, which were read by the LR110 resistance bridge [38] through a home-made connector box. The location and typical resistance value of each resistor is summarized in Table 2.3.

The lowest temperature achieved with this refrigerator is 78 mK, according to the thermometer Bk7p21 attached to the mixing chamber. This is disappointing, since a good dilution refrigerator can reach 20 mK with a continuous heat exchanger alone. The reason

Thermometer	Location	R_{300} (Ω)	R_{77} (Ω)	$R_{4.2}$ (Ω)
$1K_H$	Cold plate	145.8	163.4	1024.7
$1K_L$	Cold plate	105.1	107.1	117.1
Still	Still	146.0	149.0	142.5
HE	Heat exchanger	146.6	146.0	118.5
MC_{out}	Outside mixing chamber	138.1	140.4	119.9
MC_{in}	Inside mixing chamber	123.1	119.0	64.3
Bk7p21	Outside mixing chamber			

Table 2.3. Resistance values of the thermometers at room temperature, nitrogen temperature, and helium temperature. The resistors except $1K_H$ and Bk7p21 are Matsushita 47 Ω. $1K_H$ is Allen Bradley 100 Ω. The ruthenium oxide thermometer Bk7p21 was provided by Mark Meisel. Each resistor except MC_{in} and Bk7p21 have been ground on two sides with sand paper and attached to a 1/16 inch thick copper plate with GE 7031 varnish. A 0.004 inch thick Mylar sheet has been placed between the resistor and copper plate for electrical insulation.

for the high base temperature is not understood at the moment. Suspecting that ^{3}He does not liquefy completely at the condenser attached to the cold plate, I have installed an extra ^{3}He condenser in series to the existing one. This has not improved the performance of the refrigerator.

Volume of each part of the cryostat. The volume of each part of the cryostat and the estimated amount of helium gas are listed in Table 2.4 for the diagnostic purposes of future users.

Coaxial cables and the thermal anchors. Home-made coaxial cables are used for the vapor-pressure thermometer, torsion pendulum, and ruthenium oxide thermometer Bk5p104 placed on the experimental stage. The capacitance of each coax cable is 34 pF/m. The outer conductor of each cable is a Cu-Ni tube with a 0.037 inch o.d. and 0.027 inch i.d. The insulator of the inner conductor is provided by a TFE tube pulled off from hook-up

	Volume (cc)	Condition	^{3}He (liter)	^{4}He (liter)
Still	62.5	dil.	0.289	40.38
M.C. (inside the sponge)	9.12	conc.	5.47	
M.C. (outside the sponge)	30.62	dil.+ conc.	1.86+1.16	17.81
H.E. out	43.45	dil.	2.01	28.07
H.E in	0.9	conc.	0.54	
^{3}He filter 1K	3.1	conc.	1.86	
^{3}He filter 4K	16.5	gas at 4 K	0.38	
Leybold exhaust filter	1,700	gas	0.57	
ED500 mechanical pump	2,000	gas	0.67	
ED500 exhaust filter	200	gas	0.067	
Cold trap	851	gas at 77 K	1.00	
Cold trap tube	56.9	gas	0.2	
Return line	210.2	gas	0.07	
Return line to cryostat	3.86	gas	0.09	
Total			16.2	82.3

Table 2.4. Volume of each part of the refrigerator and gas handling system. 'dil.' indicates the dilute ^{3}He phase, for which 6.4'conc.' indicates the ^{3}He rich phase. The amounts of ^{3}He and ^{4}He are in liter of gas at STP.

wire (Alpha 30 AWG, Cat. No. 2841/1 WHT) following a recipe of Olivier Avenel. The inner conductor of each coaxial cable that runs from the top of the cryostat to the top of the vacuum can is a 0.003 inch diameter Advance wire with 46.1 Ω/ft resistance.[4] The resistance of the inner conductor is about 200 Ω for each cable. Each cable below the top of the vacuum can uses superconducting wire for the inner conductor.[5]

Male MALCO connectors (Part No. 142-0002-0001) were used on both ends of each cable. I first made the mistake of using liquid soldering fluxes such as Superior No. 50 and No. 30 to solder the connector to the inner conductor. Although these are not highly corrosive fluxes, they are slightly conductive. I was suprised to find voltages from to 60 to

[4]Advance wire is too soft to put through the TFE tube. Karma wire of the same diameter was put through the tube first as a guide. Advance wire was glued to the end of the Karma wire and was pulled through.

[5]Mono filament NbTi with a Cu-Ni matrix, with a 0.0042 inch diameter from Supercon [39].

100 mV between the inner and outer conductor.[6]. This emf was eliminated by switching to a rosin flux. Always use a rosin flux for electrical joints!

Nine home-made thermal anchors are attached to the top of the vacuum can, the cold plate, and the mixing chamber, in order to reduce the heat leak along the coaxial cables from room temperature without exposing the inner conductor of the cables. Figure 2.13 illustrates the interior of the anchor, which consists of a body, a cover, a Kapton sheet with strips of copper conductors, and four or five female MALCO connectors (Part No. 141-0002-0002) on each side. The copper conductors have been made by the standard etching procedure for a copper-plated Kapton sheet. The sheet has been glued with GE 7031 varnish onto the bottom of the box with the copper strips facing down, with a 0.004 inch thick Mylar film for electrical insulation. Each thermal anchor adds 1.8 Ω to each cable.

2.6 Sample Gas-Handling System

Figure 2.14 shows the schematic of the gas handling system used to introduce ^{4}He gas into the sample cell and vapor-pressure thermometer. The reference volume is 2.92±0.01 cm^3, which has been calibrated against a 29.01 cm^3 standard volume. All tubes on the gas handling system stainless steel with a 1/16 inch in o.d. and 0.03 inch in i.d. from HIP [40]. A Paroscientific model 223AT pressure transducer [44], whose pressure range is from 0 to 158 kPa, is used to measure the amount of gas introduced into the sample cell and to calibrate the vapor-pressure thermometers. The transducer gives two frequencies, which are measured with a two-channel frequency counter and converted to a pressure P in psia according to the formula given in Table 2.5 as provided by the manufacturer.

[6]Same effect has been seen with other liquid soldering fluxes such as Superior No.72 and La-Co Brite soft solder flux.

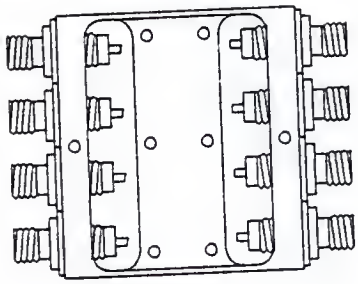

Figure 2.13. Interior of the thermal anchoring box for the coaxial cables.

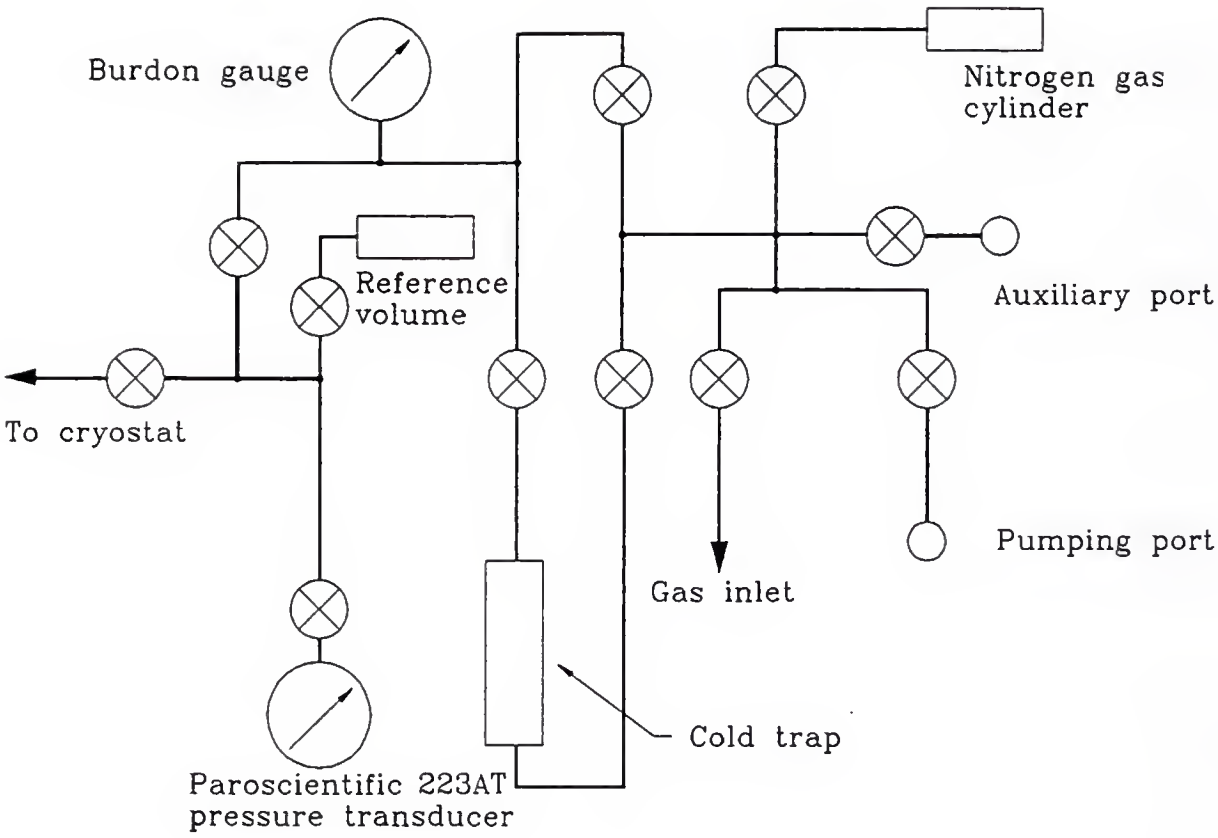

Figure 2.14. Gas-handling system. All connections are made of stainless steel tubes 1/16 inch o.d. and 0.03 inch i.d. The valves, the connectors, and tubes are from High Pressure Equipment Company [40].

$$
\begin{aligned}
P &= C(1 - \frac{T_0^2}{\tau^2})[1 - D(1 - \frac{T_0^2}{\tau^2})] \\
C &= C_1 + C_2 U + C_3 U^2 \\
D &= D_1 + D_2 U \\
T_0 &= T_1 + T_2 U + T_3 U^2 \\
U &= \tau_t - U_0
\end{aligned}
\tag{2.16}
$$

Coefficient	Value	
C_1	123.2387	psia
C_2	11.37897	psia/μsec
C_3	150.0802	psia/μsec^2
D_1	0.0446672	
D_2	0.0000000	
T_1	25.05889	μsec
T_2	0.6601851	
T_3	18.75280	μsec^{-1}

Table 2.5. Formulae and coefficients of calibration for the Paroscientific 233AT pressure transducer (S/N 35884) [41]. The data are from the Paroscientific calibration sheet. The calibration accuracy is 0.015 % over the entire pressure range. τ_t is the temperature period and τ is the pressure period in μsec.

The reproducibility of the pressure transducer is better than 8 Pa according to the manufacture. However, the long term stability is limited by the 2°C fluctuation of the room temperature. This is not a problem for measuring the amount of gas for the torsion pendulum, a task which takes less than 15 minutes. However, when the gas-handling system is used for the adsorption isotherm, which is discussed in Section 3.2, a drift has been observed due to changes in room temperature.

CHAPTER 3
CHABAZITE DEHYDRATION TECHNIQUE

This chapter describes the techniques developed to dehydrate the chabazite crystals used in the torsional-pendulum experiments discussed in Chapter 4 and in Appendix B. There are about 200 species of synthetic zeolites and 42 known species of natural zeolites [42]. Chabazite has been chosen from this zoo of zeolites as a substrate for ^{4}He in our experiments for two reasons. First, large crystals of chabazite up to about 1 cm in size are relatively easy to obtain, unlike all synthetic zeolites which are typically 10 μm or less in size, and many other natural zeolites are rare. In torsion pendulum experiments, a large crystal of at least a few millimeters in size is necessary to get reasonable sensitivity for the superfluid density of adsorbed ^{4}He. If a cell is packed with zeolite powder instead of a large crystal, most of the adsorbed helium will move with the motion of the grains, resulting in very poor sensitivity. Second, chabazite is very stable at temperatures up to about 800°C [43], unlike some zeolite species such as yugawaralite, which changes its crystal structures upon dehydration. Chabazite can be dehydrated without any irreversible deformation of the crystal.

To my knowledge, all dehydration techniques developed for zeolite prior to this dissertation involved either heating the crystals in vacuum or in air, or, in a few cases, prolonged evacuation at room temperature. Small synthetic crystals such as ZSM5 [44, 45] or zeolite Y, which are typically 10 μm or less in size, maintain structural integrity during heating, but it was not at all clear when we started this work whether crystals of millimeter sizes

could stand such processes. To our surprise, we found that chabazite crystals are pulverized even by heating to a temperature too low for dehydration. The high-pressure dehydration technique we have developed to solve this problem is unique and will certainly find an application in the manufacturing of molecular-sieve filters. The technique will probably be useful also for removing solvents from other porous media for which supercritical drying is inapplicable. For these reasons, descriptions given in this chapter are detailed, perhaps too detailed for a thesis in low temperature physics, to benefit those who may want to further refine the technique with applications in mind.

3.1 Chabazite

Chemical composition and structure of chabazite. The unit cell composition [42] of idealized chabazite is $Ca_2[(AlO_2)_4(SiO_2)_8]\cdot 13H_2O$. In reality, the chemical composition of chabazite can vary depending on the locality. The crystal is rhombohedral [46, 47] and each unit cell contains a cage shown in Fig. 3.1. Each cage is connected to six neighboring cages as shown in Fig. 3.2, each through an aperture made of a single 8-membered ring of eight Si and Al atoms bonded by oxygen atoms.

The aperture is 3.1×4.4 Å ^{2} in size and allows the passage of ^{4}He atoms whose diameters are 3 Å. The top and the bottom of the cage have double 6-membered rings made of eight Si and four Al atoms bonded by oxygen atoms. The aperture size of the double 6-ring is 2.6 Å, which is smaller than ^{4}He. The height of the cage is 10 Å and the width is 6.7 Å. Each cage can accommodate about fourteen ^{4}He atoms. There are two Ca^{2+} ions per cage with three types of sites at which the ions are located [47]. Site I is at the center of the double 6-membered rings, invisible to ^{4}He adsorbed in the cage. Site II is on the exterior of the double 6-membered rings. Site III is near a 4-membered ring which connects the

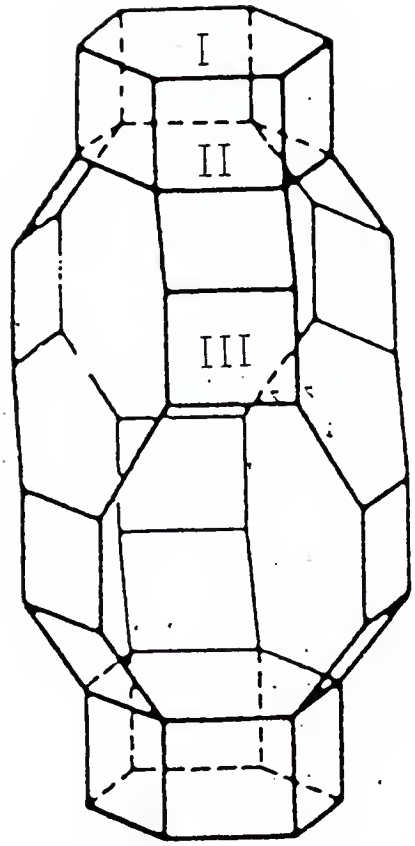

Figure 3.1. Cage structure of chabazite after Barrer [48]. Oxygen atoms are located between Si and Al atoms, which occupy the apexes. I, II, and III indicate Ca^{2+} ion sites.

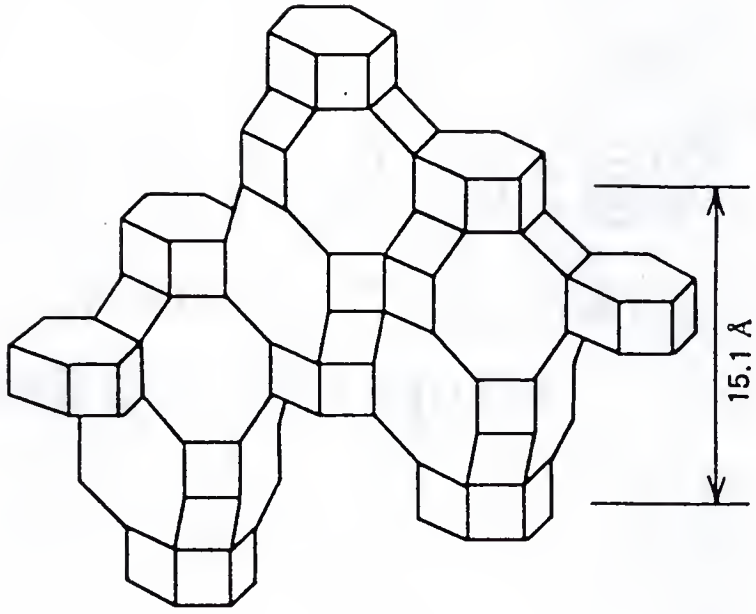

Figure 3.2. Framework structure of chabazite after Ruthven [49]. A Si or Al atom is located at each apex, and an oxygen atom is located in the middle of each line.

double 6-membered rings to a single 8-membered ring. There are one site I, two sites II, and twelve sites III in each cage. The occupancy rate of Ca^{2+} ions is 0.6 for site I, 0.35 for site II, and .0625 for site III [47]. The cages are filled with water molecules which are part of the crystal structure and need to be removed before introducing ^4He .

3.2 Vacuum Dehydration of Chabazite and Nitrogen Adsorption Isotherm.

The first approach we took was to simply heat the chabazite crystals in vacuum, as is most commonly done to dehydrate zeolite. This was done in a Thermolyne 21100 tube furnace and a home-made furnace. The latter consisted of a 2" diameter Pyrex tube on which a 10 ft length of nichrome wire with a 1.07 Ω/ft resistance was wound. Glass wool and glass tape were wrapped around the tube for thermal insulation, with a window about 1 cm in size to provide a view of the samples during heating. The samples were placed in a Pyrex cell. The temperature of each furnace was measured by a copper-constantan thermocouple placed in the tube. Each furnace was connected to a diffusion pump which maintained a pressure of about 10^{-5} Torr during the heating.

Nitrogen adsorption isotherm. A method often used to determine the amount of water removed from zeolite is simply weighing the crystals before and after dehydration. However, the chabazite crystals broke during heating into small pieces, some of which tended to stick on the wall of the Pyrex cell. This made accurate weighing of the crystals difficult after dehydration. Furthermore, weighing dehydrated crystals required a balance in a dry, protected atmosphere, which is a non-trivial measurement.

As a better alternative, the adsorption isotherm of nitrogen gas was measured at 77 K. The gas handling system used for the measurement was the same one used to introduce the sample ^4He gas to the cryostat described in Chapter 2 (See Fig. 2.14). Figure 3.3

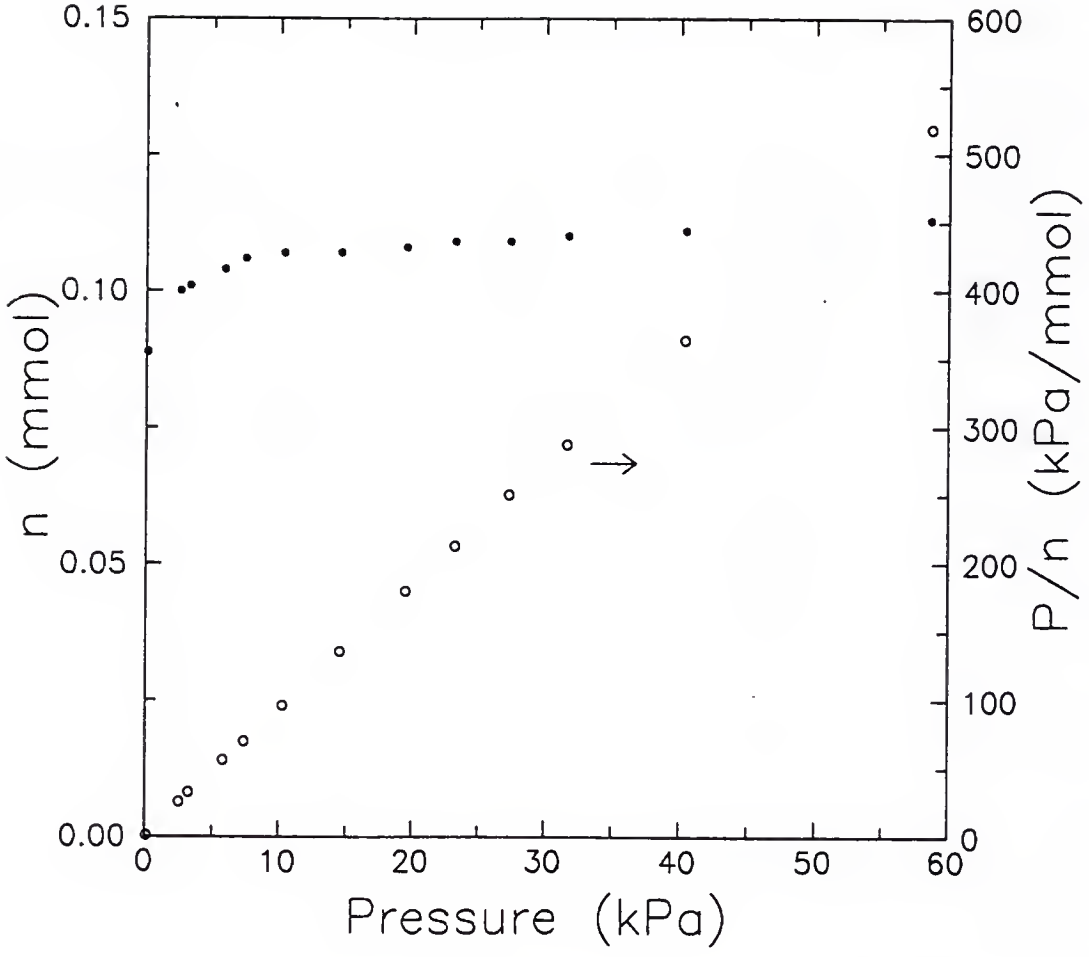

Figure 3.3. Adsorption isotherm of nitrogen at 77 K on chabazite dehydrated in vacuum at 320°C. The dashed line is a fit to the Langmuir model.

shows an example of a nitrogen adsorption isotherm, taken from run A listed in Table 3.1. The isotherm appears to be type I according to Brunauer's classification [50] as commonly found for zeolite, indicating that the pore size is not much larger than the molecular size of the adsorbate. The figure also shows P/n as a function of pressure P, where n is the adsorbed amount of nitrogen gas. The linear relationship between P/n and P indicates good agreement with the Langmuir model [51],

$$\frac{P}{n} = \frac{1}{bn_s} + \frac{P}{n_s}, \tag{3.1}$$

where b is an adsorption constant and n_s is the amount of nitrogen gas at saturation. Fitting the data to this equation gives 0.113 mmol for n_s and $(1.9 \pm 0.6) \times 10^{-3}$ Pa^{-1} for b. The full-pore amount of nitrogen obtained from n_s is 7.05 mmol per 1 g of the original chabazite crystal before dehydration, corresponding to 7.3 nitrogen molecules per cage. This corresponds to 88reported by [42].

Results of vacuum dehydration. Table 3.1 is a summary of the results of vacuum dehydration. Figure 3.4 shows the heating curves. Runs A through G were done in the Thermolyne furnace. The results show that a significant amount of water starts to come out from chabazite at a temperature between 220°C and 230°C, and the crystal can be completely dehydrated at 300°C in a very short time. Chabazite was pulverized in all these runs regardless of whether or not water was removed except for run B in which the maximum temperature was only 50°C.

In particular, chabazite was pulverized even at 80°C, a temperature far too low for dehydration. It is clear that the pulverization of chabazite is not associated with the removal of water. Although what breaks the crystals is unclear, at least one can exclude

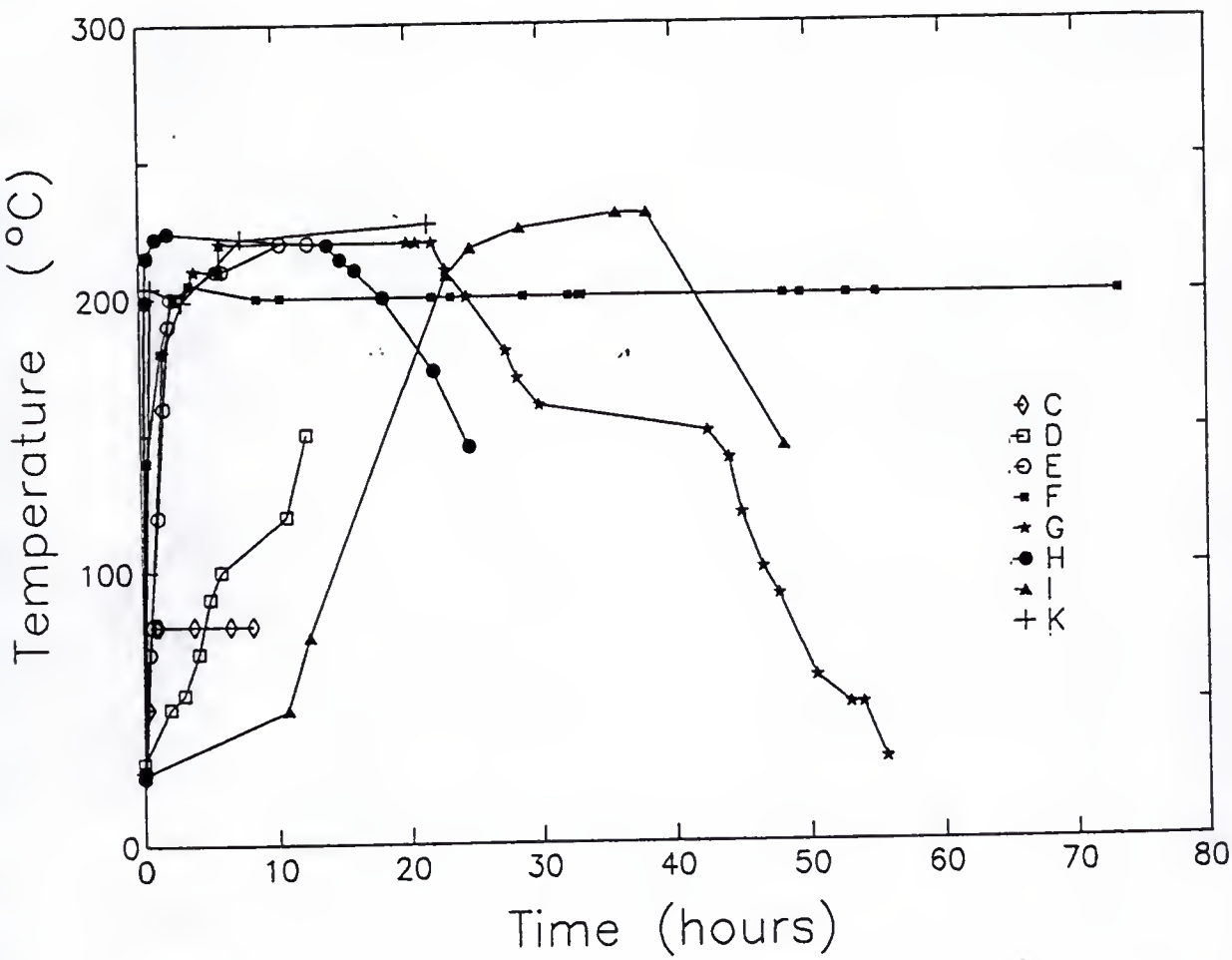

Figure 3.4. Heating curves for vacuum dehydration. The temperature in runs C through G is the reading on the panel of the Thermolyne furnace. The temperature in the other runs is that of a copper-constantan thermocouple inside the Pyrex glass furnace. The heater was turned off at the end of each curve.

Run	T (°C)	Hours	Void (%)	Appearance	Note
A	300	0.25	100	Powder	Thermolyne set to LO
B	50	1.0	0	No change	With Variac
C	80	8.5	0	Powder	With Variac
D	150	0	1	Powder	Slow heating. With Variac
E	210	2	15	Powder	With Variac
F	200	70	1	Powder	With Variac
G	220	18		Powder	Slow cooling. With Variac
H	224	12		Powder	Home-made oven with window
					With ramp circuit
I	230	12	0.6	Powder	Slow heating and cooling
					With ramp circuit
J	319	0		Powder	Power failure
					With ramp circuit
K	227	21		Powder	With ramp circuit

Table 3.1. Summary of vacuum dehydration. A Thermolyne furnace has been used for runs A through G. A homemade furnace has been used for runs H through K. The amount of nitrogen absorbed at 77 K is expressed as a percentage of the full-pore adsorption per unit mass of the sample dehydrated in run A.

the possibility of framework deformation due to dehydration. One possible explanation is the large thermal expansion of water in comparison with that of the framework[1].

Only run G, in which cooling was slow, showed any promise. The crystal in this run became completely white as in all other runs except run B, but was less fragile than the other crystals which either turned into white powder during heating or crumbled during handling with a pair of tweezers. On the other hand, the heating rate of 0.2°C/min used in run D did not prevent pulverization, although the final temperature of 150°C was too low for dehydration. The observation that the pulverization occurs even when dehydration does not take place and that the cooling rate made some difference in the strength of the samples motivated us to study when the pulverization starts and how it progresses.

[1]The coefficient of the linear thermal expansion for chabazite is 2.3×10^{-6} K^{-1} near 300 K [42]. For water, the coefficient is 303×10^{-6} K^{-1} [52].

Time (hours)	Description	Temperature (°C)	Note
0.0	No change	27	Start heating
0.4	No change	199	
0.6	Half of crystal white	215	
1.2	Remaining half has a few cracks	222	
2.1	No change	224	
14.0	No change	220	Start cooldown
15.0	Whole crystal is getting whiter	214	
16.1	Same as above	210	
18.2	Same as above	200	
21.9	Same as above	173	
24.6	Same as above	145	
37.75	Completely white	27	

Table 3.2. Summary of run H. The size of the chabazite crystal was about $1 \times 2 \times 2$ mm^3. The pressure inside the furnace was maintained at less than 4×10^{-5} torr. The temperature was measured by a copper-constantan thermocouple inside the furnace.

In order to observe the crystals during heating, a home-made furnace with a window in the thermal insulation was built as described at the beginning of this section. The heating and cooling rates of the furnace were controlled by the arrangement shown in Fig. 3.5. The ramp circuit controls the combination of a Douglas Randall RDA input module and a R10 proportional controller [53] which regulates the power into the Variac. The setting of the Variac determines the maximum voltage across the 10.3 Ω heater. Figure 3.6 shows the ramp circuit, which is a simple integrator using an operational amplifier. The ramp rate is set by the variable resistor.

Table 3.2 shows the observations made in run H, in which the temperature was raised at a rate of 8°C/min. The crystal showed little change until the furnace reached the

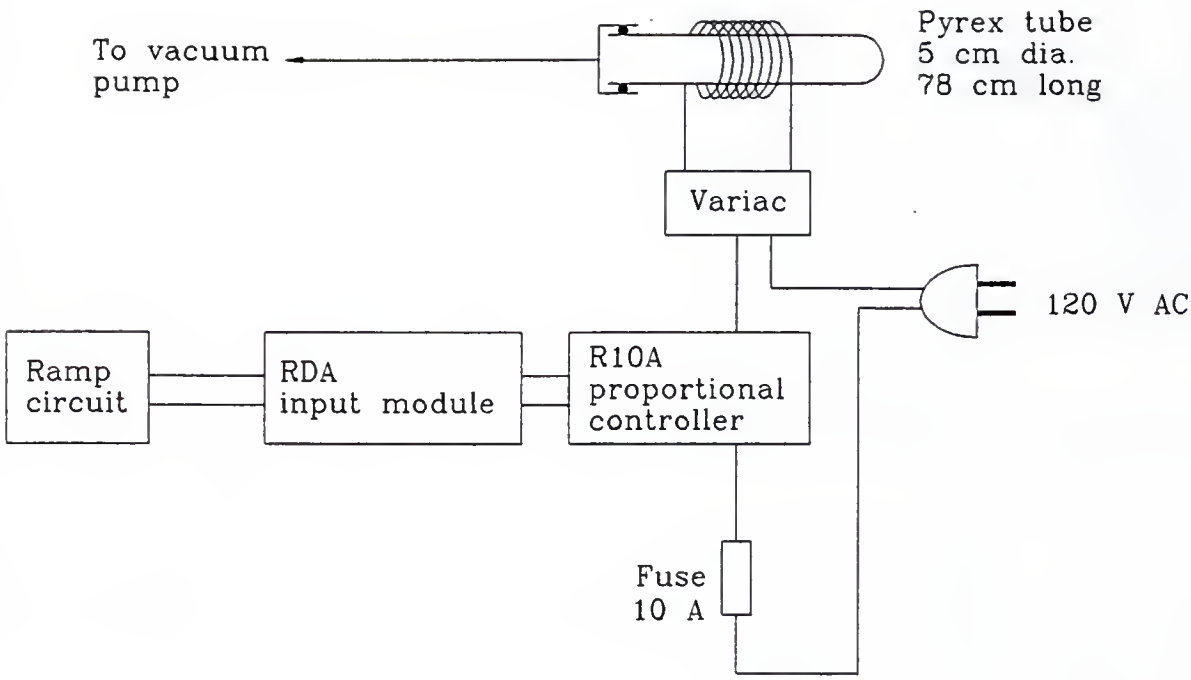

Figure 3.5. Home-made furnace and the power controller. Glass tape and glass wool were wrapped over the heater for thermal insulation. A see-through window was made by cutting a 1 cm × 1 cm hole in the glass insulation.

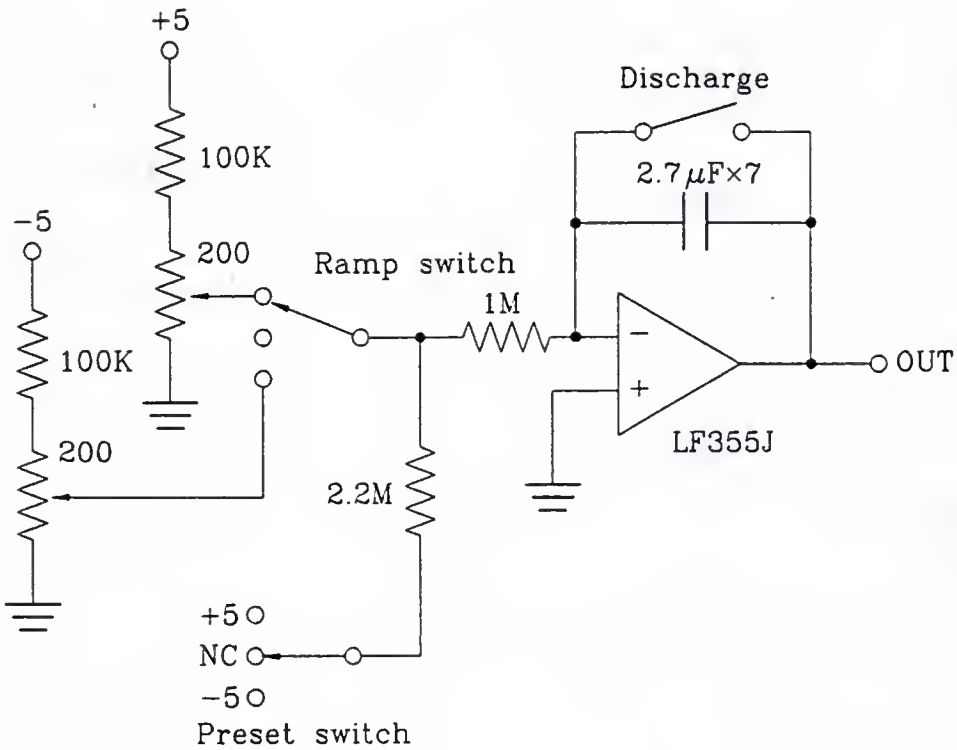

Figure 3.6. Ramp circuit for the furnace-heater controller. Seven 2.7 μF capacitors were used in parallel for the integrator.

final temperature of 224°C but started to turn white 10 minutes later. One half of the crystal became white first, the other half turning white subsequently at a slower rate. This observation suggests that pulverization occurs at different rates depending on individual crystals or on parts of a crystal. Another important observation in this run was that there was little change in the crystal for the first 20 minutes of heating, although the temperature had reached about 200°C by the end of this period. The pulverization occurred primarily after the furnace reached the highest temperature of 224°C and continued to progress while the furnace cooled toward room temperature. In fact, much shorter heating as in run C produced a badly pulverized crystal, implying that the pulverization continues even near room temperature once the crystal has been heated. In run J, power failure terminated the heating immediately after the temperature reached 319°C . Even after the furnace reached room temperature, the pulverization of the chabazite crystal progressed for at least 12 hours.

3.3 High Pressure Dehydration of Chabazite

Dehydration in an MS-17 reactor. In the manufacturing process of aerogel, the solvent needs to be removed from the silica solution. If the gel is heated in vacuum for drying, the silica framework collapses due to the surface tension of water. The common method to avoid this is to heat the silica solution under high pressure so that water vaporizes above the critical point [54], where the surface tension of water vanishes.

To see if this method can be applied to the dehydration of large chabazite crystals, a high pressure furnace was built as shown in Fig. 3.7. The MS-17 high pressure reactor [40], in which the chabazite crystals are placed, is connected through a stainless steel tube with a 1/16 inch o.d. to a dip stick filled with activated charcoal, a nitrogen gas cylinder, and

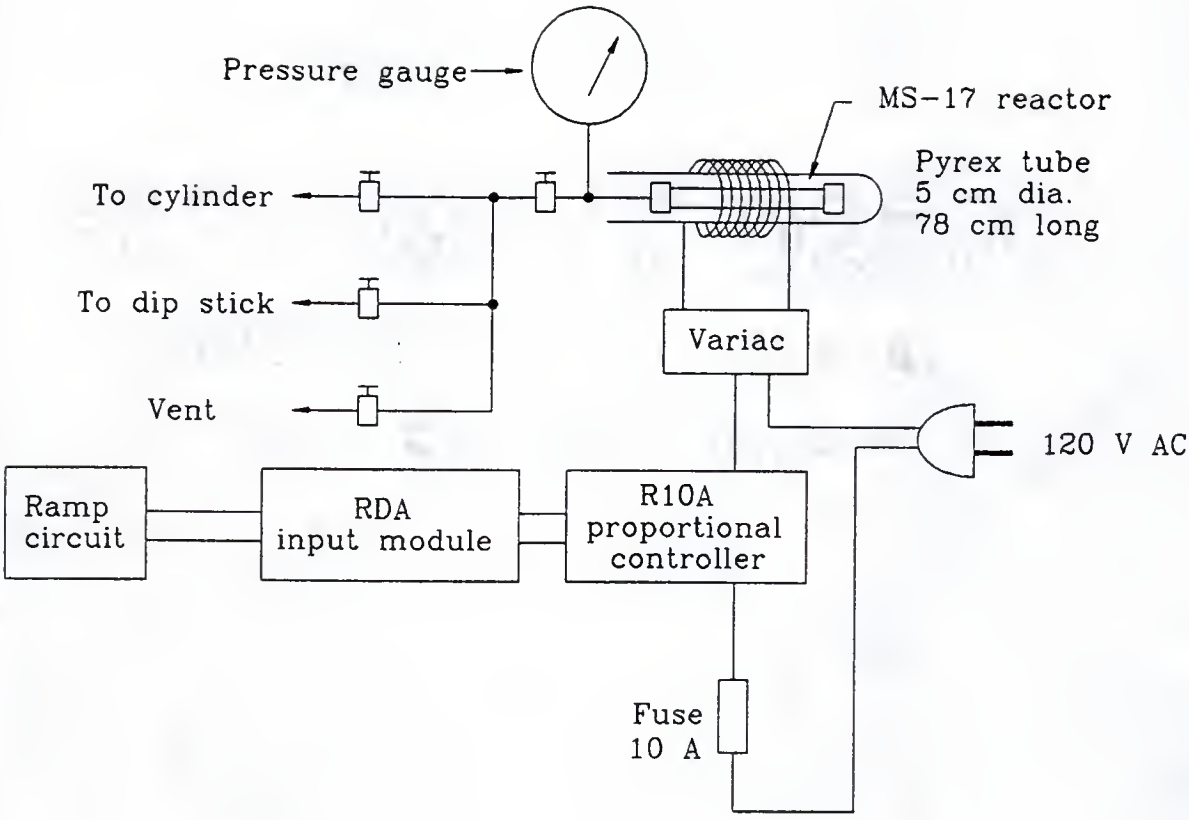

Figure 3.7. High pressure furnace using a MS-17 reactor. The reactor was inserted in the Pyrex glass tube removed from the home-made furnace for vacuum dehydration.

Run	T (°C)	P (psi)	Description	Note
H1	500	6500	Powder	Nitrogen atmosphere
H2	400	7200	White and Intact	Water atmosphere pumped to vacuum
H3	240	7100	Surface clouded otherwise no change	Leak. Heating halted
H4	320	6000	White	Glass cell also white
H5	200	5200	No change	Nitrogen atmosphere
H6	250	900	No change	Nitrogen atmosphere

Table 3.3. Summary of supercritical dehydration. The furnace is a HIP reactor (model MS-17) pressurized by a charcoal-filled dip stick.

a pressure gauge. The entire reactor is inserted into the Pyrex glass tube scavenged from the home-made vacuum furnace, including the heater. Nitrogen gas is introduced from the cylinder at about 2,000 psi to the dip stick immersed in liquid nitrogen. Warming the dip stick back to room temperature raises the gas pressure in the reactor to about 4,000 psi. By repeating the process, a pressure of over 10,000 psi is achieved. The rated pressure of the reactor and the stainless-steel tubing is 15,000 psi. However, the actual working pressure turned out to be less than 10,000 psi because the pressure seals of the reactor are heated in this arrangement.

The ramp circuit and the power control unit were the same as in the vacuum dehydration experiment. Heating of the entire reactor oxidized the threads of the pressure seals. To prevent the oxidation, the threads were coated with Fel-Pro C5-A [55] as recommended by the reactor manufacturer. The oily component of this lubricant burned when heated and left a nasty residue, which needed to be cleaned off the inner surface of the Pyrex tube and the threads of the pressure seals after each run.

A total of six heating runs were made using this furnace: two in nitrogen atmosphere and four in water vapor, as shown in Table 3.3. In run H1, the chabazite crystal was heated

in a 6,500 psi nitrogen atmosphere to 500°C, at which time the furnace was pumped to vacuum. This combination of pressure and temperature was chosen so that the water in chabazite would be in the supercritical region of the phase diagram. This procedure yielded 88% of the void volume of the fully dehydrated sample, but the crystal was damaged as the in heating in vacuum. Obviously, either supercritical dehydration does not work for chabazite or the critical point for the zeolitic water is higher in pressure or in temperature than the parameters we have chosen.

Run H5 was made in a 5,200 psi nitrogen atmosphere with a final temperature of 200°C. Unlike in run H1, the furnace was never pumped. As expected, there was no measurable void volume in the crystal, whereas the appearance of the crystal remained unchanged. This showed that a high pressure atmosphere prevents pulverization of the crystal. Clearly, the water needed to be removed from chabazite selectively by a sorption pump without releasing the pressure in the furnace. Unfortunately, the end cap of the MS-17 reactor accommodated only a 1/16 inch outer-diameter tubing, which added an unacceptably large impedance to the sorption pump. In order to remove this limitation, a new home-made furnace was built as described in the next section.

Runs H2 through H4 were made in water vapor on a hypothesis that high-pressure water vapor in the reactor reduces the internal stress caused by the thermal expansion of water in the chabazite framework by lowering the chemical potential difference of water between the inside and outside of the framework. In run 2, the water vapor in the furnace was released to the atmosphere after the furnace reached 500°C and was then pumped to vacuum. In this run, the sample crystal became completely white but remained in one piece.

In run H3, the heating was halted due to an accidental failure of the pressure seal. The highest temperature in this run was 240°C. The water was not removed from the furnace

Run	T (°C)	P (psi)	Void (%)	Description	Note
H7	245	1290	0		
H8	300	1120	0.1		
H9	320	1340	75.5		Three pressure leaks
H10	320	1200	1.5		
H11	370	1000	34		

Table 3.4. Summary of high pressure dehydration. The furnace was made from a 1/2 inch o.d. stainless steel tube and was directly attached to a sorption pump.

until it cooled to room temperature. The crystal showed little change except for some cloudiness on the surface, suggesting that the pulverization of the chabazite crystal can be avoided even at temperatures high enough to pulverize the zeolite crystal in vacuum.

In run H4, the crystal was heated to 320°C. The only differences from run H2 were a lower ramping rate which required four days for the temperature to reach the final value, as opposed to three days for run H2, and the maximum temperature which was lower by about 80°C. The chabazite crystal and the Pyrex glass cell that held the crystal turned completely white. It appears that water at high temperature and high pressure reacts with chabazite and Pyrex.

Dehydration in the 1/2 inch stainless steel tube furnace. This home-made furnace consisted of a stainless steel tube 1/2 inch in o.d., 0.035 inch in wall thickness, and 16 inch in length with a sorption pump as illustrated in Fig. 3.8. A sorption pump filled with activated charcoal was connected to the furnace via a short length of a 1/4 inch o.d. tubing. When immersed in liquid nitrogen, the pump removes water selectively from the high pressure helium atmosphere. The same dip stick that had been used in the previous furnace was used to pressurize the furnace with helium. Although the pressure rating of the tube

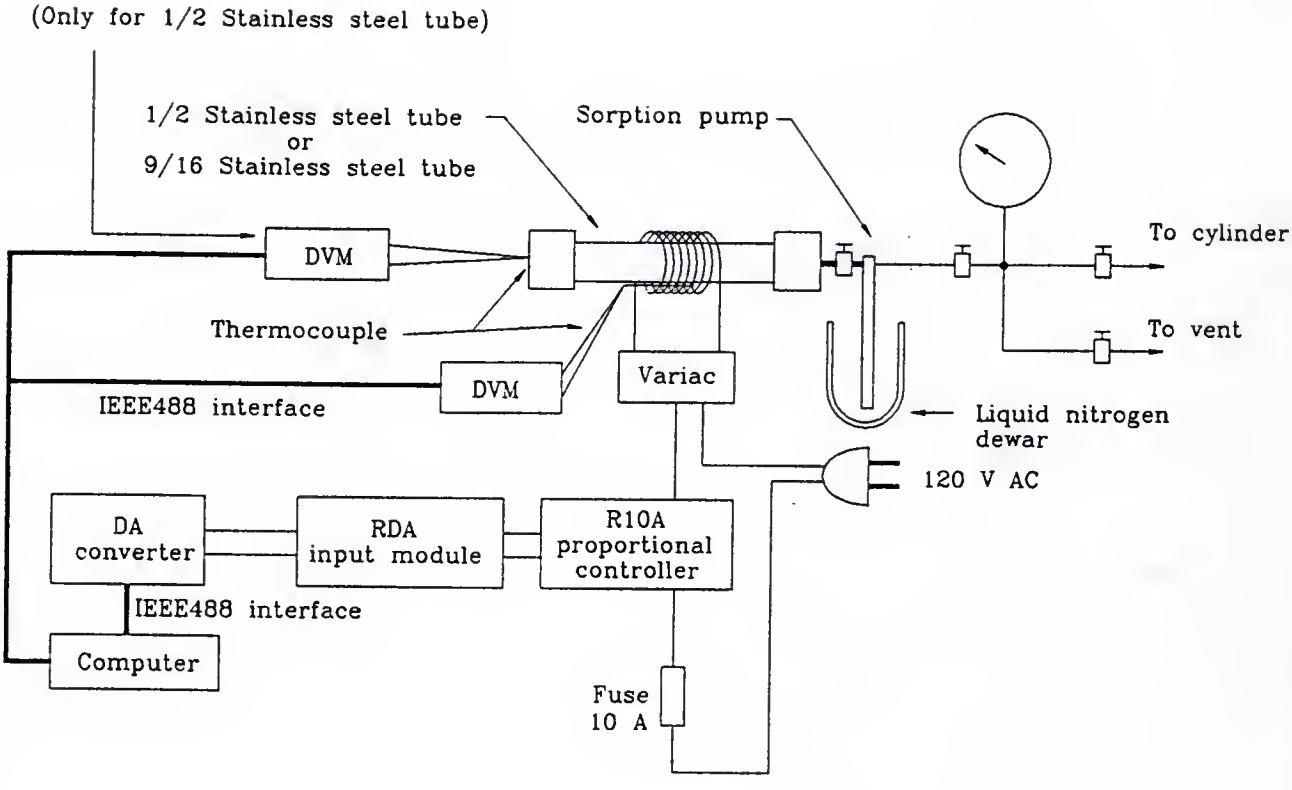

Figure 3.8. High pressure furnace made from a 1/2 inch stainless steel tube. The furnace is connected to a sorption pump filled with activated charcoal for selective removal of water.

was 3,000 psi, the Stycast 2560 feedthrough for the thermocouple wires limited the actual working pressure to less than 1,300 psi.

A total of five runs were made in this furnace as given in Table 3.4. All of them used a helium atmosphere, since only a gas which does not liquefy at 77 K is compatible with the liquid-nitrogen-cooled sorption pump. The helium pressure ranged from 1,000 psi to 1,340 psi, and the maximum temperature ranged from 245°C to 370°C. The crystals were wrapped in a thin sheet of stainless steel to keep them from moving in the furnace. During run H9, the pressure dropped three times nearly all the way to atmospheric pressure, and the sample was found to be completely pulverized. Therefore, the result of this run should be discarded. The pressure failure occurred at the valve located right above the sorption pump, when the nitrogen dewar was topped off. Evidently, the rubber o-ring in the valve froze out and ceased to seal the valve shaft properly when the liquid nitrogen level was too close to the valve.

The results of these runs show clearly that a higher temperature is required to dehydrate chabazite in helium gas at an elevated pressure than is needed in vacuum. (See Table 3.4.) Even at 370°C, a substantial amount of water remained in chabazite after one week. The crystal was not pulverized at least up to this temperature, although it did turn white, suggesting microscopic damage. At 320°C, where only 1.5% of water could be removed in 10 days, the sample remained mostly transparent with little change. The results strongly suggest that a temperature higher than 370°C is required to completely dehydrate chabazite in high-pressure helium gas and that pressures much higher than 1,000 psi may prevent chabazite from turning white.

Dehydration in the 9/16 inch stainless steel tube furnace. Another furnace was made from a 9/16 inch outer-diameter stainless steel tube purchased from HIP with an inner diameter of 3/16 inch and a rated pressure of 60,000 psi, as opposed to 3,000 psi for the 1/2 inch o.d. tubing. The configuration of the furnace was similar to that of the 1/2 inch o.d. furnace. The working pressure was limited to the rated pressure of 15,000 psi for the 1/16 inch o.d. tubing which connected the furnace to the dip stick. No thermocouple was placed inside the furnace to get rid of a feedthrough, which was the weak spot in the 1/2 inch o.d. furnace. 10 ft of a 1.07 Ω/ft heater wire was wound over a glass sleeve which covered the tube. A chromel-alumel thermocouple insulated with a small diameter glass sleeve was placed underneath the larger glass sleeving.

Table 3.5 shows the results of dehydration runs done in this furnace. Runs C1, C2, C4, and C5 yielded no significant void volume. The surfaces of the crystals became lusterless and white after the heating. The sample of run C5 was reheated in vacuum in order to remove all remaining water. However, very little increase in the void volume was observed in the nitrogen adsorption isotherm at 77 K, suggesting that the crystal had permanently lost the pores. The result is surprising, since chabazite heated up to 800°C in air can be rehydrated at room temperature [43]. However, Aoki [56] has reported that chabazite in the presence of water under a pressure up to 1 kbar transforms into other types of zeolite such as wairakite and gonnardite around 250°C depending on the heating conditions. In high pressure helium gas whose density is not much lower than that of liquid helium, zeolitic water which dissociates from the chabazite framework cannot move out of the crystal as quickly as in vacuum heating. It is possible that prolonged contact with zeolitic water under high pressure caused some transformation of chabazite into a structure with smaller pores or without pores.

Run	T (°C)	P (psi)	Time (hours)	Void (%)	Note
C1	600	8200	144	2.7	pressure failure
C2	580	9600	167	3.5	White. Shiny
C3	640	14000	133	49	Heating with a step
C4	600	15100	155	0	White. Fragile
C5	740	15700	150	0.2	Three steps
C6	660	12800	65	33	Pressure failure
C7	390	12800	brief	8	Three steps
C8	650	15600	120	20	Three steps
C9	560	12000	48	39	Active temperature control
					One step here after
C10	400	12800	60	75	
C11	320	12700	60	64	
C12	360	13000	60	73	
C13	320	13000	100	7	
C14	400	13800	60	54	
C15	360	13800	60	57	
C16	370	13600	100	85	Sample for Torsional
					pendulum experiment
C17	370	13600	100	15	Heater rewound
C18	380	13850	100	54	
C19	390	13800	100	68	
C20	390	12450	100	70	
C21	390	12450	100	77	
C22	390	13800	100	75	

Table 3.5. Summary of high-pressure dehydration of chabazite in the 9/16 inch diameter stainless steel furnace.

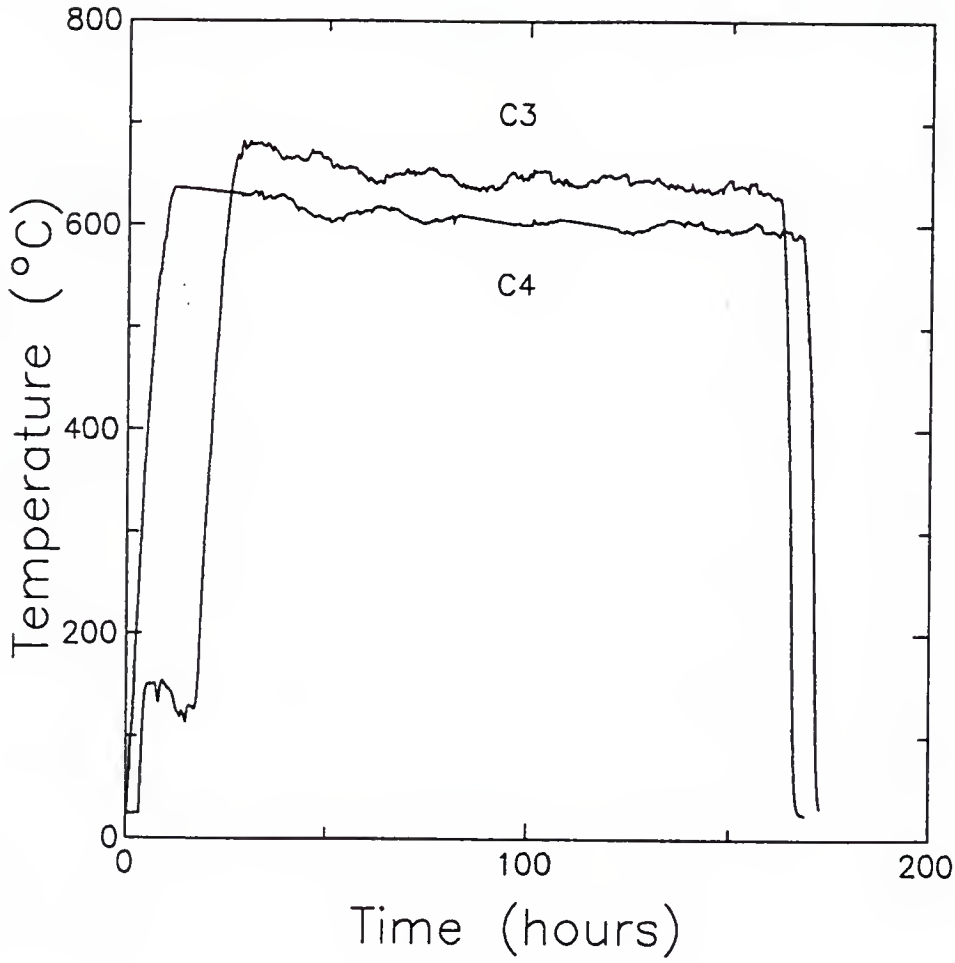

Figure 3.9. Heating curves for chabazite dehydration runs C3 and C4.

Run C3 yielded a significant void volume of 49% in contrast to runs C1, C2, C4, and C5. The only important difference between run C3 and the other four runs is the heating rate. Fig. 3.9 shows the heating curve for C3 and C4. In run C3, the temperature was raised continuously from room temperature to the final value, whereas run C4 employed an intermediate step in which the temperature was kept at 140°C for 12 hours. It is not clear whether this step enhances the dehydration by lowering the average rate of temperature change or it is necessary to have a period of constant temperature before reaching the final temperature. In order to explore further, heating with three steps was tried in runs C6, C8, and C9, which yielded significant void volumes, although they were not as large as obtained in run C3. Surprisingly, post-baking of samples of runs C6 and C9 produced either no change or only a small increase in the void volume, revealing that the up to 67% of the pores had been permanently lost. The loss was clearly less for the crystal dehydrated at the lower temperature of 560°C, indicating that an even lower final temperature needed to be used. Heating with one step had produced a larger void volume than those with three steps.

Lower final temperatures of 320°C through 400°C and one step during the ramp-up of temperature were used in all runs after C9. All of them except runs C13 and C19 yielded larger void volumes than any previous runs, with the void volumes showing no clear correlation with the final temperature. The results of the post-baking showed that the permanent loss of pore volume can be minimized, in the best case only 8% of the total pore volume as in run C12. The optimum temperature appears to be around 360°C. Run C16 at this temperature yielded 85% of the total void volume, which is the highest of all the runs.

After run C16, the heater wire on the furnace was rewound. This evidently caused the actual temperature of the furnace to be somewhat lower than before for a given thermocouple reading. Run C17 indicates the result of dehydration after the rewinding at the same nominal temperature as in C16. This result shows that the temperature was up to 30°C lower around 360°C. The optimum final temperature after rewinding the heater was found to be 390°C.

The final runs are C18 and C19, in each of which a large crystal roughly 5 mm in size were heated together with several small crystals ranging from 1 to 2 mm in size. For each run, the nitrogen adsorption isotherms were measured separately for the large crystal and the small crystals, yielding about a 10% larger void volume for the large crystal. Postbaking of the small crystals revealed that 6 - 12% of water remained in the pores after the high-pressure dehydration and 20 - 25% of the pore volume had been permanently lost. The high-pressure dehydration either works less effectively for small crystals or causes larger loss of pores in small crystals. At the present, it is unclear what causes this difference. At any rate, the two large crystals prepared in these runs were considered satisfactory for the torsional-pendulum experiments described in Chapter 4 and Appendix B, since the 75 - 77% for the fraction of open pores were certainly above the percolation limit. We leave it up to material scientists and engineering chemists to perfect the technique of high-pressure dehydration developed in this dissertation work.

CHAPTER 4
TORSION PENDULUM EXPERIMENT ON ^{4}HE ADSORBED IN CHABAZITE

4.1 Sample Cell

A schematic representation of the torsion pendulum containing a dehydrated chabazite crystal is given in Fig. 4.1. The crystal used in the experiment described in this chapter was C22, whose preparation has been described in the previous chapter. Another pendulum was constructed with crystal C16 prior to this experiment. However, it was realized at the end of the experiment that the crystal adsorbed essentially no ^{4}He introduced to the sample cell. That experiment is discussed in Appendix B together with a control experiment using a pendulum containing no chabazite crystal.

The crystal was $5 \times 5 \times 5$ mm^3 in size and weighed 87.6 mg before dehydration. The void volume of the crystal after dehydration was estimated to correspond to 0.467 mmol of nitrogen according to the nitrogen isotherm of smaller crystals dehydrated in the same batch. The void volume of the sample crystals was not measured, since nitrogen-adsorption isotherm measurement sometimes damages the crystal according to our experience. The void volume corresponds to 77% of that of a fully dehydrated crystal. The estimated amount of ^{4}He that completely fill the pores is 0.75 mmol, based on the ratio of about 2.7 between the volumes of a nitrogen molecule and a helium atom.

The crystal was glued in place with Stycast 2850FT in a dry nitrogen atmosphere. The moment of inertia of the pendulum was calculated to be $I = 2.77 \times 10^{-2}$ g-cm^2 including

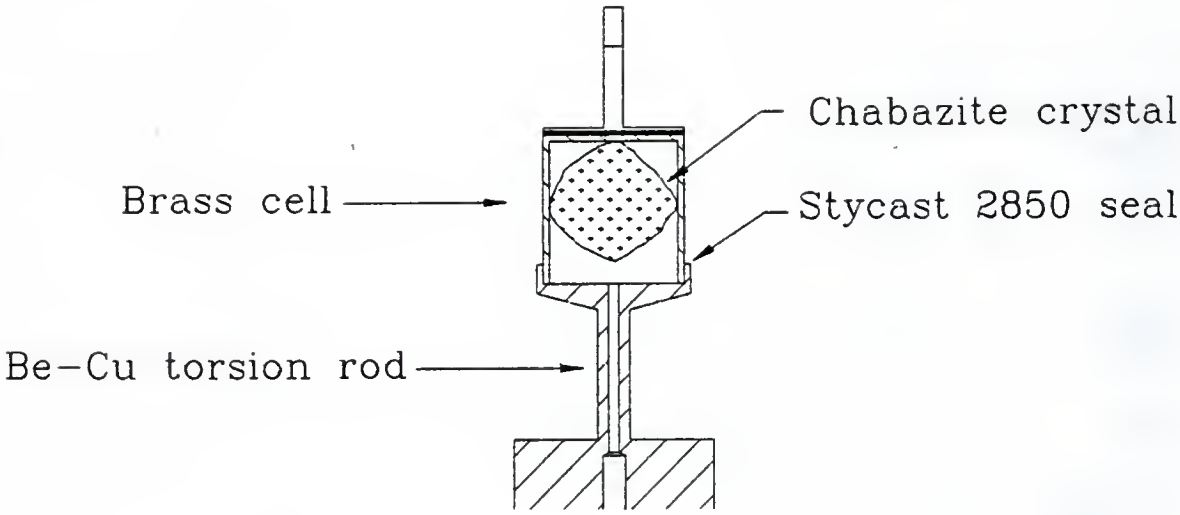

Figure 4.1. Torsion pendulum containing a dehydrated chabazite crystal.

the chabazite crystal. The quality factor Q was about 530,000 at 1 K as can be seen from the resonance curve shown in Fig. 4.2.

4.2 Results and Analysis

Figures 4.3 and 4.4 show the resonance frequency and the amplitude of the torsion pendulum for several amounts of ^{4}He adsorbed in the chabazite crystal. There is no obvious feature within the frequency curves indicating that a superfluid transition was detected within the resolution of the experiment. The smooth increase in frequency with temperature observed for amounts of ^{4}He corresponding to 80% or more of the full pore volume was due to evaporation of ^{4}He from the chabazite. The null result of the experiment places an upper limit for the possible superfluid density. The loading sensitivity of the pendulum depended slightly on the amount of ^{4}He, but the highest value was -0.25 mmol/Hz as seen from Fig. 4.5, which shows the resonance frequency as a function of the amount of ^{4}He at 150 mK, near the lowest temperature of the experiment. The standard deviation of the frequency was typically 3.3×10^{-5} Hz at a fixed temperature. Therefore, the smallest amount of superfluid component that can be detected in our experiment was 8.2 nmol, corresponding to 7.8 ppm of adsorbed ^{4}He at full pore. Within this resolution, we have observed no superfluidity in ^{4}He adsorbed in chabazite.

4.3 Conclusions

We can hypothesize as to why we have not observed superfluidity. One obvious but uninteresting possibility is that the pore size of the chabazite is too small for ^{4}He to become superfluid. In other substrates such as porous Vycor glass, the first 1.3 to 1.5 atomic layers of ^{4}He do not show superfluidity [7]. The chabazite cavity is merely 9 Å in the cross-sectional direction. In such a small space, only a few ^{4}He atoms can be

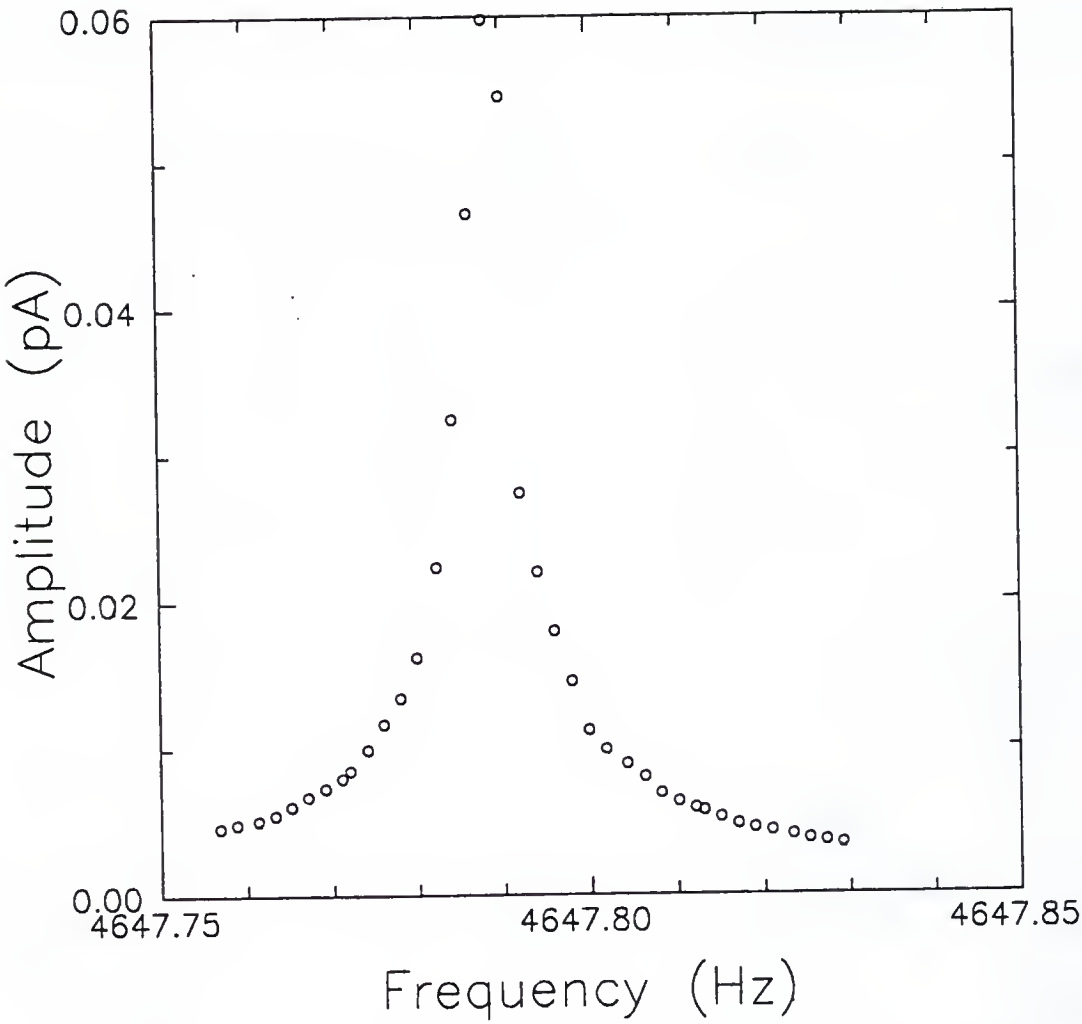

Figure 4.2. Resonance curve of the torsional pendulum containing a chabazite crystal, taken near 1 K before introducing ^{4}He into the cell. The Q factor is 530,000.

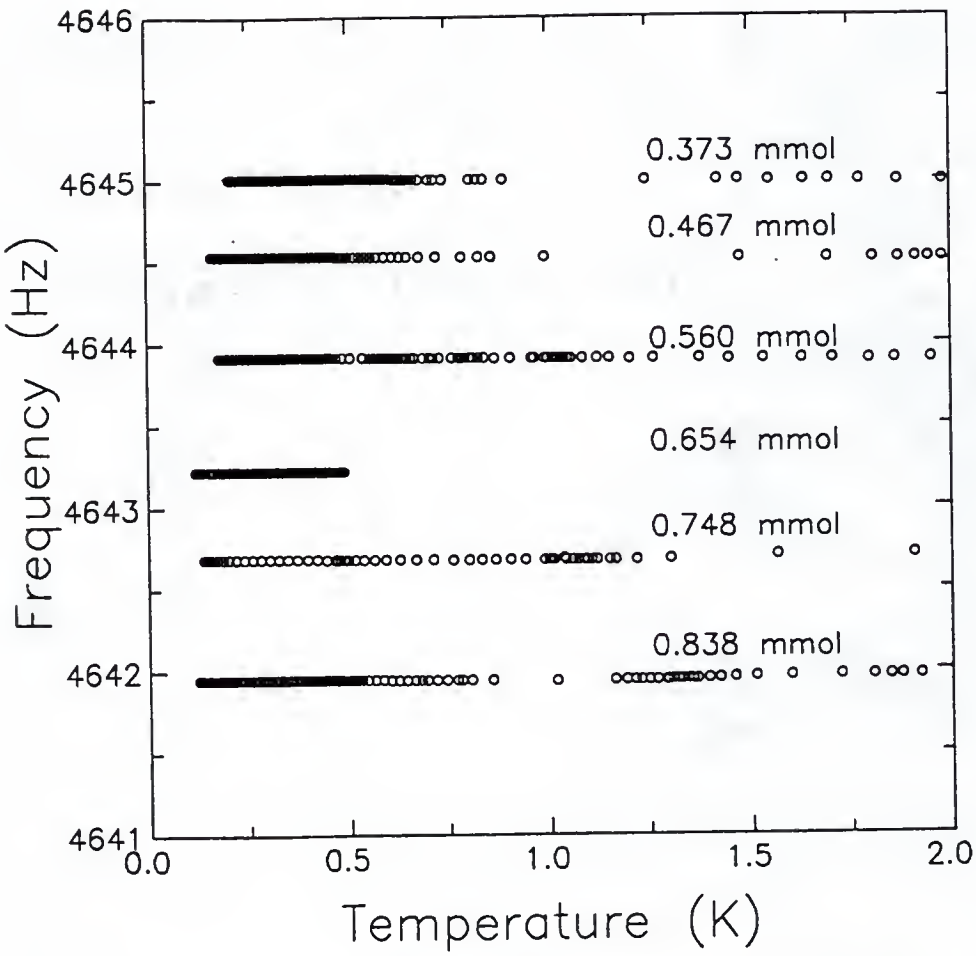

Figure 4.3. Resonance frequency of the torsional pendulum as a function of temperature for various amounts of ^{4}He absorbed in chabazite.

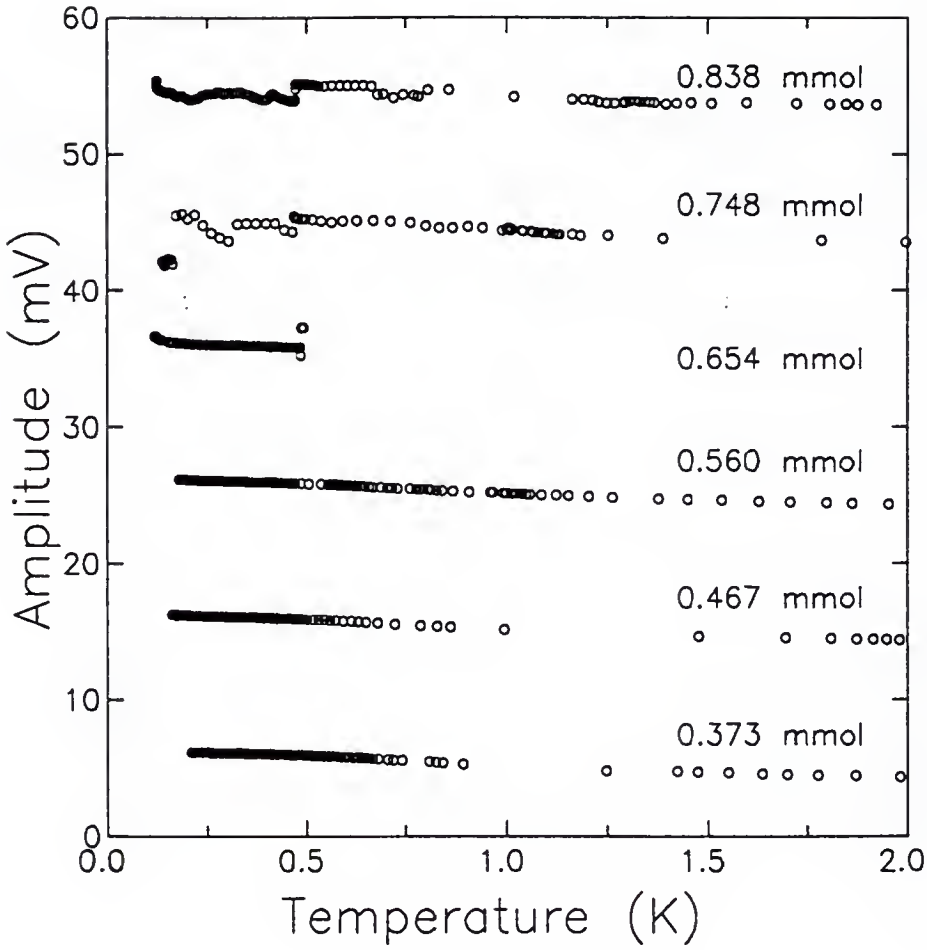

Figure 4.4. Amplitude of the torsional pendulum as a function of temperature for various amounts of ^{4}He absorbed in chabazite.

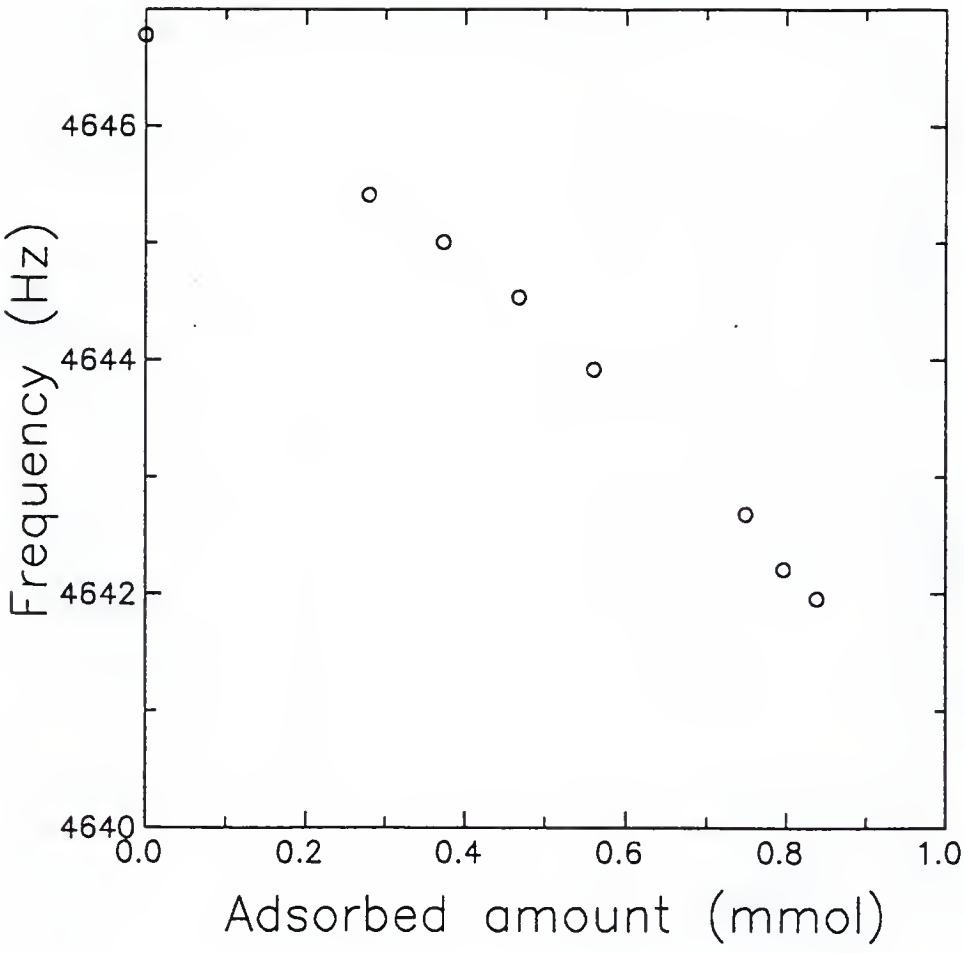

Figure 4.5. ^{4}He-loading sensitivity of the torsional pendulum containing chabazite crystal C22 at 150 mK.

accommodated on top of the first layer. If the ^{4}He film in chabazite has a localized layer as thick as in porous Vycor glass, this layer alone will fill up the pores, leaving no room for a superfluid layer. The objective of this experiment was to see if ^{4}He under such an extreme confinement can still become a superfluid due to the periodic surface potential of the chabazite pores. This evidently does not occur in chabazite. However, chabazite being a natural mineral, it is possible that the sample crystal contained a large number of lattice defects which blocked the superflow. It is also possible that the cations in the chabazite cavities are located at random sites and destroy the periodicity of the surface potential. For these reasons, it would be interesting to revisit ^{4}He in zeolite in the future when an ingenious chemist succeeds in growing a large synthetic crystal of zeolite either containing no aluminum, hence, no cation, or with cations located only inside the lattice framework.

Another possibility is that the crystal contained microscopic cracks, although the crystal remained macroscopically intact after dehydration. A sufficient number of cracks which block the flow paths of superfluid can reduce the fraction of superfluid component that decouples from the torsional pendulum.

CHAPTER 5
TORSIONAL PENDULUM EXPERIMENT ON ^{4}He ADSORBED IN 25 Å DIAMETER PORES OF SILICA

This chapter describes the torsion pendulum experiment on ^{4}He adsorbed in porous silica whose nominal pore diameter is 25 Å. The pore size is the smallest in which the superfluid transition of ^{4}He has been studied to date. Prior to this study, the superfluid transition has been observed in the full pore case of a custom-made Vycor glass of similar pore size, but little other than the transition temperature of $T_c = 0.8$ K can be extracted from the data [57].

5.1 Sample Cells

The porous silica was obtained from Geltech [58] and was cylindrical, 0.388 inch in diameter and 0.200 inch in height, weighing 0.42 g. According to the manufacturer, the specific void volume is 0.4 cm^3/g, which is equal to 43% porosity on the basis of the density of silica, 2.15 g/cm^3 [59].

Modeling the pores to be uniform cylinders 25 Å in diameter leads to an estimate for the surface area of 260 m^2. Only four atomic layers of ^{4}He can be adsorbed on the surface because of the smallness of the pore diameter. The ^{4}He capacities of the first layer and the second layer are taken to be 4.30 mmol and 2.18 mmol, respectively, from the densities of ^{4}He in porous Vycor glass given by Brewer *et al.* [60]: 18.3 μmol/m^2 for the first layer and 13.8 μmol/m^2 for the second layer. The densities of the higher layers are assumed to be that of bulk liquid ^{4}He, 36.3 mmol/cm^3 [60]. These estimates lead to 7.73 mmol for the amount of ^{4}He needed to completely fill the pores.

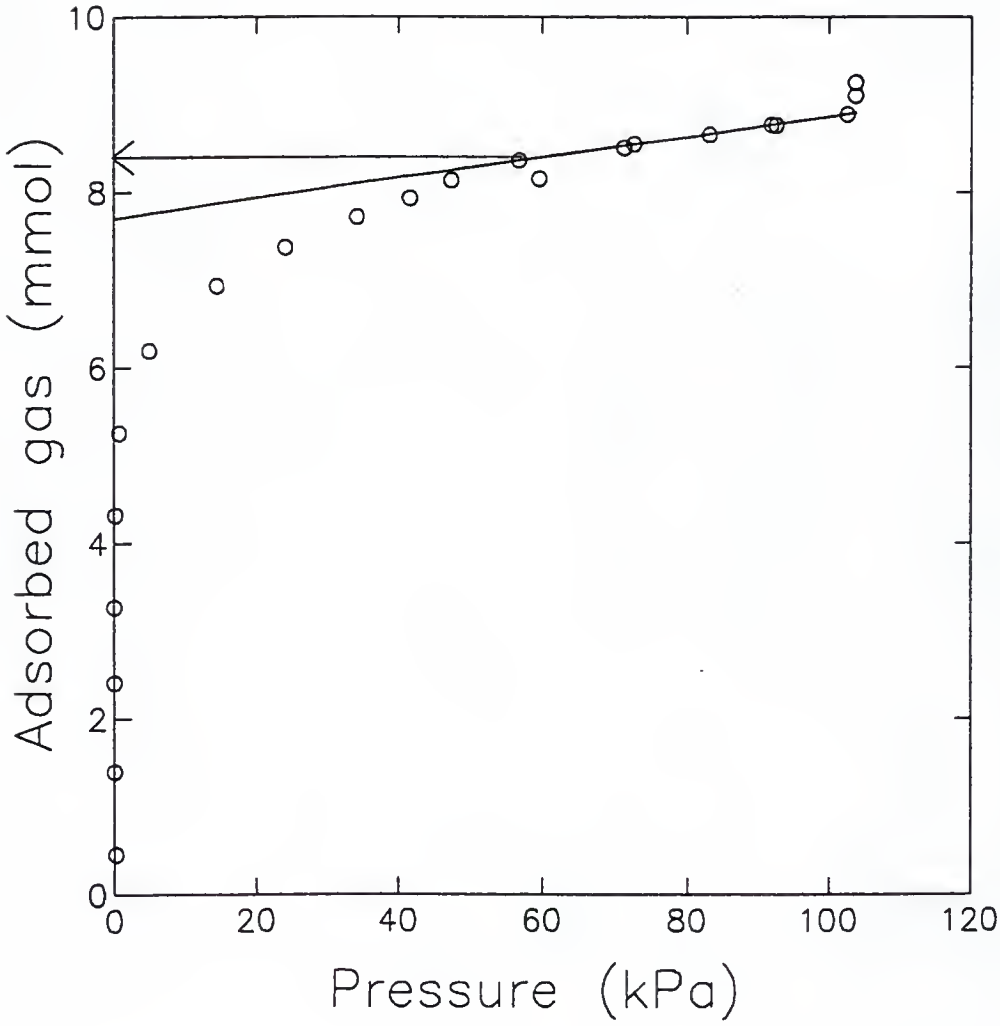

Figure 5.1. Adsorption isotherm of ^{4}He at 4.2 K.

Figure 5.1 shows the result of the adsorption isotherm of ^{4}He at 4.2 K, obtained *in situ* after the torsion pendulum experiment was completed. The curve agrees with neither the Langmuir formula [51] nor the BET formula [61]. The B-point method, an empirical procedure to determine surface area, yields about 8.3 mmol, which is the full pore value instead of the monolayer coverage because of the extremely small pore diameter. The measured value agrees to within 7% of the estimated value of 7.73 mmol. The curves for increasing the pressure and decreasing the pressure showed no difference, indicating that there is no capillary condensation. This is quite as expected for small pores such as ours.

A schematic of the torsion pendulum is given in Fig. 5.2. The torsion rod was dimensionally identical to the one used in the chabazite experiments discussed in Chapter 4 and Appendix B. The estimated moment of inertia of the pendulum was 0.193 g-cm^2. The contribution of the 8.3 mmol of ^{4}He to the moment of inertia was estimated to be about 2.0%. The porous silica was glued in the brass cell of the pendulum with Stycast 1266. In order to prevent the Stycast from migrating into the pores of the silica, a thin film of tacky Stycast was first applied on the faces that make contact to the cell. This step was repeated once, before the silica was glued into the cell with freshly mixed Stycast. The entire procedure was done in a glove bag filled with dry nitrogen to keep the silica from absorbing moisture.

5.2 Results and Discussions

Figure 5.3 shows the frequency of the torsion pendulum as a function of temperature for various amounts of adsorbed ^{4}He. Figure 5.4 shows the amplitude of the oscillation, with the curve for each successive coverage shifted up by 10 pA. The smallest amount of ^{4}He for

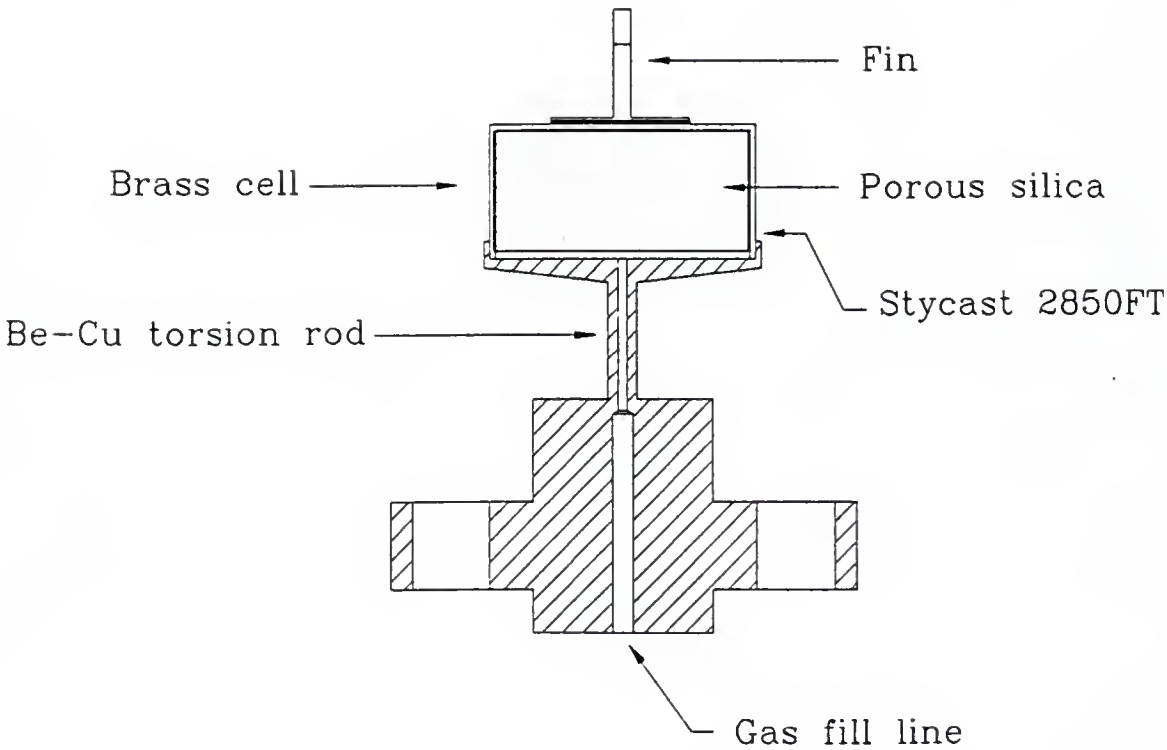

Figure 5.2. Torsion pendulum for the porous silica experiment.

Coverage (mmol)	f_0 (Hz)	T_c (K)	ζ	range (K)
6.75	0.685 ± 0.01	0.121 ± 0.0004	1.08 ± 0.02	$T < 0.113$
6.76	0.785 ± 0.22	0.124 ± 0.004	1.13 ± 0.3	$T < 0.113$
6.80	0.858 ± 0.037	0.142 ± 0.001	1.26 ± 0.05	$0.105 < T < 0.13$
7.00	1.00 ± 0.003	0.226 ± 0.001	1.03 ± 0.07	$0.16 < T < 0.22$
7.21	1.65 ± 0.1	0.344 ± 0.002	1.04 ± 0.05	$0.24 < T < 0.32$
7.40	1.96 ± 0.25	0.457 ± 0.004	1.03 ± 0.1	$0.38 < T < 0.43$
7.60	1.68 ± 0.09	0.582 ± 0.006	1.01 ± 0.06	$0.40 < T < 0.54$
7.80	1.77 ± 0.08	0.681 ± 0.003	1.06 ± 0.04	$0.54 < T < 0.64$
8.01	1.48 ± 0.05	0.78 ± 0.01	1.07 ± 0.06	$0.45 < T < 0.65$
8.20	1.39 ± 0.06	0.82 ± 0.02	1.07 ± 0.08	$0.51 < T < 0.69$

Table 5.1. Results of nonlinear least-squares fitting.

which the superfluid transition was observed is 6.75 mmol, with a transition temperature $T_c = 121$ mK.

In Andronikashvili's experiment in bulk ^{4}He, the entire superfluid component decouples from the motion of the torsion pendulum. When ^{4}He is in a porous media, however, superflow has to take tortuous paths because of the geometry of the substrate, leaving a fraction χ of the superfluid component coupled to the torsion pendulum. In the case of silica aerogel, a highly open substrate, χ factors between 0.16 and 0.33 have been reported for the full pore case depending on the substrate porosity [62], whereas χ in Vycor glass, whose pores provide complex paths for the superflow, is about 0.67. Shapiro and Rudnick [63] have shown that χ in packed powders increases as the porosity decreases.

Figure 5.5 shows the fraction 1-χ of the superfluid density which decouples from the torsion pendulum in our experiment. Even the largest value of $1 - \chi$ is only 0.064, which is about 1/5 of the Vycor case, indicating either extremely tortuous paths for the superflow or a sizeable fraction of completely blocked pores.

In bulk and porous substrates as the temperature approaches T_c, the superfluid density approaches zero and the coherence length diverges. In the critical region, these quantities

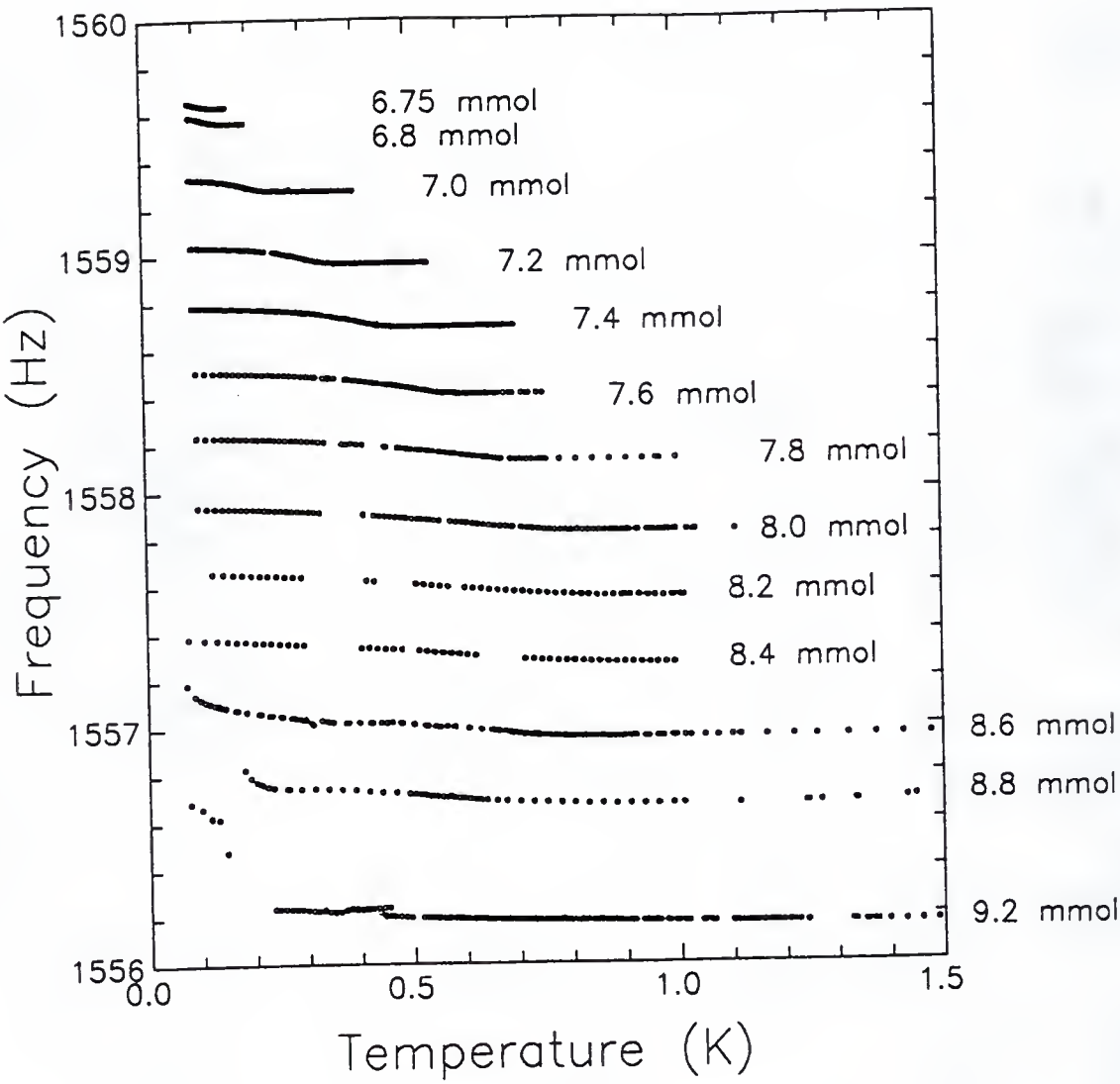

Figure 5.3. Frequency of the torsion pendulum containing porous silica for various amounts of adsorbed ^{4}He.

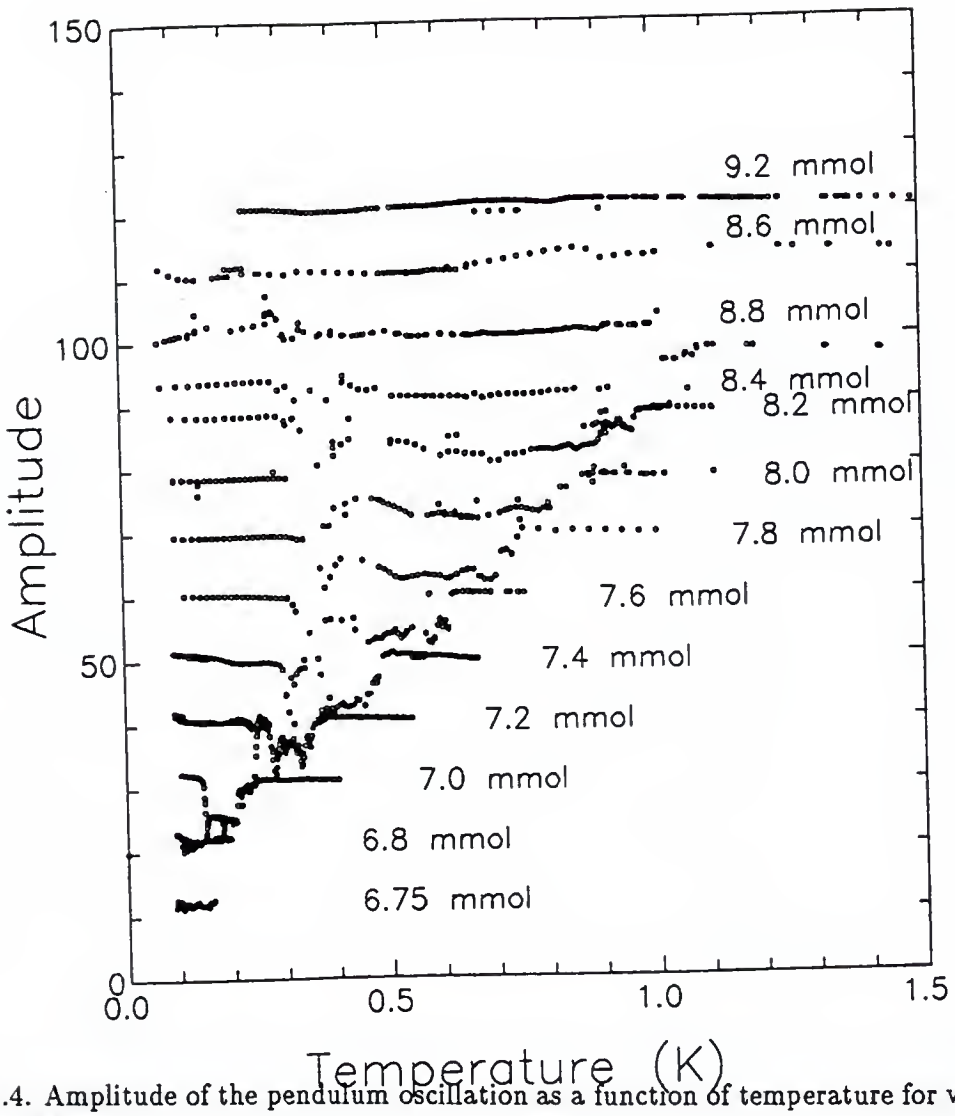

Figure 5.4. Amplitude of the pendulum oscillation as a function of temperature for various amounts of ^{4}He.

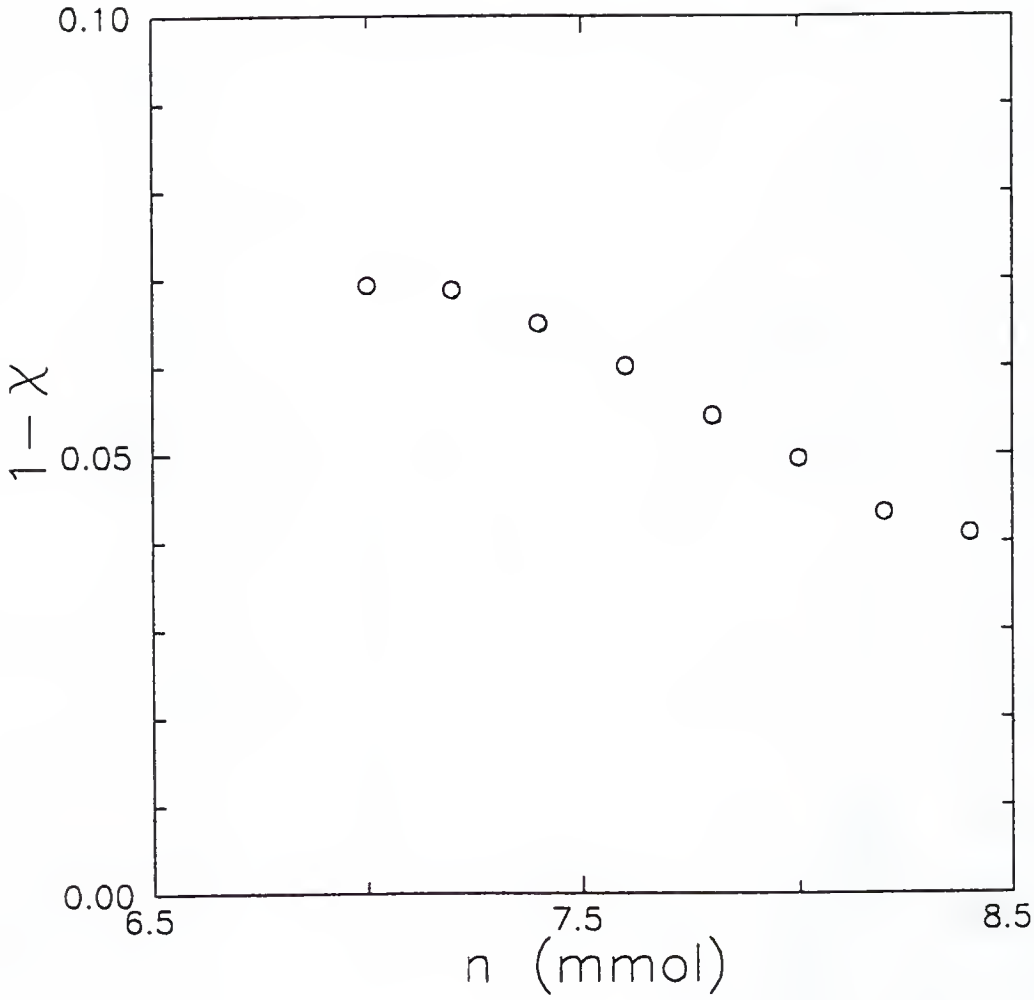

Figure 5.5. 1-χ for various amounts of adsorbed ^{4}He.

follow the power laws [62]

$$\rho_s = \rho_0 \left(1 - \frac{T}{T_c}\right)^{\zeta} \tag{5.1}$$

and

$$\xi = \xi_0 \left(1 - \frac{T}{T_c}\right)^{-\zeta}, \tag{5.2}$$

where ρ_s is the superfluid density and ξ is the coherence length. The superfluid density ρ_s and ξ are connected by the Josephson relation [64]

$$\xi = \left(\frac{k_B T m^2}{\hbar^2}\right) \frac{1}{\rho_s}. \tag{5.3}$$

The results of the nonlinear least-squares fitting of the superfluid density to the power law are compiled in Table 5.1.

The fits are shown in Figs. 5.6 and 5.7. The critical exponents are close to 1.0 for all coverage below 8.20 mmol except 6.80 mmol, for which $\zeta = 1.26 \pm 0.05$. The values are close to the critical exponent obtained for aerogel in the full pore case, ranging from 0.8 to 0.95 depending on the substrate porosity [62, 65, 66], rather than the 0.667 seen in porous Vycor glass.

The transition temperature T_c obtained from the fit increases with the amount of ^{4}He up to 8.20 mmol as shown in Fig. 5.8. The rate of T_c increase is 54.5 ± 0.01 mK/(μmol/m^2), which is about 50% smaller than in the Vycor case [7]. The critical coverage at which T_c becomes zero is 6.56 ± 0.01 mmol according to the fit. This corresponds to 2.0 atomic layers of localized ^{4}He, which should be compared with 1.35 layers for porous Vycor glass [7, 15]. The difference between the two critical coverages is possibly artificial, since the fractional filling of the second atomic layer strongly depends on the definition of the surface area.

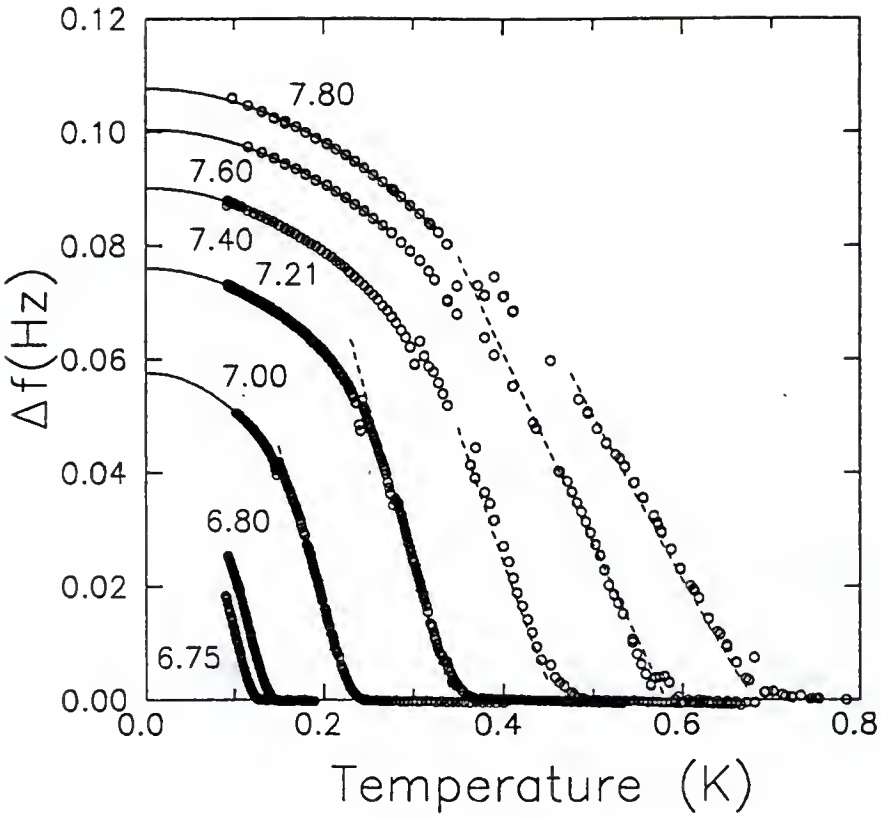

Figure 5.6. Frequency shift Δf of the torsional pendulum due to decoupling of the superfluid density. The solid lines are the T^2 fits in the low temperature region. The broken lines represent the power-law fits in the critical region. The number indicate ^{4}He coverages in mmol.

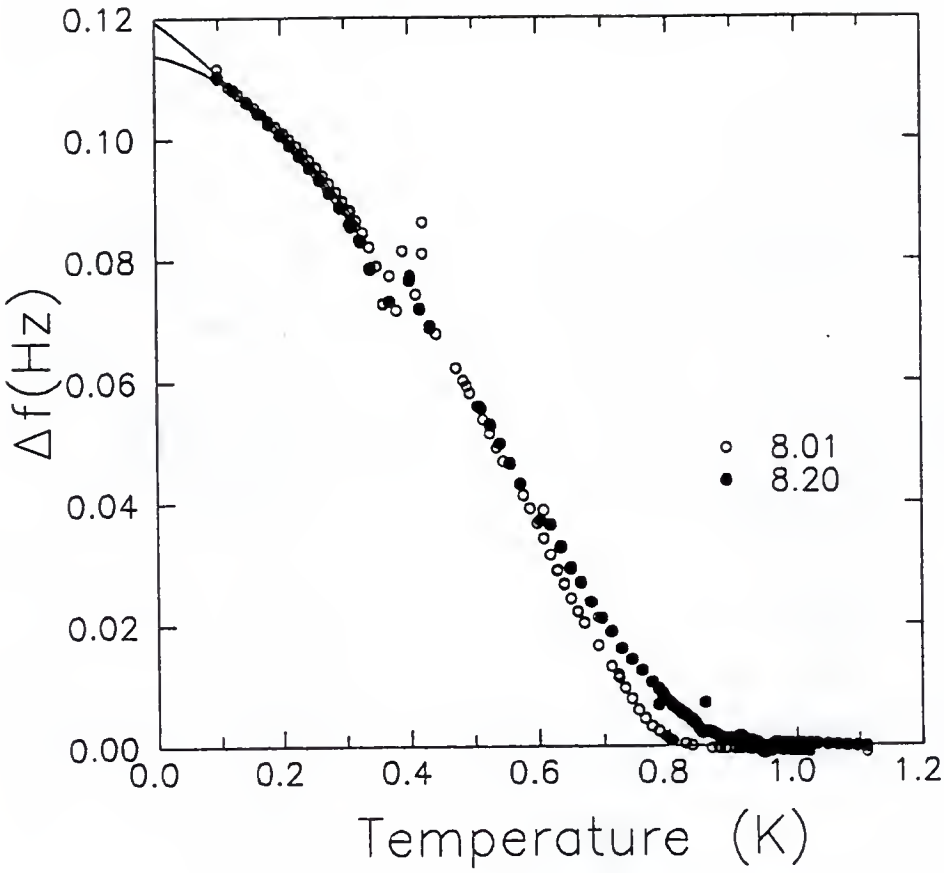

Figure 5.7. Frequency shift Δf for 8.01 and 8.20 mmol.

Coverage (mmol)	T_c (K)	ξ_0 (Å)	ζ	T_{min} (K)	T_{max} (K)	ξ_{min} (Å)	ξ_{max} (Å)
6.8	0.138	7.162	1.028	0.105	0.130	31.174	133.799
7.0	0.226	9.198	0.941	0.160	0.220	29.290	279.685
7.2	0.344	8.098	1.040	0.240	0.320	28.099	129.116
7.4	0.457	8.440	1.033	0.300	0.430	25.449	156.833
7.6	0.582	11.229	1.008	0.400	0.540	36.244	158.909
7.8	0.681	11.201	1.059	0.540	0.640	59.366	219.595
8.0	0.780	14.309	1.066	0.450	0.650	35.797	96.631
8.2	0.822	15.464	1.070	0.510	0.690	43.600	109.451

Table 5.2. Coherence length ξ obtained from the superfluid density ρ_s near the transition temperature. ξ_0 is the coefficient of Eq. 5.2, T_{min} and T_{max} indicate the temperature regions of the fits, and ξ_{min} and ξ_{max} the coherence lengths at these temperatures

.

Here I have used 158 m^2 for the second layer, taking into account the reduction of the pore diameter by the first layer. The critical coverage will be 1.5 atomic layer, if I use 235 m^2 for the second layer as well as for the first layer. For coverages larger than 8.20 mmol, the frequency curve shows a broad rounding, which makes the determination of T_c less precise than for lower coverages. However, T_c appears to be coverage independent in this regime as expected from the vapor pressure isotherm, which indicates that the full-pore coverage is about 8.3 mmol.

The coherence lengths obtained from the Josephson relation are shown in Table 5.2. The critical exponent is close to unity, indicating that the coherence length diverges at T_c roughly as the inverse of $1 - T/T_c$. At the lower temperature end of the critical region, the coherence lengths ranges from 23 to 31 Å depending on the coverage. These values are roughly two to three times the diameter of the pore left open by roughly 2 atomic layers of localized ^{4}He, consistent with the three-dimensional power-law behavior observed. The critical exponent close to unity suggests that the observed superfluid transition belongs to a different universality class from those in porous Vycor glass [67] and packed powder [68] with critical exponents close to 2/3.

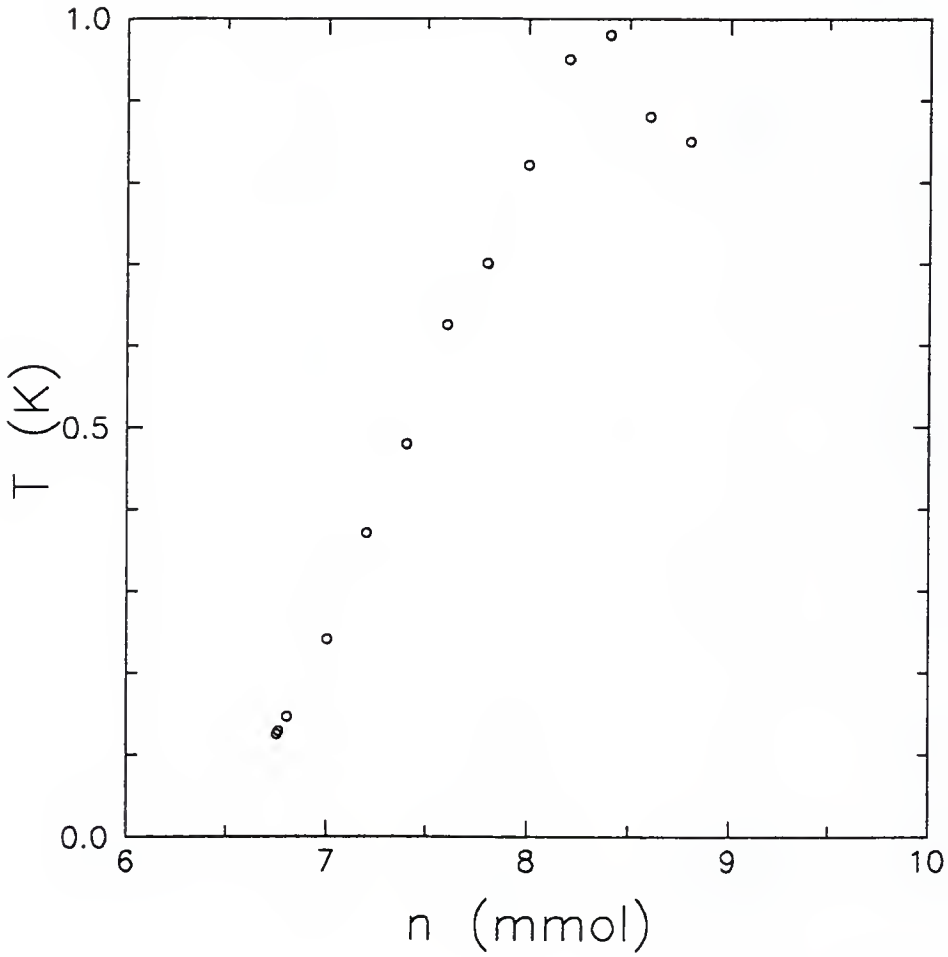

Figure 5.8. Transition temperature obtained by the nonlinear least-squares fitting.

Low temperature fits. In bulk ^{4}He and in ^{4}He adsorbed in porous Vycor glass, the normal fluid density ρ_n at temperatures below 0.5 K arises only from the excitation of phonons. Padmore [69] has argued that ρ_n in this regime depends on temperature as T^{D+1}, where D is the dimensionality of the system. Vycor glass data [7] show a T^2 dependence consistent with a cylindrical (one dimensional) geometry. In our results, the frequency curves for ^{4}He coverages from 7.00 mmol to 7.80 mmol follow T^2 temperature dependences below about 44% of T_c. For 8.01 mmol and higher coverages, the frequency curves are fitted better with $\alpha T^2 + \beta T$ (where α and β are fitting parameters) than with a T^2 term alone. As shown in Fig. 5.9, the T^2 term gradually becomes small as the amount of adsorbed ^{4}He increases from 8.01 mmol to 8.40 mmol, while the T-linear term grows.

In Padmore's picture, ρ_n has a T-linear dependence when the geometry is zero dimensional as in the case of packed powders [69, 70]. One possible explanation of our data is that narrow sections of the pores are completely filled with liquid ^{4}He at 8.01 mmol and above, whereas ^{4}He coats the pores more or less uniformly for lower coverages. The completely filled sections represent a zero dimensional geometry to phonons, whereas one dimensional phonons come from the remainder. Another possible interpretation of the T-linear term is that it is an artifact due to ^{4}He in a dead volume outside the porous silica. As seen in Fig. 5.7, the 8.20 mmol curve is identical to the 8.01 mmol curve except near T_c and near the lowest temperature. The 8.40 mmol curve, not shown in the figure, is also nearly identical to the 8.01 mmol curve, except that it shows a hint of modulations that are clearly visible in Fig. 5.3 for coverages higher than 8.40 mmol. It is quite likely that the pores of the silica become full at around 8.01 mmol and the T-linear term is the response of the superfluid outside the silica superposed to the data.

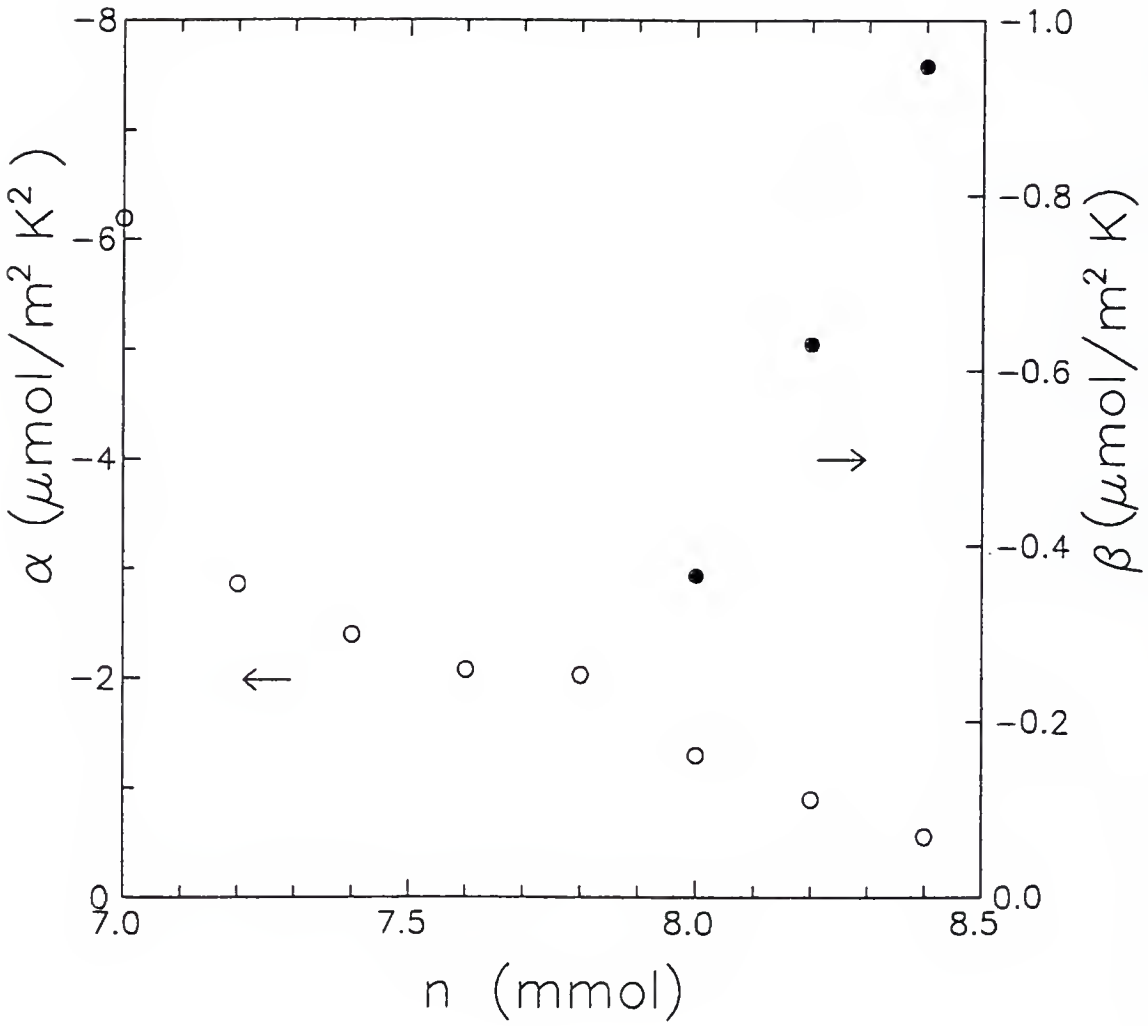

Figure 5.9. Fitting parameters for the $\alpha T^2 + \beta T$ dependence of the frequency data at low temperatures. Fit regions are $T < 0.15$ K for 7.00 and 7.21 mmol, $T < 0.2$ K for 7.40 mmol, and $T < 0.3$ K for larger amounts of ^{4}He .

According to Padmore [69], the temperature dependence of the normal-fluid density in a one dimensional channel is given by

$$\rho_{\rm n} = \frac{\pi\hbar}{3c\lambda^2 d_1 d_2}\,, \tag{5.4}$$

at temperatures for which $k_B T \ll \pi\hbar c/d_i$, where $i = 1, 2$. Here $\lambda = \hbar c/k_{\rm B}T$ is the characteristic wavelength of the thermal phonons, c is the phonon velocity, d_1 and d_2 are the widths of the channel, and $\rho_{\rm n}$ is the volume density of the normal component. Figure 5.10 shows the phonon velocity c obtained from the coefficient of the T^2 term given in Fig. 5.9. In the calculation, d_1 and d_2 are assumed to be 11 Å, the diameter of the pore excluding the localized layer of a 7.1 Å thickness. The phonon velocity is 11.4 m/sec at 7.00 mmol and increases to 15.2 m/sec at 7.40 mmol. The velocity remains around 15 m/sec between 7.4 mmol and 7.8 mmol. These values are about 20 times smaller than the phonon velocity of 239 m/sec in bulk liquid ^{4}He [59].

<u>Theory of Kotsubo and Williams.</u> Kotsubo and Williams [71] have applied the theory of Kosterlitz and Thouless [10] to a superfluid ^{4}He film on a single sphere to explain their results in packed Al_2O_3 powders. Two vortices of opposite signs in the film produce a flow field at (θ', ϕ') in spherical coordinates [72]

$$v_\theta = \frac{1}{2R}\frac{\hbar}{m}\left[\frac{\sin\theta\sin\phi'}{1-\sin\theta\sin\theta'\cos\phi'-\cos\theta\cos\theta'}\right] \tag{5.5}$$

and

$$v_\phi = \frac{1}{2R}\frac{\hbar}{m}\left[\frac{\sin\theta'}{1-\cos\theta'} + \frac{\sin\theta\cos\theta'\cos\phi'-\cos\theta\sin\theta'}{1-\sin\theta\sin\theta'\cos\phi'-\cos\theta\cos\theta'}\right]\,, \tag{5.6}$$

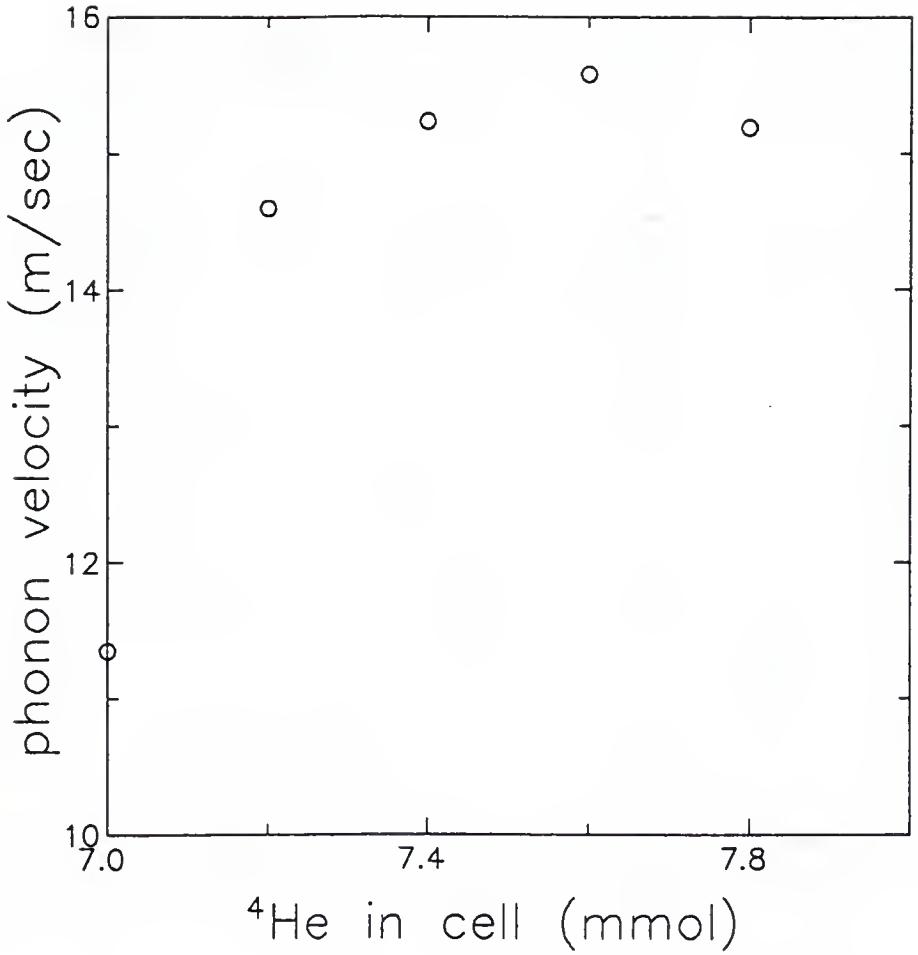

Figure 5.10. Phonon velocity obtained from ρ_n at low temperatures.

where m is the atomic mass of the ^{4}He and R is the radius of the sphere. One vortex is at $(0,0)$ and the other is at $(\theta,0)$. The vortex pair energy $U_0(\theta)$ is given by integrating $\frac{1}{2}\sigma_s^0 v_s^2$ over the film excluding the regions of vortex cores of radius a_0, which add $2E_c$ to the energy. Here σ_s^0 is the areal superfluid density. The integration yields [71]

$$U_0(\theta) = 2\pi K_0 \ln\left[\frac{\sin\{\frac{1}{2}(\theta-\theta_c)\}}{\sin(\frac{1}{2}\theta_c)}\right] + 2E_c\,, \tag{5.7}$$

where $\theta_c = a_0/R$ and $K_0 = (\hbar/m)^2\sigma_s^0$. In the limit of small θ and θ_c, the energy becomes that of Eq. 1.8 for a vortex pair on a flat substrate except that r/a_0 is replaced with $(r-a_0)/a_0$. As in the flat substrate case, the vortex pair is polarized in the presence of an external flow. Similar to Eq. 1.13, the polarizability $P(\theta)$ is given by [10]

$$P(\theta) = \frac{1}{2}\frac{\hbar}{m}\frac{\partial}{\partial v_{\rm ext}} < R\theta\cos\psi > |_{v_{\rm ext}=0}\,, \tag{5.8}$$

where ψ is the angle between the external flow and the arc connecting the centers of the vortex cores. Evaluating the thermal average with a weight $\exp(-U_0(\theta)/k_{\rm B}T - 2\pi K_0\frac{m}{\hbar}v_{\rm ext}\theta\cos\psi/k_{\rm B}T)$ leads to

$$P(\theta) = \frac{\pi}{2}(R\theta)^2\frac{K_0}{k_{\rm B}T}\,. \tag{5.9}$$

The screening effects of the polarized pairs determine the behavior of the superfluid density near the transition region. As in the flat substrate case, the screening effect is expressed by a dielectric constant $\epsilon(\theta) = 1 + 4\pi\chi(\theta)$, where the susceptibility $\chi(\theta)$ is given by

$$\chi(\theta) = \int_{2\theta_c}^{\theta} n(\theta')P(\theta')2\pi R^2\sin\theta' d\theta'\,. \tag{5.10}$$

Here $2\theta_c$ is $2a_0/R$, at which the two cores come in contact, $n(\theta)$ is the number density of vortex pairs with a separation angle θ and is given by

$$n(\theta) = \frac{y_0^2}{(2R\theta_c)^4} \exp(-U(\theta)/k_{\mathrm{B}}T)\,, \tag{5.11}$$

where $U(\theta)$ is the pair energy including the screening effect and $y_0 = \exp(-E_c/k_{\mathrm{B}}T)$. The energy $U(\theta)$ is determined by integrating the inter-vortex force as

$$U(\theta) = \int_{2\theta_c}^{\theta} \frac{1}{\epsilon(\theta')} \frac{dU_0}{d\theta'} d\theta'\,, \tag{5.12}$$

where $U_0(\theta')$ is the pair energy without the screening effect as given by Eq. 5.7. Defining $K(\theta) = (\hbar/m)^2\sigma_s^0/\epsilon(\theta)$ similar to $K(l)$ defined in Eq. 1.18 leads to the pair energy

$$U(\theta) = \int_{2\theta_C}^{\theta} \frac{\pi K(\theta')}{\tan[(\theta' - \theta_c)/2]} d\theta'\,, \tag{5.13}$$

where $K(\theta)$ obeys the equation

$$\frac{1}{K(\theta)} = \frac{1}{K_0} + \frac{4\pi^3 y_0^2}{(2\theta_c)^4 k_{\mathrm{B}}T} \int_{2\theta_c}^{\theta} (\theta')^2 \sin\theta' \exp(-U(\theta')/k_{\mathrm{B}}T) d\theta'\,. \tag{5.14}$$

Note that the experimentally observed the superfluid density is σ_s

$$\sigma_s = \frac{\sigma_s^0}{\epsilon(\pi)} = \frac{K(\pi)^2}{\hbar/m}\,, \tag{5.15}$$

which can be obtained at each temperature by performing the integal in Eq. 5.14 up to $\theta = \pi$. In the limit of large R, Eqs. 5.13 and 5.14 become the flat-substrate form

$$U(r) = \int_{2a_0}^{r} \frac{\pi K(r')}{r' - a_0} dr' \tag{5.16}$$

and

$$\frac{1}{K(r)} = \frac{1}{K_0} + 4\pi^3 \frac{y_0^2}{(2a_0)^4 k_B T} \int_{2a_0}^{r} (r')^3 \exp(-U(r')/k_B T) dr' . \tag{5.17}$$

Figure 5.11 shows the superfluid density obtained by Kotsubo and Williams from Eqs. 5.13 and 5.14 using $a_0 = 10$ Å, $E_c/K_0 = 2.2$ and $\sigma_s^0 = 5 \times 10^{-9}$ g/cm^2 for various radii of the sphere. As the ratio of the core radius to the sphere radius becomes smaller, the transition becomes broader as a consequence of the finite size of the sphere. In the case of the flat substrate, which corresponds to the limit $R \to \infty$, the superfluid density shows a sharp transition.

As discussed in Chapter 1, Nelson and Kosterlitz [14] have shown that the superfluid density σ_s on a flat substrate at the transition temperature T_c is given by a universal relation

$$\frac{\sigma_s(T_c)}{T_c} = \frac{2m^2 k_B}{\pi \hbar^2} = 3.49 \times 10^{-9} \mathrm{g/cm^2 K} . \tag{5.18}$$

Figure 5.12 shows the superfluid density as a function of temperature for various film thicknesses on a flat substrate and a sphere of a 150 Å diameter. The solid line represents the superfluid density given by Eq. 5.18 at the Kosterlitz-Thouless transition temperature.

<u>Analysis by the Kotsubo-Williams theory.</u> Table 5.3 shows the parameters obtained by fitting our superfluid density data to the Kotsubo-Williams theory. Figure 5.13 shows the

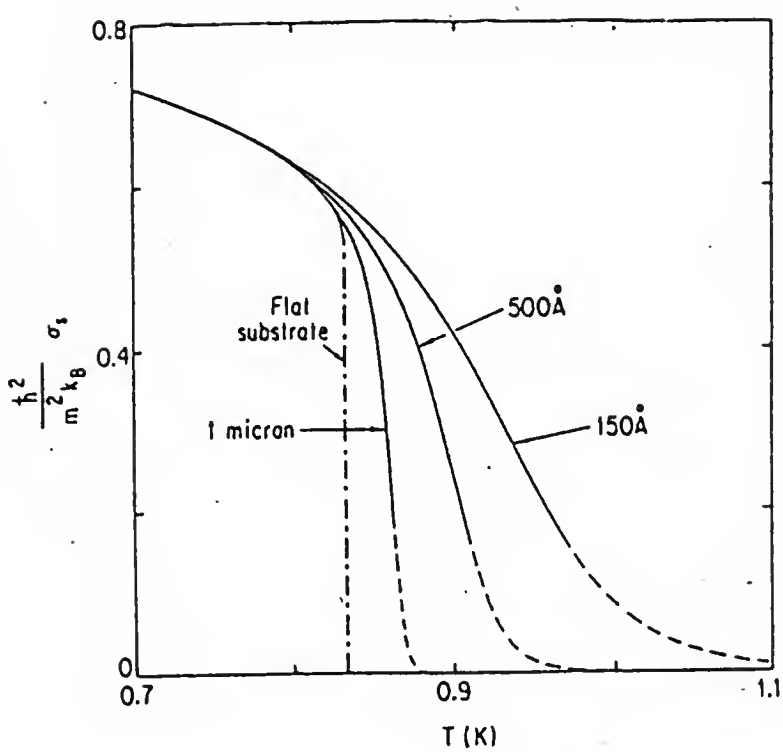

Figure 5.11. Superfluid density calculated by Kotsubo and Williams [71].

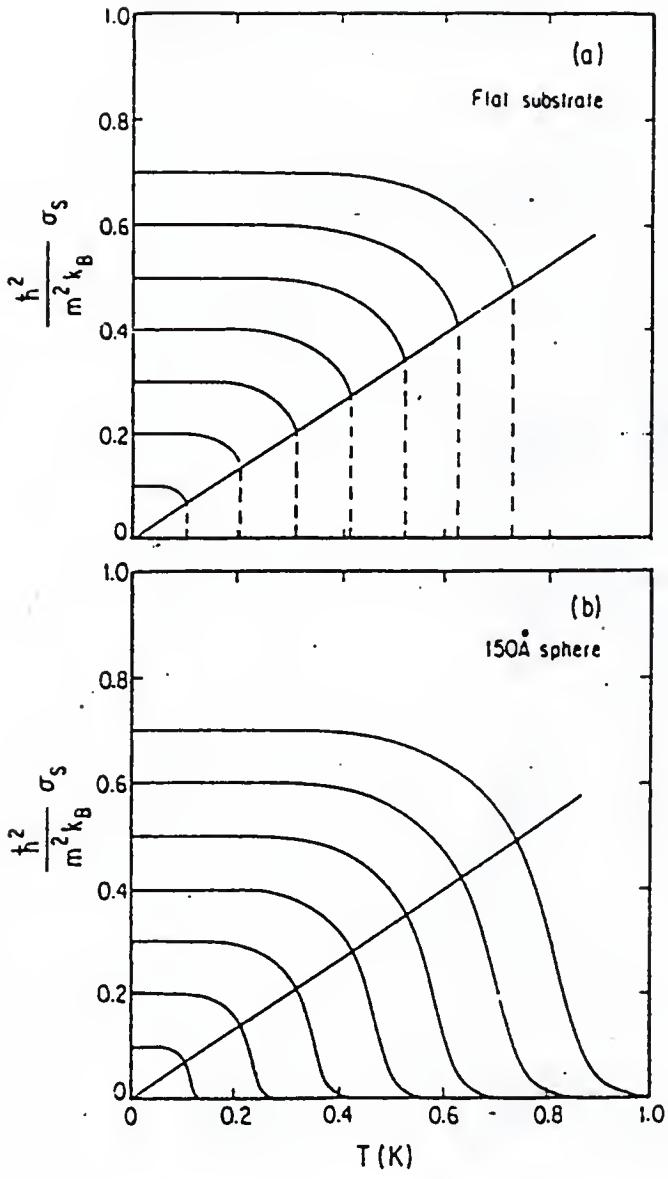

Figure 5.12. Superfluid density for various film thicknesses for the (a) flat substrate and (b) 150 Å diameter radius, after Kotsubo and Williams [71].

^{4}He in cell (mmol)	Core radius a_0 (Å)	Core energy E_c/K_0
7.00	4.3	1.1
7.21	2.9	1.2
7.40	3.8	1.5
7.60	6.0	1.7

Table 5.3. Fitting parameters with the Kotsubo-Williams theory. 6 Å was used as the sphere radius.

fits superimposed on the data. In the calculation the sphere radius R has been taken to be 6 Å by subtracting the two atomic layers of localized ^{4}He from the pore radius. The bare superfluid density σ_s^0 in the absence of vortex pairs has been obtained by extrapolating the T^2 fit discussed earlier in this chapter to higher temperatures. For consistency, the temperature region of the T^2 fits should be checked against the core energy obtained from the fit to the Kotsubo-Williams theory. The superfluid density σ_s for each coverage has been obtained from the frequency shift by taking into account the χ factor. The correction is equivalent to an assumption that all ^{4}He added over the critical coverage of 6.56 mmol becomes superfluid.

A striking aspect of these fits is that they fit the data for 7.80 mmol and 8.01 mmol very well over the entire temperature range, leaving no room for vortex pair unbinding to contribute to ρ_n. In contrast, the phonon contribution to ρ_n in the Al_2O_3 powder experiment of Cho and Kotsubo [68] is less than 30% of the total ρ_n near the critical region.

As seen in Table 5.3, the core radius equals the sphere radius at 7.60 mmol. This number is obviously unphysical, since there is no room for pairs which cause the screening effect. The theory of Kotsubo and Williams is inapplicable for the coverages of 7.60 mmol and higher.

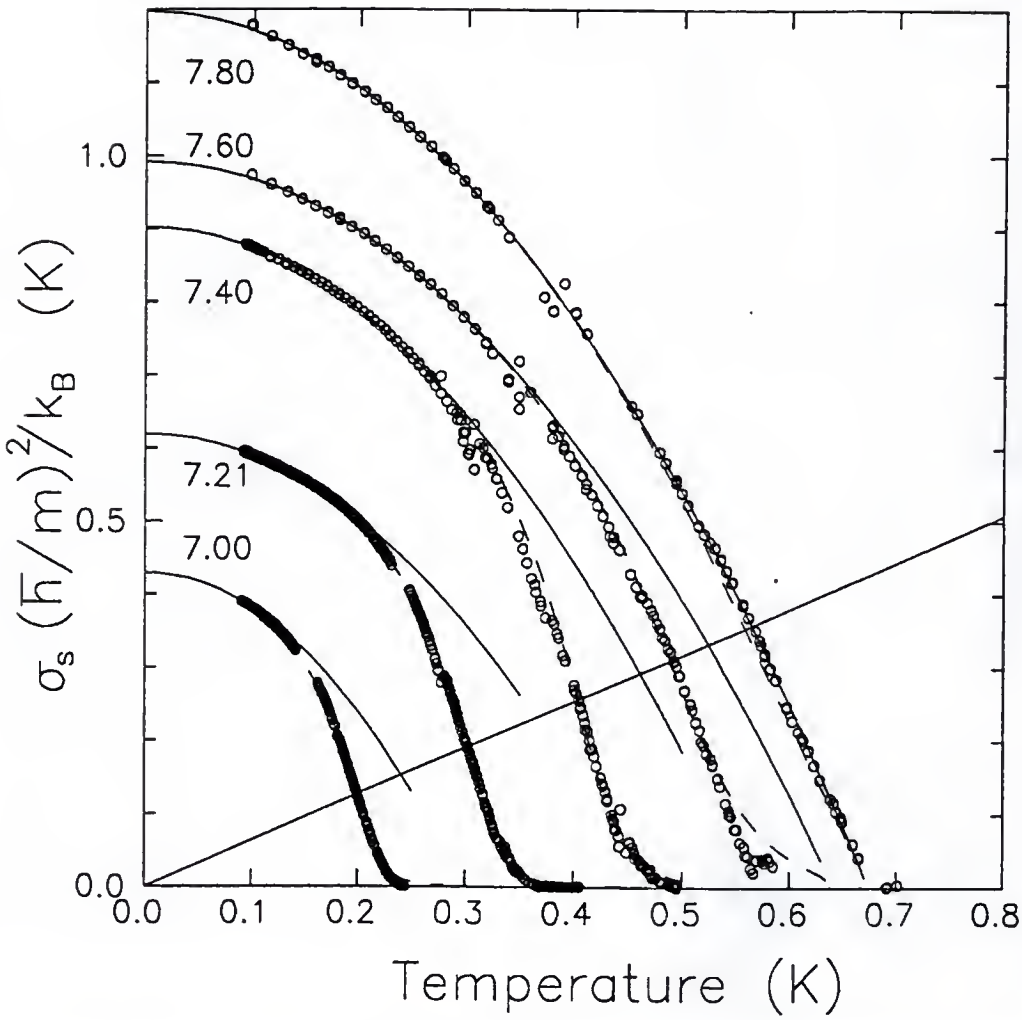

Figure 5.13. Superfluid density ρ_s. The solid lines are the calculations. The dashed lines are σ_s^0 obtained from the T^2 fits for the low temperature region. The broken lines are the fits to the formula of Kotsubo and Williams.

Figure 5.14 shows the core radius obtained in the packed Al_2O_3 powder experiment of Cho and Kotsubo [68]. The core radius increases as the coverage decreases. They argue that the core radius has to be on the order of the interparticle distance. Because a vortex core is a node of the order parameter, having zero amplitude at the center, the amplitude reaches an equilibrium value at infinite distance from the center. Since the order parameter cannot change as fast as the interparticle distance, the core radius cannot be smaller than the interparticle distance. The core radius obtained by Cho and Kotsubo is of the order of the interparticle distance. In our results, the core radius is an increasing function of coverage except for 7.00 mmol. This trend cannot be explained by the argument of Cho and Williams, casting doubt on the relevance of the theory of Kotsubo and Williams and the underlying mechanism of vortex-pair unbinding.

Universal jump. Cho and Kotsubo pointed out that their results reflect the universal jump [68] given by Eq. 5.18 in that the line representing the universal relation crosses the shoulder of the superfluid density curve as seen in Fig. 5.12. In Fig 5.13 the straight line represents the universal relation of Eq. 5.18. The experimental data have no shoulders that can be identified, indicating that the universal jump is probably irrelevant.

5.3 Conclusions

We have studied the superfluid transition of ^{4}He in 25 Å diameter pores of silica. Although the coherence length was much larger than the pore diameter in the critical region, the critical behavior of the superfluid density was close to a linear rather than a power law with critical exponent of roughly 2/3, observed in Vycor and packed powders. The critical exponent close to one is close to those seen in the full pore case of aerogel.

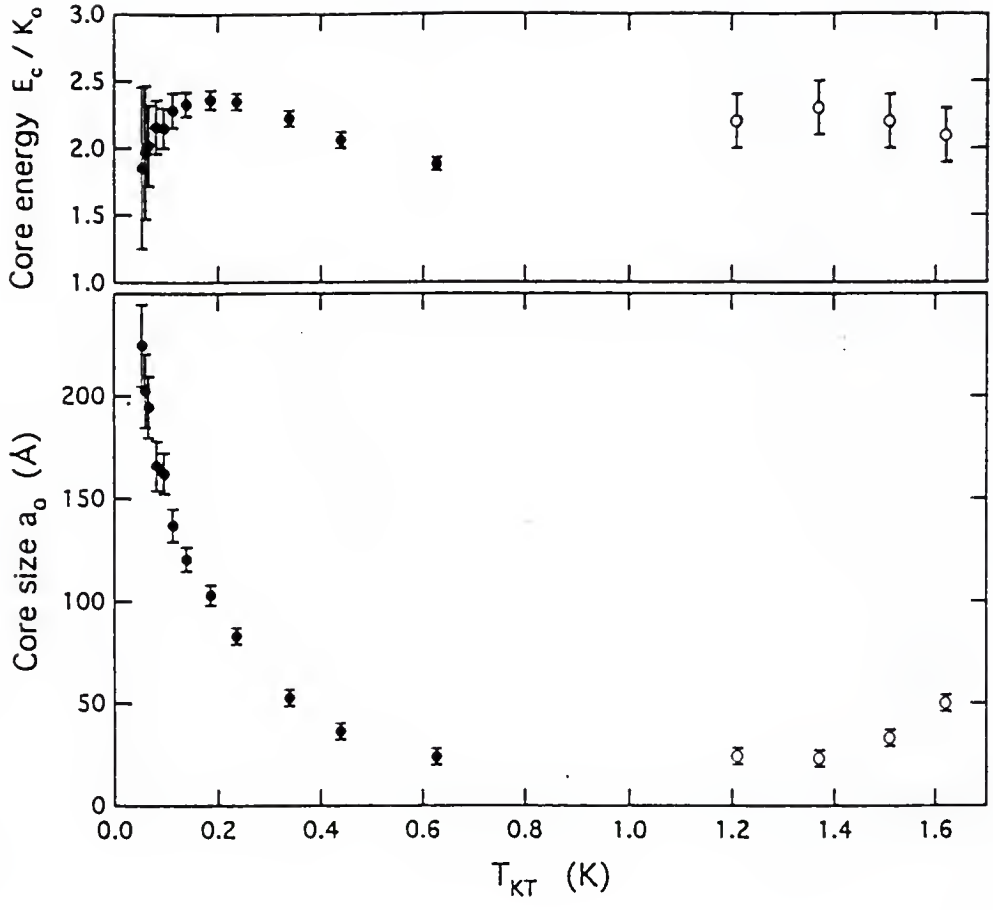

Figure 5.14. Core radius obtained by Cho and Kotsubo for 500 Å Al_2O_3 [68].

The low temperature fits of the phonon contribution to the normal-fluid density leave no room for vortex-unbinding contributions at higher temeratures for coverages above 7.80 mmol. The fit to the theory of Kotsubo and Williams yields an unphysical vortex radius even for the 7.60 mmol data. The universal relation, which is often used as evidence for vortex-pair unbinding being responsible for the superfluid transition, appears to be irrelevant in our results. This is the first clear observation of non vortex pair unbinding superfluid transition for a thin film of ^{4}He in a porous media. However, there is no clear explanation of what contributes to the normal component in the region where the fitting to the parabolic function deviates from the observed superfluid density.

APPENDIX A
HELIUM VAPOR PRESSURE THERMOMETER

A helium vapor pressure thermometer shown in Fig. A.1 has been built as a primary thermometer to calibrate the ruthenium oxide resistance thermometers described in Chapter 2. However, I have not had an opportunity to use the thermometer in the experiments described in this dissertation. The description of the thermometer is given here for those who will use it later in this laboratory.

In order to avoid the thermomolecular effect, the pressure transducer of the thermometer must be placed inside the cryostat and needs to be calibrated against an external standard located at room temperature. A piece of phosphor-bronze bellows with three convolutions from Robertshow [73] has been used as the pressure transducer, on which an electrode is attached to form a capacitor with a stationary electrode. The reference capacitor is included in the housing of the thermometer to eliminate the need to regulate its temperature. The value of the reference capacitor, 2.17 pF, has been chosen to be close to that of the transducer capacitor at zero pressure in order to maximize the pressure sensitivity of the capacitance bridge at the lowest temperature, where the vapor pressure is low. Nevertheless, the overall temperature sensitivity is larger at higher temperatures, where the vapor pressure is strongly temperature dependent. The gap between the two electrodes on the transducer side is chosen to give the maximum usable pressure of about 1/3 bar, which

corresponds to 3.2 K for the ^{4}He vapor and 2.4 K for the ^{3}He vapor. These temperatures are sufficiently high for our experiments whose temperature does not much exceed the superfluid transition temperature T_λ=2.17 K of the bulk ^{4}He.

The calibration of the pressure transducer is made against a Paroscientific 223AT pressure transducer located at room temperature. The calibration at helium temperature is done at pressures above 10 kPa, where the thermomolecular effect can be ignored. For lower pressures, the calibration has to be made at a higher temperature such as liquid nitrogen temperature and be adjusted by adding an overall constant to match the high-pressure calibration done at helium temperature in order to account for the temperature-dependent background. Figure A.2 shows the capacitance as a function of pressure at 77 K.

Capacitance bridge. The capacitance of the vapor-pressure thermometer has been measured with an ac bridge shown in Fig. A.3. The reader is referred to an excellent review by Adams [74] for detailed discussions of capacitance bridges used for vapor-pressure thermometers and for other devices based on strain gauges. In the diagram, C_r is the reference 2.17 pF capacitor, and C_x is the transducer capacitance. The excitation signal is supplied by the reference output of the PAR 124A lock-in amplifier through a Gertsch ST-100A transformer to isolate the ground. The condition for the balance is

$$\alpha C_x = (1-\alpha)C_r, \tag{A.1}$$

where α is the ratio transformer setting. When the balance is off, the output voltage of the bridge is

$$V_{\text{out}} = V\left(\alpha - \frac{C_r}{C_r + C_x}\right), \tag{A.2}$$

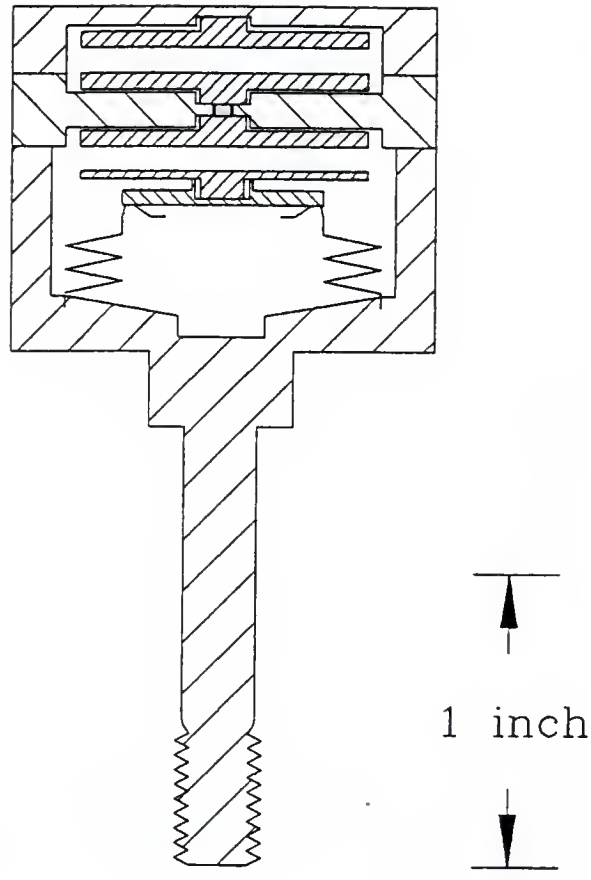

Figure A.1. Helium vapor pressure thermometer.

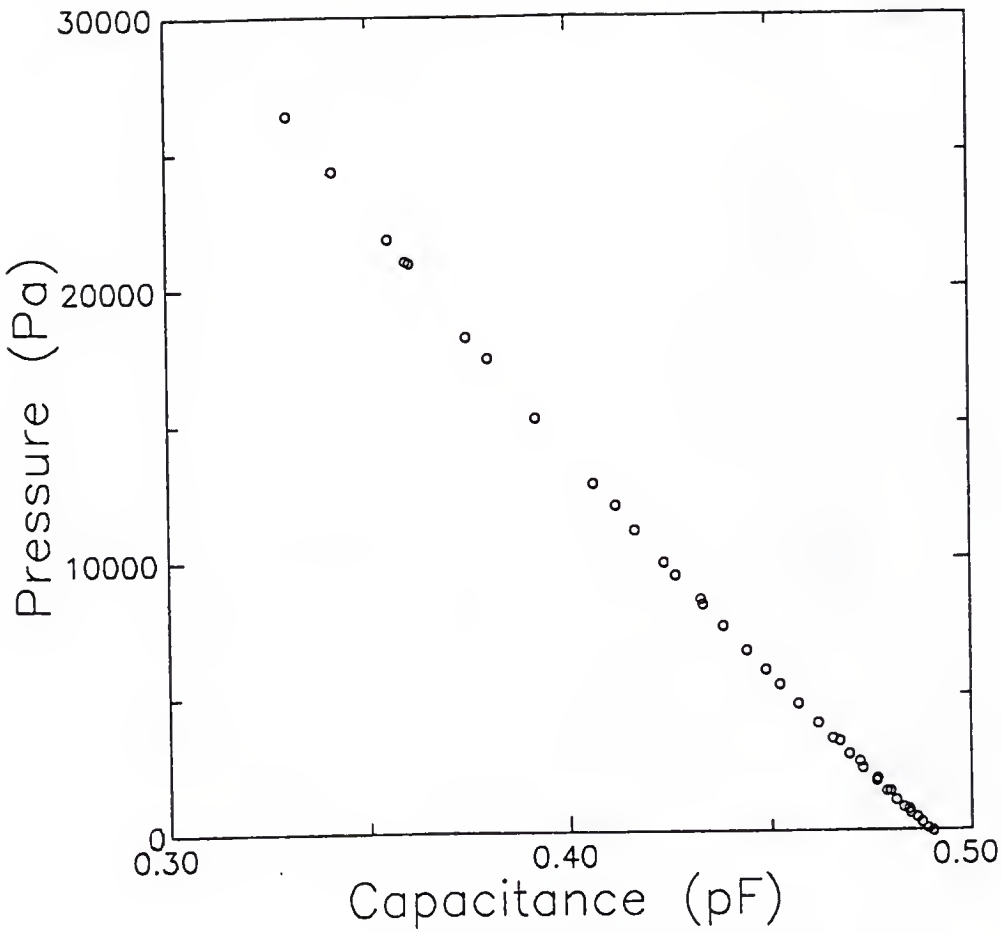

Figure A.2. Capacitance of the vapor pressure thermometer as a function of pressure at 77 K.

where V is the excitation voltage across the ratio transformer.

In the actual capacitance bridge the cables connecting the thermometer to the electronics have significant capacitances to the ground. The effect of the capacitances of the two cables to the ratio transformer can be ignored, because the impedance of each capacitance is roughly 0.5 MΩ at 1 kHz. However, the effect of the capacitance of the cable to the lock-in amplifier can be significant. The cable capacitance C_{cable} changes the denominator of Eq. A.2 to $C_x + C_r + C_{\text{cable}}$.

$$V_{\text{out}} = V \frac{\alpha C_x - (1-\alpha) C_r}{C_r + C_x + C_{\text{cable}}} . \tag{A.3}$$

Since C_{cable} is 200 $\sim$ 300 pF, whereas C_x and C_r are about 2 pF each, $C_r + C_x + C_{\text{cable}} \sim C_{\text{cable}}$, which means that the cable capacitance attenuates the output signal by $(C_r + C_x)/C_{\text{cable}}$. To minimize the cable capacitance, a preamplifier can be placed on the top of the cryostat before the lock-in amplifier.

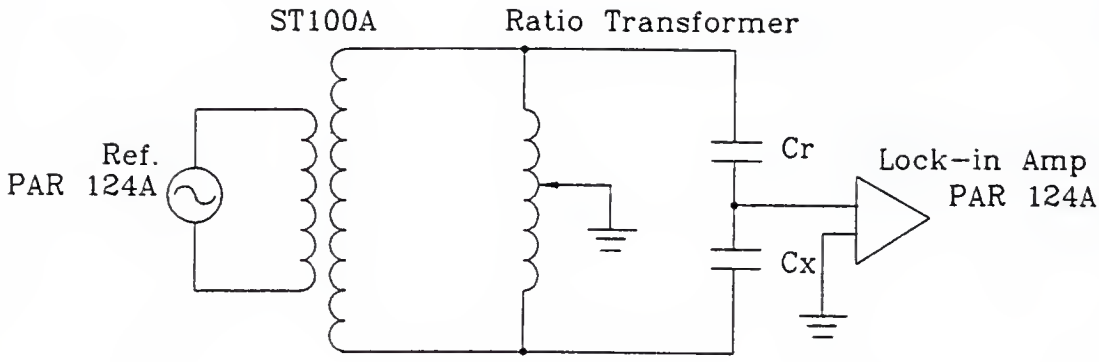

Figure A.3. Circuit diagram of the capacitance bridge for the vapor-pressure thermometer.

APPENDIX B
TORSION PENDULUM EXPERIMENT USING CHABAZITE CRYSTAL C16

This chapter describes an experiment using the first torsion pendulum containing a dehydrated chabazite crystal. The experiment was performed prior to a similar experiment discussed in Chapter 4. It was found at the end of the experiment that the crystal absorbed essentially no ^{4}He. However, a frequency anomaly was observed which can be attributed to the fountain effect. The results of this experiment as well as of a control experiment using a pendulum which contained no chabazite crystal are described here, because the anomaly shows features which we do not completely understand.

B.1 Results for the Torsion Pendulum Containing Chabazite

A torsional pendulum containing the chabazite crystal was identical in dimensions to that given in except for the sample cell. The crystal was $5 \times 5 \times 5$ mm in size and weighed 87.6 mg before dehydration. It was dehydrated in run C16 described in Chapter 3 and was expected to have a void volume corresponding to 0.43 mmol of nitrogen according to the nitrogen adsorption isotherm of smaller crystals dehydrated in the same batch.

Figures B.1 and B.2 show the temperature dependence of the resonance frequency of the pendulum up to 3.21 mmol of ^{4}He in the cell. The amplitude of the signal for the corresponding amounts of ^{4}He are shown in Figure B.3. The solid line at the top of Fig. B.1 was obtained without ^{4}He. In other frequency curves, a cusp or dips are seen slightly above 2 K. This is believed to be the superfluid transition of bulk liquid ^{4}He.

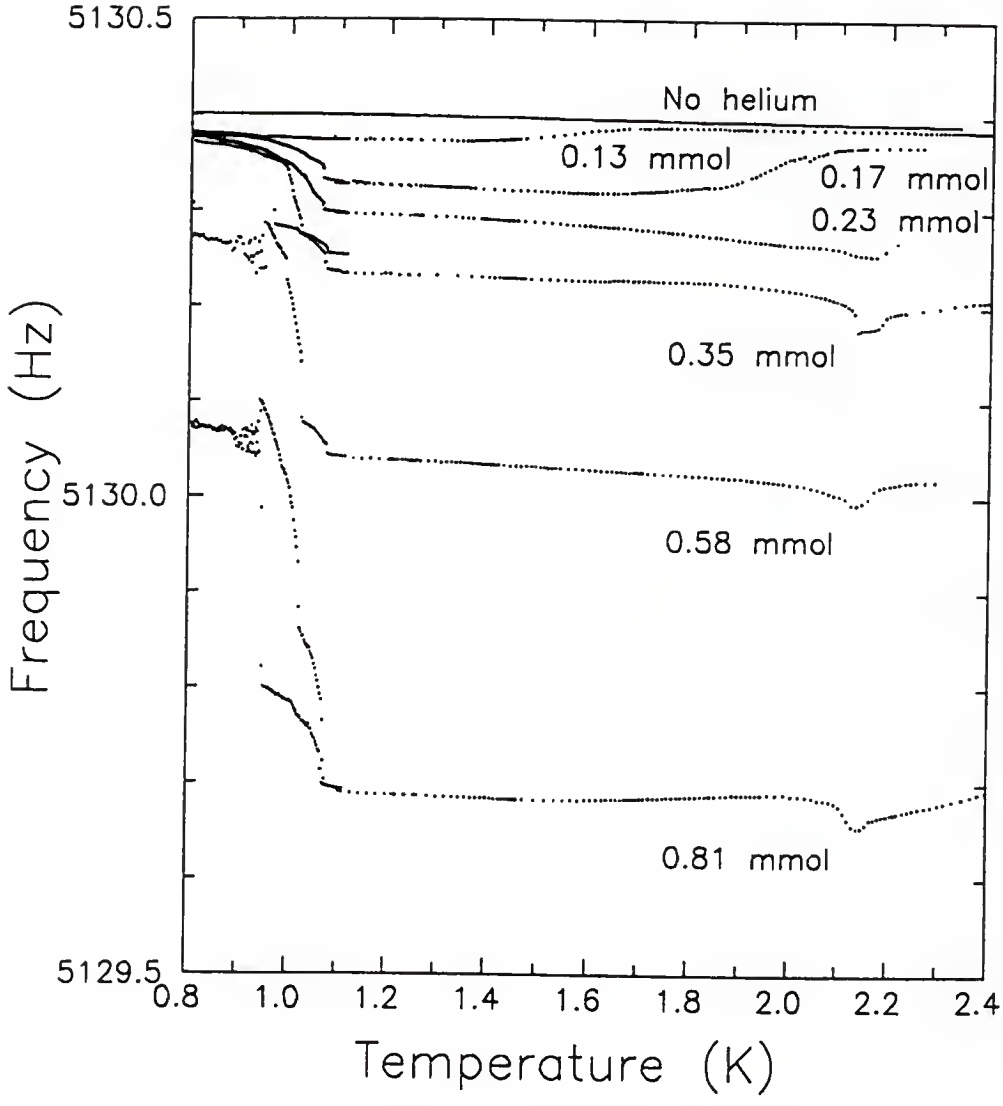

Figure B.1. Frequency of the torsion pendulum, containing chabazite crystal C16, as a function of temperature for various amounts of ^{4}He.

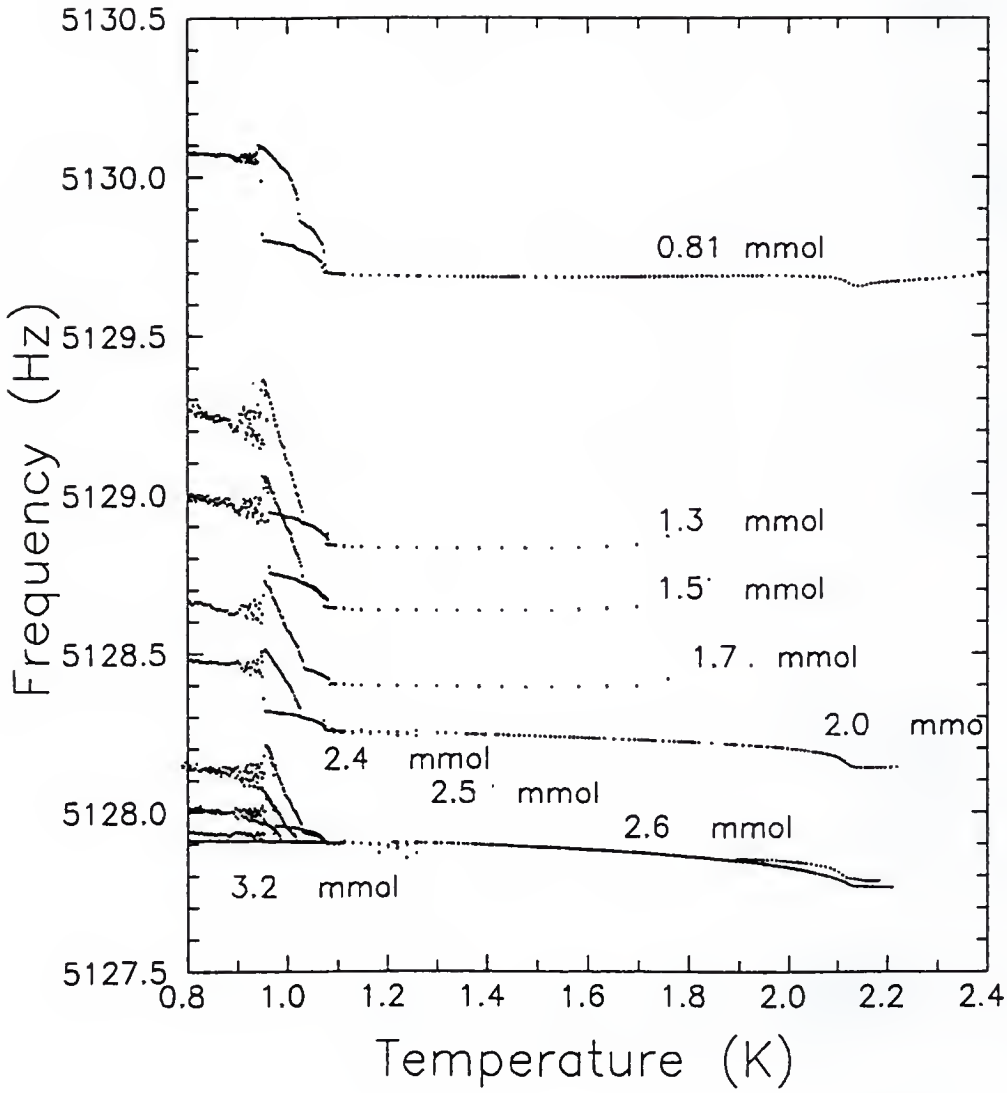

Figure B.2. Frequency as a function of temperature for various amounts of ^{4}He.

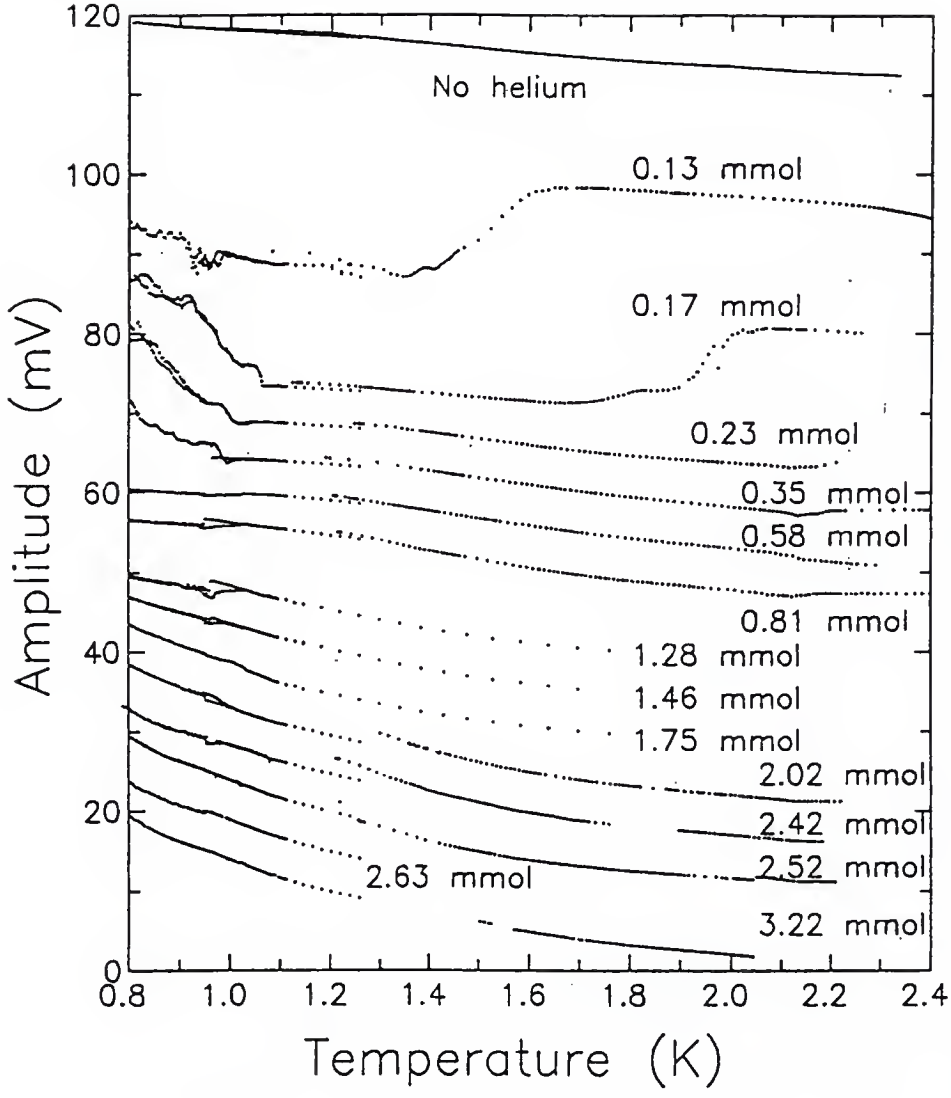

Figure B.3. Amplitude of the torsional pendulum containing chabazite crystal C16 as a function of temperature for various amounts of ^{4}He.

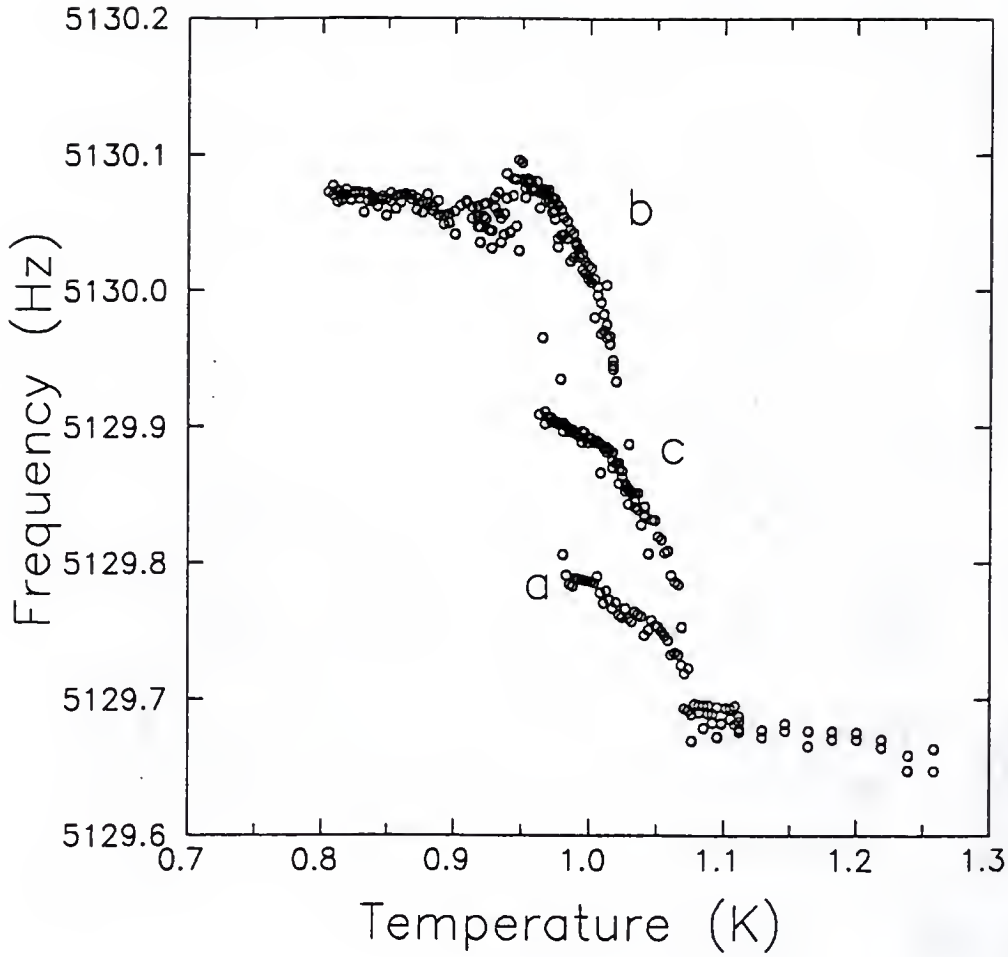

Figure B.4. Frequency of the torsional pendulum containing the chabazite crystal as a function of temperature showing history dependence. The amount of helium in the cell was 0.82 mmol. Curve *a* is the warming curve, *b* is the cooling curve, and *c* is the curve observed when the direction of the temperature sweep was reversed from warming to cooling below 1.0 K.

The most prominent feature of these results is a frequency anomaly at a temperature between 0.9 K and 1.1 K. The feature is unusual in that it exhibits history dependence, wheras all known superfluid transitions in ^{4}He . Figure B.4 shows a magnified view of this frequency feature for the 0.82 mmol data. Lines *a* and *b* are warming and cooling curves, respectively. When the direction of the temperature sweep was reversed from warming to cooling below 1.0 K, curve *c* was observed. Suhc a third frequency curve was observed only for this amount of ^{4}He. For other amounts of ^{4}He, only two distinct frequency curves were observed except for less than 0.35 mmol of ^{4}He for which the history dependence was no longer seen. The history dependence seen is quite similar to supercooling of liquids and unlike the hysteresis curves of ferrites which exhibit nested loops.

One important aspect of the frequency anomaly is that its onset temperature changes by less than 15 mK for the amount of ^{4}He between 0.35 mmol and 2.32 mmol. On the other hand, the frequency difference Δf between the low temperature side and the onset temperature depends on the amount of ^{4}He as shown in Fig. B.5. Δf initially increases with the amount of ^{4}He. Δf is largest for 1.16 - 2.32 mmol, above which it decreases until reaching zero at 2.61 mmol, as shown in Fig. B.5. Between 2.32 mmol and 2.61 mmol of ^{4}He, the shape of the frequency curve no longer depends on the amount of ^{4}He above the onset temperature. Below the onset temperature, the curve appears as if the lower frequency portion has been cut off while the remaining part looks very similar to the one for 2.32 mmol.

<u>Void volume of the chabazite crystal.</u> During the torsion pendulum experiment, a few thousand pascals of ^{4}He gas pressure was observed when the fill line valve was opened to let additional gas into the cell, even when the amount of ^{4}He in the cell was far less than

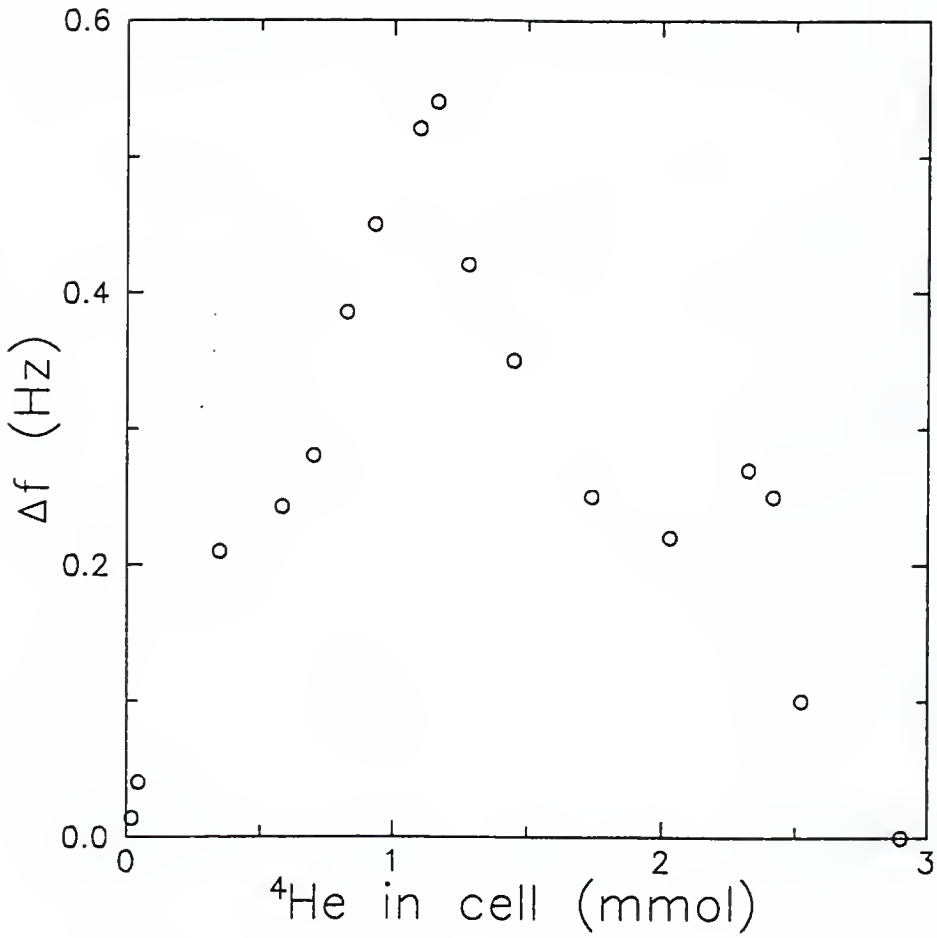

Figure B.5. Size of the frequency anomaly for various amounts of ^{4}He.

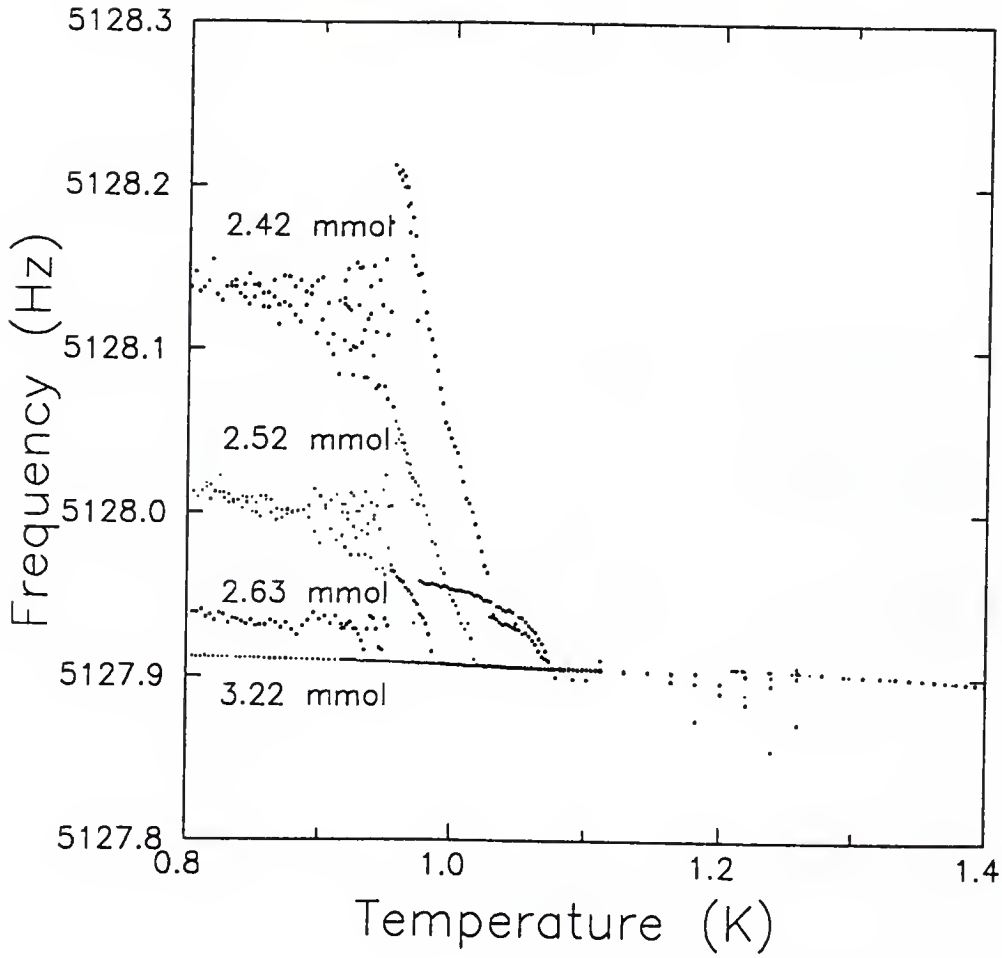

Figure B.6. Frequency of the torsional pendulum containing chabazite crystal C16 as a function of temperature for the amounts of ^{4}He larger than 2.32 mmol.

that needed to fill up the pores of the chabazite crystals. As with crystal C22 used in the experiment discussed in Chapter 4, this crystal was not checked for the adsorption of nitrogen gas prior to the experiment for fear of damaging it. Therefore, it was possible in principle that the crystal was not adsorbing ^{4}He. In order to test if this was the case, an adsorption isotherm of ^{4}He was measured at 4.2 K *in situ* after the torsion pendulum experiment was completed. Figure B.7 shows the result, from which the surface area of the crystal was determined to correspond to -0.01 ± 0.008 mmol of ^{4}He. The result indicates that there was no void volume in the crystal within the error of the measurement. Therefore, ^{4}He introduced into the sample cell remained outside the crystal during the torsional pendulum experiment and the frequency anomaly was due to bulk liquid ^{4}He residing in the dead volume of the cell. At this point, however, it is still possible that the chabazite somehow played a role in the frequency anomaly.

It remains unclear why the crystal had essentially no void volume. One possibility is that there was a small leak through the valve for the fill line. Although all solder joints on the fill line had been leak tested before installing the cell, the valve had not been checked for a leak. Another possibility is that the crystal did not lose water for an unknown reason, although small crystals prepared together with this crystal had an average void volume 85% of that of vacuum-dehydrated crystals.

<u>Bulk ^{4}He transition and the viscous penetration depth.</u> Having established that the frequency anomaly around 1 K is due to bulk ^{4}He in the dead volume, we can shed light on the anomaly by comparing its size with the frequency change due to the bulk superfluid transition at 2.17 K. The frequency change due to the superfluid transition is governed by the viscous penetration depth of ^{4}He. Above T_λ where liquid ^{4}He is normal, the pendulum

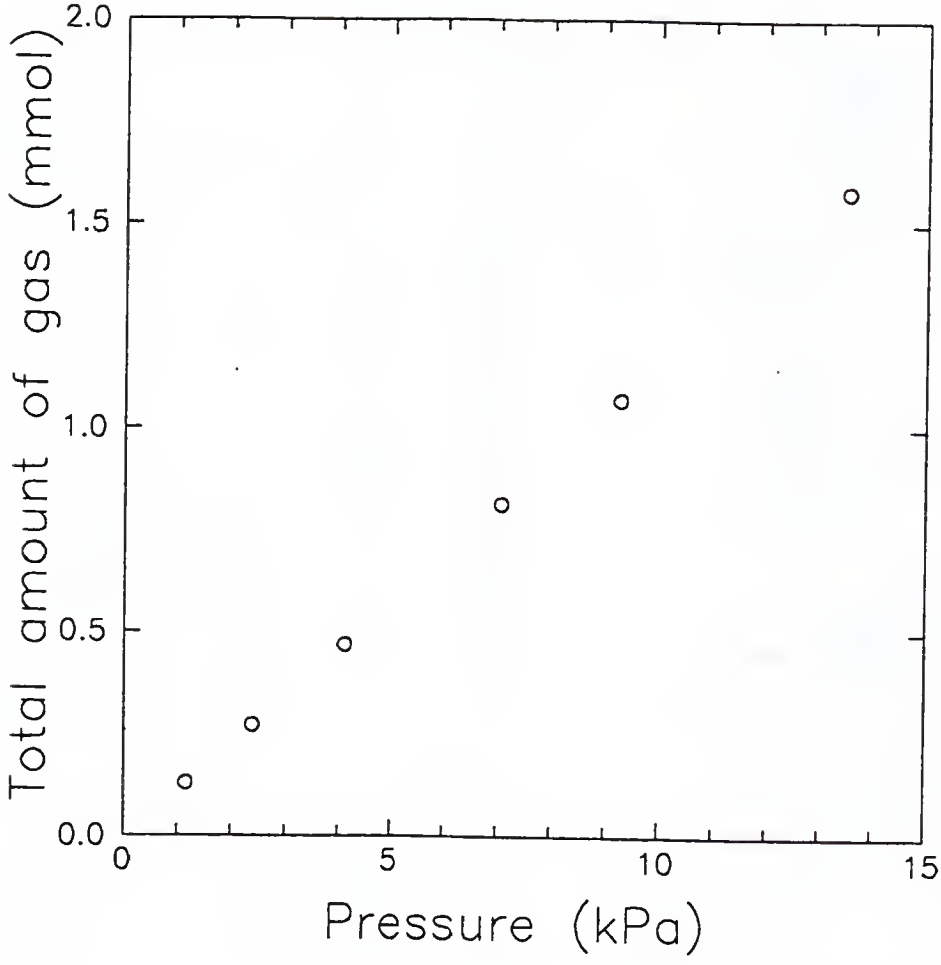

Figure B.7. Adsorption isotherm of ^{4}He at 4.2 K on chabazite crystal C22 used in the torsional pendulum experiment. The pressure is measured with the Digiquartz pressure transducer 223AT on the gas handling system located at room temperature. No corrections due to thermomolecular effect have been made.

couples to the liquid within the viscous penetration depth (about 1.1 μm at T_λ) with the walls of the cell and the exterior surface of the chabazite crystal. At temperatures far below T_λ, where little normal-fluid component is left, the pendulum completely decouples from the fluid. The frequency change can be estimated from the change in the moment of inertia of the fluid within the viscous penetration depth from the inner surfaces of the cell. The inner surface area of the cell is 0.81 cm^2 on the side and 0.20 cm^2 each on the top and the bottom. The exterior surface area of the chabazite crystal is roughly the same as the inner surface area of the cell. When these surfaces are covered with a ^{4}He film whose thickness exceeds the viscous penetration depth of about 1.1 μm, the moment of inertia is expected to change by $\Delta I = 1.67 \times 10^{-6}$ gcm^2 between T_λ and $T = 0$. The expected frequency change due to the bulk ^{4}He transition is, therefore, $\Delta f = \frac{1}{2} f \Delta I / I$ =0.15 Hz for f =5.1 kHz and $I = 1.67 \times 10^{-6}$ gcm^2, in good agreement with the actual frequency change of about 0.14 Hz.

At temperatures near 1 K, the viscous penetration depth increases by a factor of ten because the viscosity of the normal-fluid component increases rapidly as the temperature is lowered. However, the normal-fluid density decreases at the same time. As a result, the overall change of the moment of inertia near 1 K becomes about 1/10 of ΔI at T_λ. Since the frequency anomaly seen below 1.1 K is as large as 0.15 Hz for amounts of ^{4}He between 0.2 mmol and 2.5 mmol, it cannot be explained by a decoupling of ^{4}He through a change in the viscosity of the normal component.

B.2 Results for the Torsion Pendulum with an Empty Cell (A Control Experiment)

In order to determine the role of the chabazite crystal in the frequency anomaly, a new torsional pendulum was made with an empty cell whose dimensions were the same as those

of the cell containing the chabazite crystal. The frequency of this pendulum is shown in Fig. B.8 for various amounts of ^{4}He.

It is evident that the frequency anomaly below 1.1 K occurs without the presence of a chabazite crystal. The frequency curves are very similar to those of the pendulum containing the chabazite crystal except for an additional anomaly at around 1.6 - 1.7 K. The loading sensitivity, which is defined as the rate of frequency change due to a change in the amount of ^{4}He, was -1.17 Hz/mmol at 1.2 K for the chabazite cell and only -0.022 Hz/mmol for the empty cell. The frequency change through the anomaly was also much smaller in the empty cell.

In understanding these differences, it is important to note that the frequency of the empty cell at 0.9 K depended on the amount of liquid ^{4}He, even though the normal-liquid density is negligible at that temperature. This implies that the motion of the pendulum was not purely torsional. When the axis of the oscillation does not match the geometrical axis of the cell, the oscillation contains a small degree of floppy motion, which couples to the mass of the liquid. Since the chabazite crystal has a irregular shape, the principal axis of the moment of inertia of the cell which contains a chabazite crystal can be off from the geometrical axis of the cell. The frequency of such a cell has a high sensitivity to the mass of liquid ^{4}He.

In order to confirm this explanation, direct measurements were made of the floppy-mode frequency of the empty cell. The floppy mode couples to the entire mass of liquid ^{4}He and not only to the moment of inertia of ^{4}He within the viscous penetration depth.

As can be seen in Fig. B.9, the floppy mode shows the same frequency anomaly observed in the torsion mode. This indicates that the liquid actually moves out of the cell at 1.1 K. The size of the anomaly in the torsion mode and floppy mode roughly scales with the

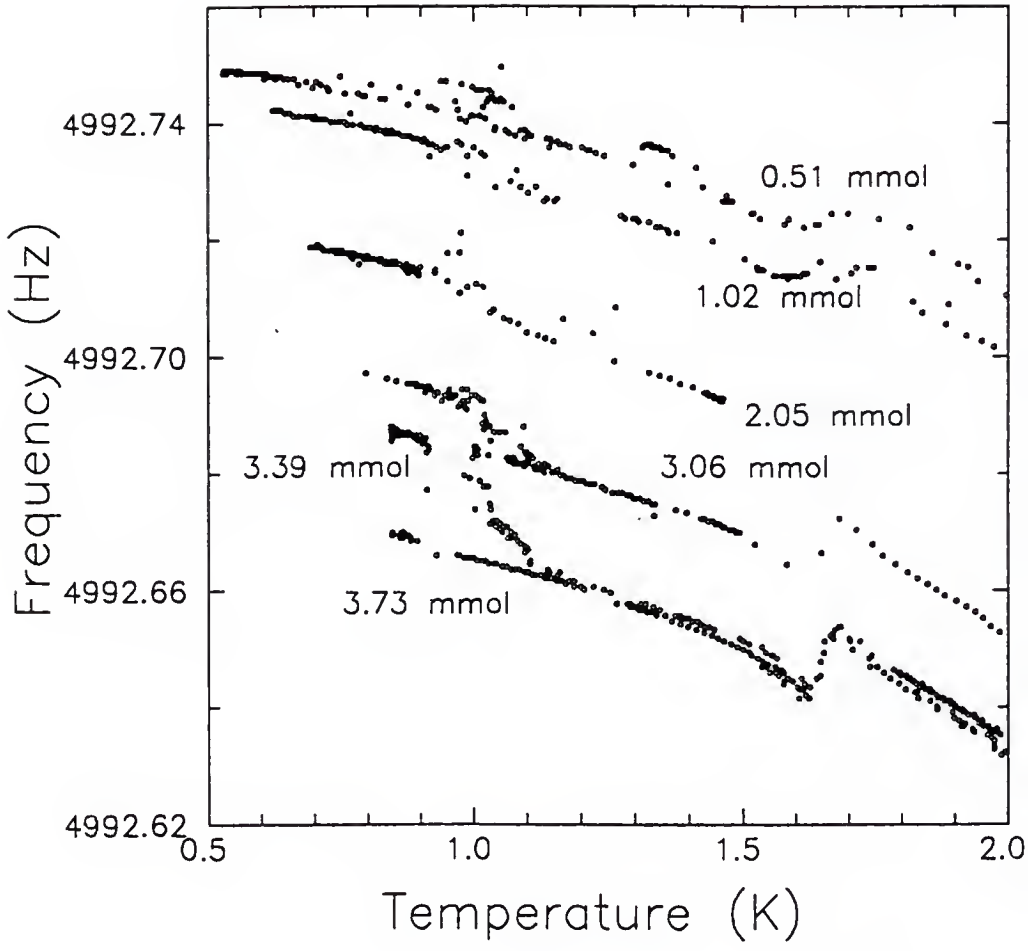

Figure B.8. Frequency of the torsional pendulum with an empty cell.

^{4}He-loading sensitivities of the two modes. This is seen in Fig. B.10, which shows the size of the anomaly scaled by the loading sensitivity, in other words the amount of liquid ^{4}He moving out of the cell, obtained from the torsion mode and the floppy mode.

B.3 Analysis and Conclusions

Onset temperature and the mechanism for the migration of liquid ^{4}He. When there is a temperature difference between two reservoirs connected with superfluid ^{4}He, the chemical-potential gradient creates a pressure difference between the reservoirs. This is called the fountain effect. H. London [75] first derived the equation

$$\frac{\Delta p}{\Delta T} = \rho\sigma \,, \tag{B.1}$$

for this effect. Here ρ is the mass density of liquid ^{4}He and σ is the entropy per unit mass.

Since bulk liquid ^{4}He is present in our cells, the inner surface of the fill line is covered with superfluid ^{4}He up to a point at which the temperature of the fill line reaches T_λ. When the cell is colder than the cold plate of the dilution refrigerator, there will be a pressure difference between the cell and the cold plate due to the fountain effect.

Since the cold plate is located 50 cm above the cell, the fluid does not actually move until the difference in the chemical potential becomes sufficient to overcome gravity. One can estimate the onset temperature by assuming that the temperature varies linearly in the fill line as a function of height from the sample cell and by integrating Eq. B.1 to obtain

$$\Delta p = \int_{T_1}^{T_2} \rho\sigma dT \,, \tag{B.2}$$

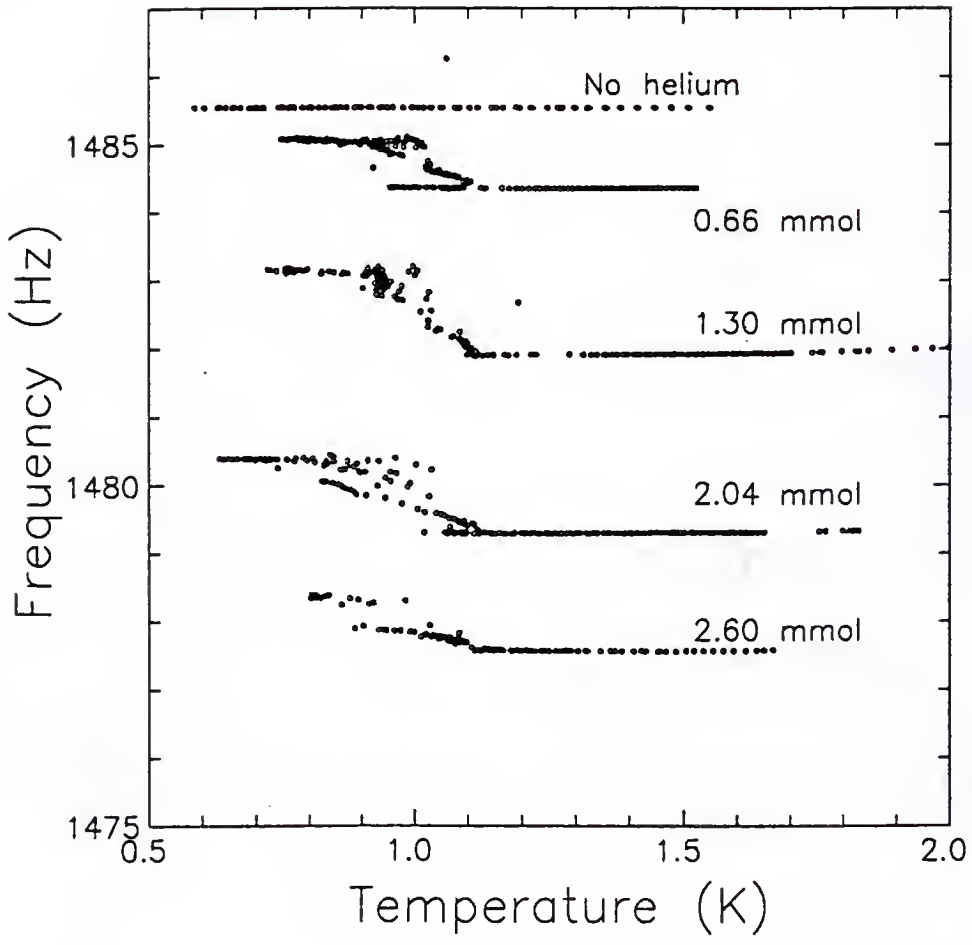

Figure B.9. Frequency of the floppy mode of the torsional pendulum with an empty cell.

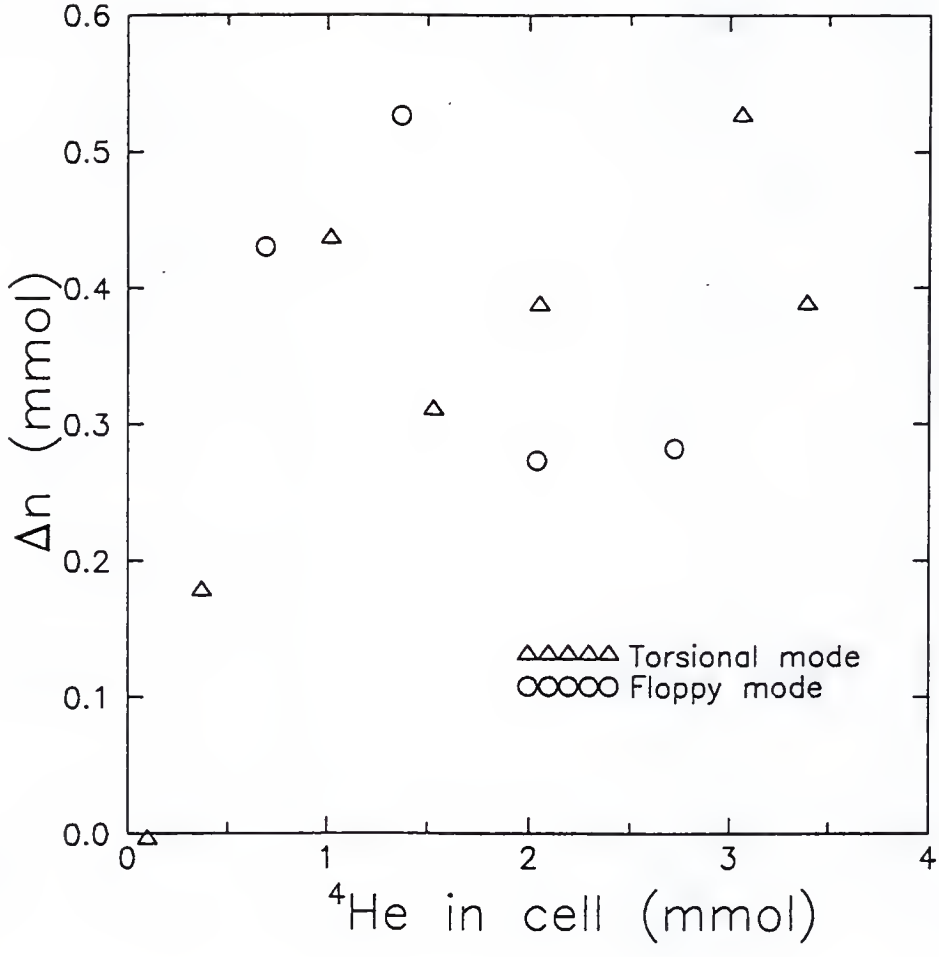

Figure B.10. Amounts of liquid ^{4}He escaping from the cell containing no chabazite detected in the torsional mode and the floppy mode.

where T_1 is the temperature of the cell and T_2 is the temperature of the cold plate. The hydrostatic pressure is $\rho g l$, where g =980 cm/s^2 is the acceleration of gravity and l simeq 50 cm is the vertical distance of the cold plate from the cell. By equating Δp with $\rho g l$, one predicts that the onset occurs when 4.9×10^4 erg/g $= \int_{T_1}^{T_2} \sigma dT$. Figure. B.11 shows the plot of $\int_0^T \sigma dT$ as a function of temperature. From the onset temperature T_1 of 1.1 K, T_2 is found to be about 1.3 K, somewhat lower than the actual temperature of the cold plate (about 1.5 K).

Since the difference in height between the high temperature end of the fill line and the liquid level determines the onset temperature according to our picture, it is expected that the onset temperature increases by a small amount as the liquid level rises in the cell. The change in the onset temperature when the liquid level rises from the bottom of the cell to the top is estimated to be about 10 mK. Figure B.12 shows the onset temperature as a function of the amount of ^{4}He on a magnified scale. The onset temperature increases by 14 mK from 0.4 mmol to 1.6 mmol, in good agreement with the estimate. Near the smallest amount of ^{4}He, the onset temperature decreases much more rapidly than expected from our picture. This may be due to surface tension. For the largest amount of ^{4}He, the onset temperature becomes smaller again. This is an artifact when the liquid level exceeds the top of the cell as explained below.

<u>Disappearance of the anomaly.</u> The frequency anomaly in the torsional pendulum containing the chabazite cell disappeared when the amount of ^{4}He exceeded 2.61 mmol. Further increasing the amount of helium in the cell did not change the base frequency. The estimated dead volume in the cell suggests that the cell was completely filled with liquid ^{4}He at this point.

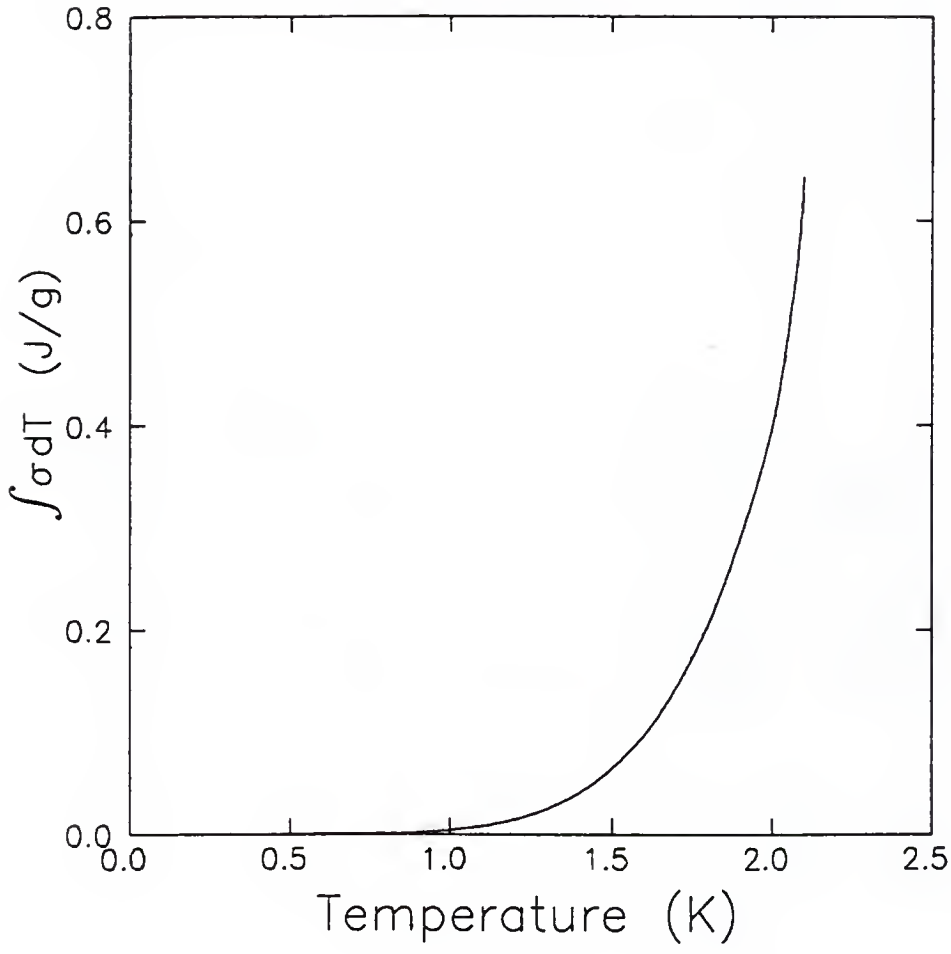

Figure B.11. $\int_0^T \sigma dT$ as a function of temperature for superfluid ^{4}He.

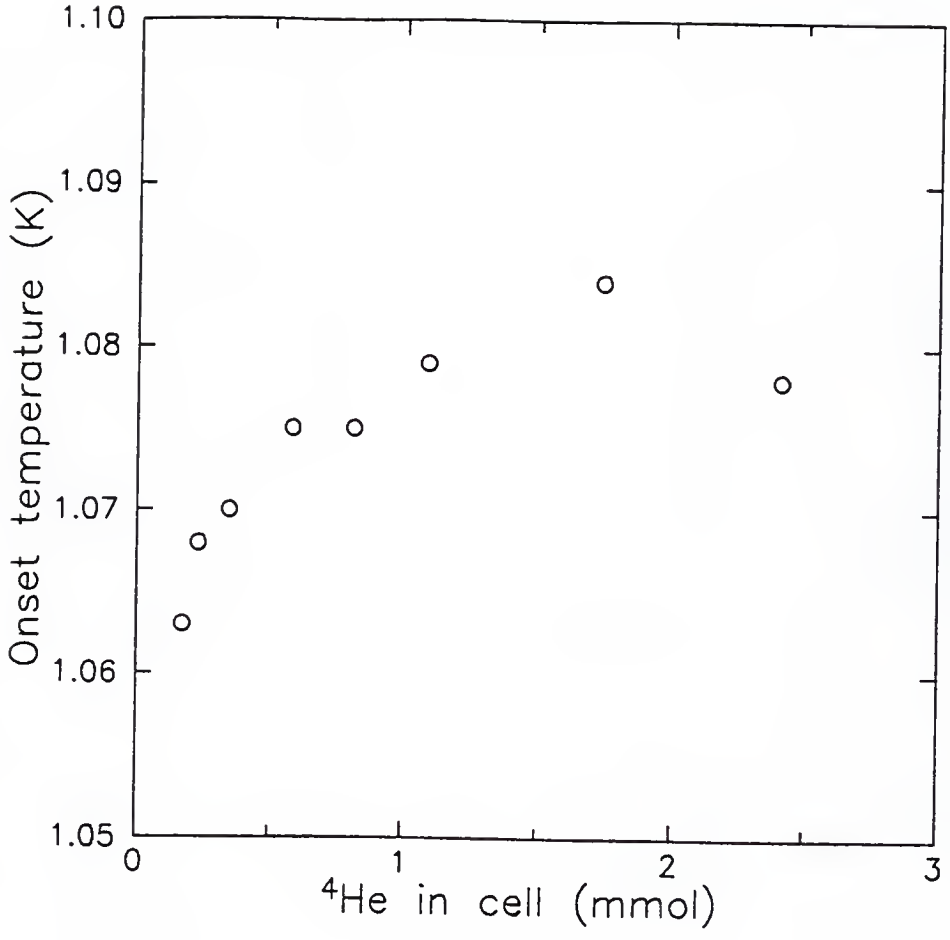

Figure B.12. Onset temperature of the anomaly observed in the frequency of the tosional peudulum containing chabazite crystal C16, as a function of the amount of ^{4}He.

When the amount of ^{4}He exceeds the capacity of the cell so that the level of the liquid is still above the cell after some liquid has moved up, the frequency anomaly will not be seen. If the level is above the cell at temperatures above the onset temperature and the level reaches the cell as some of the liquid moves out, one will begin to see the frequency changing at the point when the liquid level reachs below the top of the cell. Since the mechanism for liquid escaping from the cell is independent of whether or not the level is in the cell, the shape of the frequency curve should be the same as that for lower amounts of ^{4}He.

Size of the frequency anomaly as a function of the amount of ^{4}He. The frequency anomaly observed for the torsion penudulum containing the chabazite crystal has a maximum around 0.9 mmol as seen in Fig. B.13. On the other hand, the size of the frequency anomaly in the penudulum without a chabazite crystal varies monotonically with the amount of ^{4}He. The peak in the former case arises from the shape of the chabazite crystal. As shown in Fig. 4.1, the crystal occupies more space in the middle and less at the bottom and the top of the cell. When the liquid level is near the middle of the cell, the change in the liquid level due to ^{4}He escaping from the cell is larger than when the level is near the bottom or the top. This results in the maximum, since the amount of liquid which moves out of the cell depends only on the temperature difference between the cell and the cold plate and not on the amount of liquid in the cell.

Cause of the history dependence. It is unclear at present why the frequency, hence the amount of ^{4}He escaping from the cell, depends on the temperature history. There is, however, one possible scenario which may explain the frequency behavior. When the cell temperature becomes lower than the onset temperature, the ^{4}He film inside the section

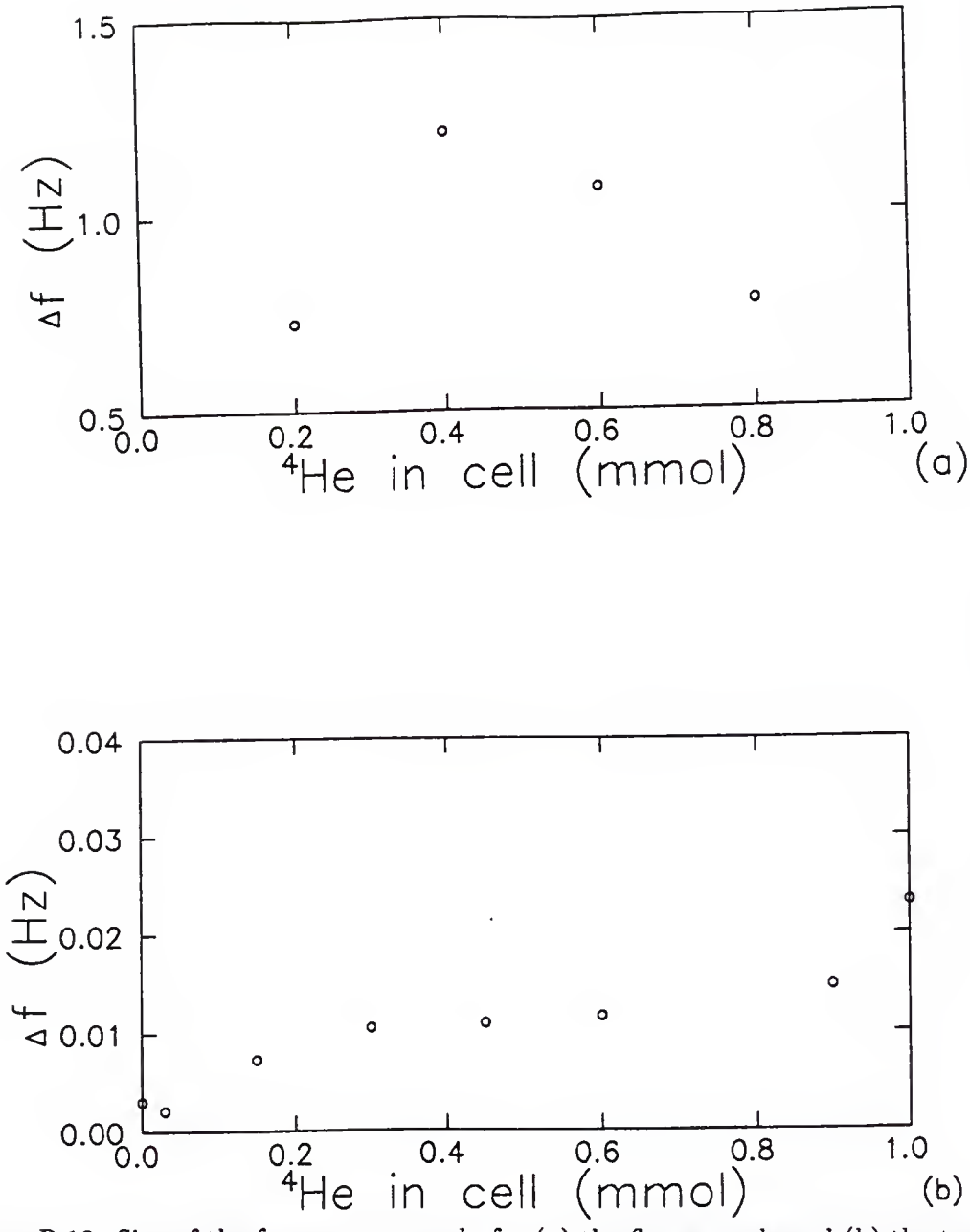

Figure B.13. Size of the frequency anomaly for (a) the floppy mode and (b) the torsional mode of the torsional pendulum containing chabazite crystal C16 as a function of the amount of ^{4}He.

of the fill line which is between the cold plate and the still starts to build up. When the film is thick enough, this section of the fill line becomes completely filled with liquid ^{4}He. This causes the sudden jump up in frequency at 0.9 K on the cooling curve. When the temperature is raised, liquid ^{4}He in the fill line starts to descend to the cell while a section of the fill line is still filled with the liquid. At the point where the cooling curve and the warming curve meet slightly below the onset temperature, no section of the fill line is completely filled with the liquid.

B.4 Conclusions

Liquid ^{4}He escaping from the cell due to a fountain effect can explain several features we have observed, either quantitatively or qualitatively. There are, however, a few things which cannot be explained by this picture. One is the complex structure of the frequency curves at 0.9 K and below. The rapid frequency change in the temperature region suggests an instability in the liquid held in the fill line. We do not, however, have any explanation regarding this feature. Another feature for which we have no explanation is the third frequency curve observed for 0.66 mmol of ^{4}He.

The third puzzling aspect of the data is the wide temperature range (0.9 K - 1.1 K) over which the frequency rises. Our estimate of the onset temperature was merely determined by the competition between the fountain pressure and the gravitational force. Once below the onset temperature, all of the liquid in the cell should move out within 15 mK, the speed of the onset temperature due to the change in the liquid level inside the cell. In order to explain the wide temperature range, one must introduce another mechanism which affects the pressure difference. One possible mechanism is the heat conduction by the liquid ^{4}He in the fill line. Superfluid ^{4}He has a very large thermal conductivity near T_λ because the second

sound can carry entropy with the sound velocity which is about 20 m/sec. This will make the temperature difference between the cell and the upper part a little smaller but does not appear to be sufficient to explain the wide temperature range of the anomaly.

REFERENCES

[1] E. L. Andronikashivili. *Zh. Eksp. Theo. Fiz.*, 16:780, 1946.

[2] L. D. Landau. *J. Phys. USSR*, 5:71, 1941.

[3] L. D. Landau. *J. Phys. USSR*, 11:91, 1947.

[4] L. Tisza. *Nature*, 141:913, 1938.

[5] D. R. Tilley and J. Tilley. *Superfluidity and Superconductivity.* Adam Hilger, 1974.

[6] D. G. Henshaw and A. D. B. Woods. *Phys. Rev.*, 121:1266, 1961.

[7] D. J. Bishop, PhD thesis, Cornell University, 1978 (unpublised).

[8] G. Agnolet, PhD thesis, Cornell University, 1983 (unpublised).

[9] G. Agnolet, D. F. McQueeney, and J. D. Reppy. *Phys. Rev. B*, 39:8934, 1989.

[10] J. M. Kosterlitz and D. J. Thouless. *J. Physics*, C6:1181, 1973.

[11] J. M. Kosterlitz and D. J. Thouless. *Progress in Low Temperature Physics*, volume 7. North Holland Publishing Co., Amsterdam, 1980.

[12] J. S. Langer and J. D. Reppy. *Progress in Low Temperature Physics*, volume 6. North Holland Publishing Co., Amsterdam, 1980.

[13] Sir. Horace Lamb. *Hydrodynamics.* Dover Publications, N.Y., 1945.

[14] D. R. Nelson and J. M. Kosterlitz. *Phys. Rev. Lett.*, 39:1201, 1977.

[15] B. C. Crooker, B. Hebral, E. N. Smith, Y. Takano, and J. D. Reppy. *Phys. Rev. Lett.*, 51:666, 1983.

[16] J. E. Berthold, D. J. Bishop, and J. D. Reppy. *Phys. Rev. Lett.*, 39:348, 1977.

[17] V. Kotsubo and G. A. Williams. *Phys. Rev. Lett.*, 53:691, 1984.

[18] T. Minoguchi and Y. Nagaoka. *Jpn. J. Appl. Phys.*, 26:327, 1987.

[19] J. Machta and R. A. Guyer. *Phys. Rev. Lett.*, 60:397, 1988.

[20] K. Shirahama, M. Kubota, S. Ogawa, N. Wada, and T. Watanabe. *Phys. Rev. Lett.*, 64:1541, 1990.

[21] M. P. A. Fisher, P. B. Weichman, G. Grinstein, and D. S. Fisher. *Phys. Rev. B*, 40:546, 1989.

[22] N. Trivedi and S. Ullah. *J. Low Temp. Phys.*, 89:67, 1992.

[23] N. Wada, H. Kato, and T. Watanabe. *J. Low Temp. Phys.*, 95:507, 1994.

[24] R. C. Richardson and E. N. Smith. *Experimental Techniques in Condensed Matter Physics at Low Temperatures.* Addison-Wesley Publishing Company, Inc., 1988.

[25] Bertan Associates Inc., 121 New South Rd., Hicksville, NY 11801, phone:(516)433-3110.

[26] Princeton Applied Research, P.O. Box 2565, Princeton, NJ 08540, phone:(609)452-2111.

[27] P. Horowitz and W. Hill. *The Art of Electronics.* Cambridge University Press, Cambridge, 1980.

[28] P. P. Craig and J. R. Pellam. *Phys. Rev.*, 108:1109, 1957.

[29] M. W. Meisel, G. R. Stewart, and E. D. Adams. *Cryogenics*, March 1989.

[30] Caddock Electronics, Inc., 1717 Chicago Avenue, Riverside, CA 92507-2346, phone:(714)788-1700.

[31] A. C. Anderson. *Rev. Sci. Instrum.*, 44:1475, 1973.

[32] Amidon Associates, Inc., 12033 Otsego St. N. Hollywood, CA 91607, phone:(818)760-4429.

[33] Microsoft Corp., 16011 NE 36th Way, Box 97017, Redmond, WA 98073-9717.

[34] Inland Vacuum Industries, 35 Howard Ave. P.O. Box 373, Churchville, NY 14428, phone:(800)962-8099, FAX:(716)293-3093.

[35] ULVAC Technologies Inc., 6 Riverside Dr., Andover, MA 01810, phone:(508)686-7550 ,FAX:(508)689-6300.

[36] Du Pond, Condord Plaza-Read Bldg. Wilmington, DE 19898, phone:(302)772-6120.

[37] M. Locatelli, D. Arnaud, and M. Rotin. *Cryogenics*, page 374, 1976.

[38] Linear Research, 5231 Cushman Place.

[39] Supercon Inc., 830 Boston Turnpike Rd., Shrewsbury, MA 01545, phone:(617)842-0174.

[40] High Pressure Equipment Company, Inc., 1222 Linden Avenue, Erie, PA 16505, phone:(814)838-2028.

[41] Paroscientific, Inc., 4500 - 148th Ave. NE, Redmond, WA 98052.

[42] D. W. Breck. *Zeolite Molecular Sieves.* John Wiley and Sons.

[43] M. Koizumi. *Min. J.*, 1:36, 1953.

[44] R. J. Argauer and G. R. Landolt, US Patent 3,702,886 (1972).

[45] Mobil Co., Netherland Patent 7,014,807 (1971).

[46] J. V. Smith, C. R. Knowles, and F. Rinaldi. *Acta. Cryst.*, 17:374, 1964.

[47] J. V. Smith. *Acta. Cryst.*, 15:835, 1961.

[48] R. M. Barrer. *Zeolites and Clay Minerals as Sorbents and Molecular Sieves.* Academic Press, 1978.

[49] D. M. Ruthven. *Principles of Adsorption and Adsorption Processes.* John Wiley and Sons, 1980.

[50] S. Brunauer, L. S. Deming, W. E. Deming, and E. J. Teller. *J. Am. Chem. Soc.*, 62:1723, 1940.

[51] I. Langmuir. *J. Chem. Soc.*, 40:1361, 1918.

[52] R. C. Weast, editor. *Handbook of Chemistry and Physics.* CRC Press., 1977.

[53] Douglass Randall, 6 Pawcatuck Avenue, Pawcatuck, CT 02891, phone:(203)-599-2075.

[54] S. S. Kistler, U. S. Patent 2,093,454 (1934).

[55] Fel-Pro, Inc., 7450 North McCormick Blvd. P.O. Box 1205, Skokie, IL 60076-8205, phone:(312)761-4500.

[56] M. Aoki. *J. Japn. Assoc. Miner. Petr. Econ. Geol.*, 73:155, 1978.

[57] R. J. Torii, H. J. Maris, and G. M. Seidel. *Phys. Rev. B*, 41:7167, 1990.

[58] Geltech Inc., One Progress Blvd. Box 8, Alachua, FL 32615, phone:(904)462-2358, FAX (904)462-2993.

[59] H. L. Anderson, editor. *The Second Edition of the Physics Vade Mecum.* American Institute of Physics, New York, 1989.

[60] D. F. Brewer, A. J. Symonds, and A. L. Thomson. *Phys. Rev. Lett.*, 15:182, 1965.

[61] S. Brunauer, P. H. Emmett, and E. Teller. *J. Am. Chem. Soc.*, 60:309, 1938.

[62] G. K. S. Wong, P. A. Crowell, H. A. Cho, and J. D. Reppy. *Phys. Rev. Lett.*, 48:3858, 1993.

[63] K. A. Shapiro and I Rudnick. *Phys. Rev. A*, 137:1383, 1965.

[64] B. D. Josephson. *Physics Letters*, 21:608, 1966.

[65] J. R. Beamish and N. Mulders. Quantum fluids and solids - 1989, 1989.

[66] P. A. Crowell, J. D. Reppy, S. Mukherjee, J. Ma, M. H. W. Chan, and D. W. Schaefer. *Phys. Rev. B*, 51:12721, 1995.

[67] J. D. Reppy. *Physica B*, 126:335, 1984.

[68] H. Cho and G. A. Williams. *Phys. Rev. Lett.*, 75:1562, 1995.

[69] T. C. Padmore. *Phys. Rev. Lett.*, 28:1512, 1972.

[70] F. D. M. Pobell, H. W. Chan, L. R. Corruccini, R. P. Henkel, S. W. Schwenterly, and J. D. Reppy. *Phys. Rev. Lett.*, 28:542, 1972.

[71] V. Kotsubo and G. A. Williams. *Phys. Rev. B*, 33:6106, 1986.

[72] V. A. Bogomolov. *Fluid Dynamics*, 12:863, 1978.

[73] Cat. A01124A0046. Robertshaw Tennessee, P.O. Box 400, 2318 Kingston Pike, Knoxville, TN 37901-0400, phone:(615)546-0550.

[74] E. D. Adams. *Rev. Sci. Instrum.*, 64:601, 1993.

[75] H. London. *Proc. R. Soc. A*, 171:484, 1939.

BIOGRAPHICAL SKETCH

Satoru Miyamoto was born on October 20, 1963, in Sapporo, Japan. In 1982, he entered Hokkaido University, where he received a bachelor's degree with a major in physics. He also received a Master of Science degree at the graduate school of Hokkaido University. Since September of 1988, he has been working toward the Doctor of Philosophy degree at University of Florida.

I certify that I have read this study and that in my opinion it conforms to acceptable standards of scholarly presentation and is fully adequate, in scope and quality, as a dissertation for the degree of Doctor of Philosophy.

Yasumasa Takano, Chairman
Professor of Physics

I certify that I have read this study and that in my opinion it conforms to acceptable standards of scholarly presentation and is fully adequate, in scope and quality, as a dissertation for the degree of Doctor of Philosophy.

Charles F. Hooper, Jr.
Professor of Physics

I certify that I have read this study and that in my opinion it conforms to acceptable standards of scholarly presentation and is fully adequate, in scope and quality, as a dissertation for the degree of Doctor of Philosophy.

Gary G. Ihas
Professor of Physics

I certify that I have read this study and that in my opinion it conforms to acceptable standards of scholarly presentation and is fully adequate, in scope and quality, as a dissertation for the degree of Doctor of Philosophy.

John M. Graybeal
Associate Professor of Physics

I certify that I have read this study and that in my opinion it conforms to acceptable standards of scholarly presentation and is fully adequate, in scope and quality, as a dissertation for the degree of Doctor of Philosophy.

M. Luis Muga
Professor of Chemistry

This dissertation was submitted to the Graduate Faculty of the Department of Physics in the College of Liberal Arts and Sciences and to the Graduate School and was accepted as partial fulfillment of the requirements for the degree of Doctor of Philosophy.

December 1995

Dean, Graduate School

LD
1780
1995
.M685

UNIVERSITY OF FLORIDA
3 1262 08556 9373